Study of Structural, Electrical, Optical, and Transport Properties of Ga-doped ZnO Thin Films Prepared by RF Magnetron Sputtering

Lukman Nulhakim

Supervisor: Prof. Hisao Makino

Submitted in partial fulfillment of the requirements for the degree of Doctor of Engineering in the Kochi University of Technology

Graduate School of Engineering
Kochi University of Technology, Japan
September 2016

Abstract

The structural, electrical, optical, and transport properties of Ga-doped ZnO (GZO) thin film prepared by radio frequency magnetron sputtering have been carefully investigated. In this study, there concerned two main topics on properties of polycrystalline GZO thin films, and obtained four significant results.

First main topic is concerning to electrical and optical properties of GZO thin films in relation with structure and defects.

Firstly, the effects of heated substrate on depositions of GZO films have been investigated. The polycrystalline GZO films deposited on glass substrates commonly show high *c*-axis preferred orientation when deposited at 200 °C, while they show poor *c*-axis orientation concomitant with lots of defects when deposited at room temperature (RT). Such the poor structural property and the defects seriously degrade performance of GZO films. So the high temperature deposition leads to improvement of structure, and annealing out of defects simultaneously. To understand effects of these two phenomena separately, we employed control of structure and post-deposition annealing. The structure of GZO film deposited at RT was controlled by inserting highly *c*-axis oriented self-buffer layer. It was revealed that the improvement of structure leads to reduction in contribution of grain boundary scattering to the Hall mobility. Whereas, the improvement of structure was not sufficiently effective to reduce the defects causing carrier concentration, low in-grain electron mobility, and low transmittance of GZO deposited at RT. Such the defects were able to be eliminated by the post-deposition annealing. Even though the in-grain mobility increase by annealing out of defects, the Hall mobility was strongly deteriorated by the grain boundary scattering caused by the poor structural properties.

Secondly, based on the preceding findings, the evolution of scattering mechanism and annealing out of defects were explored with varying substrate temperature (*Ts*) from RT to 200 °C. The defects probably caused by ion bombardment were gradually eliminated by increasing the *Ts*. The in-grain electron mobility which can be

evaluated by optical mobility, the carrier concentration, and the transparency which is decreased by absorption originating in defects, were gradually increased owing to the annealing out of defects. On the other hand, the contribution of the grain boundary scattering remained up to the *Ts* of 150 °C, and it abruptly vanished at 175 °C accompanied by the perfect *c*-axis orientation. From the characterization of structural properties, it was revealed that existence of oriented domains that has (10-11) plane parallel to the substrate was related to the scattering observed at the lower *Ts*.

Thirdly, the electrical properties of GZO thin films with film thickness of several tens nm were investigated from a viewpoint of crystallographic polarity. It was found that the electrical properties of GZO films deposited on Zn-polar ZnO were significantly improved compared to those deposited on O-polar ZnO. Using Zn-polar ZnO templates, a very low resistivity of 2.62×10^{-4} Ω cm was achieved for 30 nm-thick GZO films on a glass substrate. It was proposed that polarity inversion plays an important role in determining the electrical properties of extremely thin GZO films.

Second main topic is application of GZO films for hydrogen gas sensors. In this study, we focus on the effects of structural properties on gas sensitivity. One of important parameter as sensing materials is film thickness. However, the grain size and *c*-axis orientation both changed depending on the films thickness. Accordingly, it was difficult to interpret dominant factor to determine gas sensitivity. To clarify this issue, highly *c*-axis oriented ZnO templates were used to control the structural properties. The grain size of GZO films on ZnO template increased with increasing the thickness of template, while the *c*-axis orientation was kept as comparable. It was found that the hydrogen gas sensitivity increased with increasing tilting of *c*-axis. It was therefore proposed that *c*-axis orientation plays an important role to determine the hydrogen gas sensitivity of polycrystalline GZO thin films.

Contents

1. Introduction

1.1 Background

ZnO has a wurtzite structure that naturally performs as an n-type semiconductor. Over the last few decades, there has been growing interests of ZnO as material for a wide variety of device applications. For practical applications, doping to semiconductor is fundamentally necessary in order to control their properties depending on purposes. There are several candidates of n-type dopant for ZnO, e.g., group III elements (B, Al, Ga and In), group IIIB of rare earth metals (Sc and Y), group IV elements (Si, Ge, and Sn), and group VII elements (F and Cl) [1]. The report on doping of ZnO thin films can be seen on several topics, group IV impurity-doped ZnO [2], and Ti-doped ZnO [3] for transparent conductive films, Cu-doped [4], Eu-doped [5], and Er-doped ZnO [6, 7] for nonlinear optics or fluorescent thin films, and so on.

In the optoelectronic applications such as thin-film photovoltaics [8], flat panel displays [9], and light-emitting diodes [10], considerable recent attention has been paid to transparent conductive oxides (TCOs) for use as transparent electrodes. The development of TCO materials has already started in about 1950s based on material of CdO and Sn-doped In_2O_3 (ITO) [11, 12]. Nowadays, the most widely used TCO is ITO, however, some alternatives to ITO have been desired in the last decade because of scarcity of In and also toxicity issues with its processing [13, 14]. ZnO-based TCOs like as Al-doped ZnO (AZO) and Ga-doped ZnO (GZO) have been studied for long time as materials for transparent electrodes as well [13, 14]. In the last few years, GZO and AZO films have widely been proposed as an alternative to ITO due to their similar low resistivity (~1–3 $\times$ 10^{-4} Ω.cm), their large optical band gap (higher than 3.4 eV for GZO and ~3.7 eV for ITO), and the advantages of higher transmittance of GZO in the visible wavelength range compared with ITO [15-17]. Recently, current research on the heavily doped ZnO is more focus on transport properties.

On the other hand, considerable attention has been paid to hydrogen as a one of promising clean energy resources in the world [18]. There are a lot of advantages of hydrogen in wide area, i.e., hydrogen for fuels, automobile, fuel cells, chemical material industry, and so on [19, 20]. On the concentration of higher than 4% in air, the hydrogen gas was flammable and explosive [20]. Since hydrogen gas has specific properties such as odorless, tasteless, colorless, and undetectable by human senses, it is very important to fabricate sensitive and reliable sensing devices to detect hydrogen. For this purpose, there has been growing interest again on gas sensors based on metal oxide semiconductors, e.g., SnO_2, In_2O_3, and ZnO.

1.2 Motivation and strategy

The heavily doped ZnO films can be prepared by several deposition methods, such as magnetron sputtering (MSP), pulsed laser deposition (PLD), evaporation, metal organic chemical vapor deposition (MOCVD), ion plating (IP), vacuum arc plasma evaporation (VAPE), spray pyrolysis, and electrochemical deposition [1, 21]. The MSP is one of the most effective methods for film deposition due to its low-temperature deposition, easy scalability to large-area deposition, homogenous and fairly dense of films and also relatively simple control over the film thickness [22, 23].

In the MSP deposition of ZnO-based TCOs, defects caused by ion bombardment during deposition is one of crucial issue. Bikowski et al. [24] demonstrated that the electrical properties of AZO films are strongly affected by negative oxygen ion bombardment during deposition. The electrical resistivity improves by increasing the substrate temperature *Ts*, and the improvement has been explained by annealing out of the defects by increasing *Ts* [24]. On the other hand, it was also reported that the structural properties of ZnO thin films like as grain size and c-axis preferred orientation can be improved by increasing *Ts* [25]. Concerning transport properties, the influences of intrinsic defects on transport [26, 27], scattering mechanisms limiting the carrier mobility [28, 29], and the relationship between microstructural

properties and transport [30-32] have been reported for ZnO-based TCOs. The influence of grain boundaries on the carrier transport also has been discussed [30-35]. It was reported that the contribution of grain boundary scattering strongly depended on the structural properties [36].

As mentioned above, the point defects decrease with increasing *Ts*, while the structural properties improve with increasing *Ts* as well. Both the defects and structure will affect electrical properties of heavily doped ZnO thin films. Then, questions arise: what is the main factor limiting electrical properties of heavily doped ZnO thin films deposited by the MSP at low temperature: how each of defects and structural properties influence the electrical properties.

Next issue is the electrical properties of thinner films below 100 nm on highly doped ZnO. It has been recognized the electrical properties of heavily doped ZnO shows strong thickness dependence especially thickness below 100 nm [Ref. 37, 38, 39, and 40]. Yamada et al. [37] discussed electrical properties in relationship with the *c*-axis orientation and grain size. Look et al. [38, 39] suggested that electrical properties influenced by a poor interface layer due to high density defects at the interface of substrates. Bikowski et al. [41] reported the inhomogeneous distribution of Al dopants for very thin films. Considerable attentions have been paid for the issue, however, causes of the high resistivity of very thin films are still under discussion.

From a viewpoint of application of the heavily doped ZnO, it has been considered to be one of promising candidates as sensing materials for hydrogen gas sensors [18]. The sensing mechanism is based on change of electrical properties caused by surface reactions with hydrogen [20]. Since the electrical properties strongly depends on structural properties of thin films in doped ZnO as discussed above, the sensing properties might be also influenced. Effects of grain size has been studied for several metal oxides semiconductors including ZnO [42, 43, 44, 45], however, there is no report on effects of *c*-axis orientation on gas sensing properties.

Based on the above mentioned present status about heavily doped ZnO thin films, this thesis aimed to clarify the following issues on heavily Ga-doped ZnO thin films deposited by Radio Frequency (RF) magnetron sputtering.

1. This study aimed to clarify the effects of the *Ts* on the properties of GZO films deposited by RF magnetron sputtering in terms of the microstructural properties and annealing out of the point defects. The discussion will especially focus on the scattering mechanisms of charge carriers.
2. This study also aimed to clarify cause of strong thickness dependence of electrical properties of GZO films deposited by RF magnetron sputtering with thickness below 100 nm. The discussion will focus on the influence of crystallographic polarity.
3. As a one of application of GZO films deposited by RF magnetron sputtering, the study aimed to clarify the effects of structural properties (grain size and *c*-axis orientation) on hydrogen gas sensing.

In order to achieve these objectives, a template or a buffer layer on substrate is cleverly utilized to control microstructural properties of GZO thin films. In addition, comparison between the Hall mobility and optical mobility is employed to explore carrier scattering mechanism governing the electrical properties of GZO thin films.

1.3 Scope of the thesis

The thesis describes the study of structural, electrical, optical, and transport properties of Ga-doped ZnO thin films prepared by RF magnetron sputtering. This thesis consists of eight chapters.

First chapter is “Introduction”. In this chapter, purpose of the study covering all topics in this study, and outline of this thesis are summarized.

Second chapter is “Fundamentals”. In this chapter, general properties of zinc oxide (ZnO) like as crystal structure, crystallographic polarity, and defects, are briefly

introduced. In addition, scattering mechanism of charge carriers, principles of magnetron sputtering, and gas sensors based on metal oxide semiconductors are briefly introduced.

Third chapter is “Research Methodology”. In this chapter, methodology of thin film deposition, characterization techniques employed in this dissertation, and analytical evaluations are described.

Next four chapters are main part of this thesis consists of four topics published (or to be published) in refereed journals. Each chapter consists of introduction, experimental method in details, results and discussion, conclusion, and references.

Fourth chapter is focus on the influence of microstructure and point defects on electrical and optical properties of GZO films deposited at room temperature on glass substrates. The influences are separately discussed by combining microstructural control and post deposition annealing.

Fifth chapter investigated the effects of substrate temperature on properties of GZO films in terms of microstructure annealing out of defects and improvement of c-axis orientation. The discussion is focus on the change of scattering mechanism.

Sixth chapter is focus on the properties of thinner GZO films. The influence of polarity inversion has been discussed and clarified.

Seventh chapter is focus on the hydrogen gas sensor based on GZO thin films. The GZO as a material class of TCOs reveals not only applicable for optoelectronic applications but also for gas sensing applications.

The last chapter of this thesis is “Concluding Remarks”. This chapter concludes findings and achievement thorough this study and some concluding remarks are given.

1.4 References

[1] H. Morkoc and U. Ozgur, Zinc Oxide: Fundamentals, Materials and Device Technology, WILEY-VCH Verlag GmbH & Co. KGaA, Winheim, p. 246, (2009).

[2] H. Sato, T. Minami, S. Takata, J. Vac. Sci. Tech. A 11, 2975 (1993).

[3] H. P. Chang, F. H. Wang, J. C. Chao, C. C. Huang, H. W. Liu, Curr. Appl. Phys.11, S185 (2011).

[4] L. Ma, S. Ma, H. Chen, X. Ai, X. Huang, Appl. Surf. Sci. 257 10036 (2011).

[5] A. M. Ahmed, P. Szymanski, M. A. El-Sayed, Y. Badr, L. M. El-Nadia, Appl. Surf. Sci. 359 356 (2015).

[6] T. M. Williams, D. Hunter, A. K. Pradhan and I. V. Kityk, Appl. Phys. Lett. 89, 043116 (2006).

[7] P. T. Neuvonen, K. Sigvardt, A. R. Johannsen, J. Chevallier, B. Julsgaard, S. K. Ram, and A. N. Larsen, Appl. Phys. Lett. 104, 102106 (2014).

[8] T. Minami, T. Miyata, and J. Nomoto, IOP Conf. Ser.: Mater. Sci. Eng. 34, 012001 (2012).

[9] N. Yamamoto, H. Makino, S. Osone, A. Ujihara, T. Ito, H. Hokari, T. Maruyama, and T. Yamamoto, Thin Solid Films 520, 4131-4138 (2012).

[10] J-K Sheu, Y.S. Lu, M-L. Lee, W.C. Lai, C.H. Kuo, and C-J.Tun, Appl. Phys. Lett. 90, 263511 (2007).

[11] G. Helwig, Phys. 132, 621 (1952)

[12] Rupprecht, Phys. 139, 504 (1954)

[13] T. Minami, Thin Solid Films 516, 1314-1321 (2008).

[14] T. Yamamoto, T. Yamada, A. Miyake, H. Makino, and N. Yamamoto, J. Soc. Inf. Disp. 16, 713-719 (2008).

[15] T. Minami, Semicond. Sci. Technol. 20, S35 (2005).

[16] T. Yamada, H. Makino, N. Yamamoto, and T. Yamamoto, J. Appl. Phys. 107, 123534 (2010).

[17] T. Yamamoto, T. Yamada, A. Miyake, H. Makino, N. Yamamoto, J. Soc. Inf. Disp. 16, 713 (2008).

[18] D. C. Look, J. Electron. Mater. 35, 1299 (2006).

[19] M. Fleischer and H. Meixner, J. Vac. Sci. Technol. A 17, 1866 (1999).

[20] A. Rothschild and Y. Komem, J. Appl. Phys. 95, 6374 (2004).

[21] K. Elmer, A. Klein, B. Rech, Transparent conductive zinc oxide, basics and applications in thin film solar cells, Springer, Verlag Berlin Heidelberg, 2008.

[22] T. Minami, H. Sato, H. Nanto, and S. Takata, Jpn. J. Appl. Phys. 24 Part 2, L781 (1985).

[23] C. Agashe, O. Kluth, J. Hüpkes, U. Zastrow, B. Rech, and M. Wuttig, J. Appl. Phys. 95, 1911 (2004).

[24] A. Bikowski, T. Welzel, and K. Ellmer, Appl. Phys. Lett. 102, 242106 (2013).

[25] C. C. Singh, T.A. Patel, and E. Panda, J. Appl. Phys. 117, 245312 (2015).

[26] D. O. Demchenko, B. Earles, H. Y. Liu, V. Avrutin, N. Izyumskaya, U. Ozgur, and H. Morkoc, Phys. Rev. B 84, 075201 (2011).

[27] D. C. Look, K. D. Leedy, L. Vines, B. G. Svensson, A. Zubiaga, F. Tuomisto, D. R. Doutt, and L. J. Brillson, Phys. Rev. B 84, 115202 (2011).

[28] K. Ellmer and R. Mientus, Thin Solid Films 516, 4620-4627 (2008).

[29] T. Terasako, H. Song, H. Makino, S. Shirakata, and T. Yamamoto, Thin Solid Films 528, 19-25 (2013).

[30] T. Yamada, H. Makino, N. Yamamoto, and T. Yamamoto, J. Appl. Phys. 107, 123534 (2010).

[31] H. Y. Liu, V. Avrutin, N. Izyumskaya, U. Ozgur, A. B. Yankovich, A. V. Kvit, P.M. Voyles, and H. Morkoc, J. Appl. Phys. 111, 103713 (2012).

[32] S. Y. Lee, W. Lee, C. Nahm, J. Kim, S. Byun, T. Hwang, B. K. Lee, Y. I. Jang, S. Lee, H. M. Lee, and B. Park, Curr. Appl. Phys. 13, 775-778 (2013).

[33] H. Makino, N. Yamamoto, A. Miyake, T. Yamada, Y. Hirashima, H. Iwaoka, T. Itoh, H. Hokari, H. Aoki, and T. Yamamoto, Thin Solid Films 518, 1386-1389 (2009).

[34] H. Makino, H. Song, and T. Yamamoto, Thin Solid Films 559, 78-82 (2014).

[35] D. C. Look, K. D. Leedy, D. B. Thomson, and B. Wang, J. Appl. Phys. 115, 012002 (2014).

[36] L. Nulhakim and H. Makino, Thin Solid Films 615, 158-164 (2016).

[37] T. Yamada, A. Miyake, S. Kishimoto, H. Makino, N. Yamamoto, and T. Yamamoto, Appl. Phys. Lett. 91, 051915 (2007).

[38] D. C. Look, K. D. Leedy, A. Kiefer, B. Claflin, N. Itagaki, K. Matsushima, and I. Surhariadi, Opt. Eng. 52, 033801 (2013).

[39] D. C. Look, B. Claflin, A. Kiefer, and K. D. Leedy, Opt. Eng. 53, 087108 (2014).

[40] N. Itagaki, K. Kuwahara, K. Nakahara, D. Yamashita, G. Uchida, K. Koga, and M. Shiratani, Appl. Phys. Express 4, 011101 (2011).

[41] A. Bikowski, M. Rengachari, M. Nie, N. Wanderka, P. Stender, G. Schmitz, and K. Ellmer, APL Mater. 3, 060701 (2015).

[42] N. H. Al-Hardan, M. J. Abdullah, A. A. Aziz, Int. J. Hydrogen Energy 35, 4428 (2010).

[43] A. A. Haidry, J. Puskelova, T. Plecenik, P. Durina, J. Gregus, M. Truchly, T. Roch, M. Zahoran, M. Vargova, P. Kus, A. Plecenik, and G. Plesch, Appl. Surf. Sci. 259, 270 (2012).

[44] G. Korotcenkov, I. Boris, V. Brinzari, S. H. Han, B. K. Cho, Y. N. Lychkovsky, Ceram. Int. 41, 7478 (2015).

[45] N. Al-Hardan, M. J. Abdullah, A. A. Aziz, H. Ahmad, Appl. Surf. Sci. 256, 3468 (2010).

2. Fundamentals

2.1 Zinc Oxide as a semiconductor

In the last decades, there has been a growing interest in ZnO and related materials. ZnO is one of promising materials for several semiconductor device applications. ZnO have direct band gap of about 3.4 eV at room temperature with large exciton binding energy of about 60 meV [1]. Such the large binding energy has been considered to be suitable for optical device applications. ZnO material also reveals large piezoelectric constants [2] that will suitable for sensors and actuators applications based on mechanical properties. In addition, ZnO has been considered as sensing materials in gas sensors. The surface of ZnO are very reactive to gases such as oxygen and hydrogen. In this section, fundamental properties of ZnO as a semiconductor are out looked.

2.1.1 Crystal Structure

The crystal structure of ZnO is hexagonal wurtzite that occur naturally as the rare mineral zincite [3]. The phase of wurtzite structure under ambient condition is thermodynamically stable [4]. ZnO also have another structure such as rock salt that showed metastable cubic phase [5, 6]. The ZnO large bulk single crystals naturally almost always available as *n*-type [2]. The structure of wurtzite ZnO can be seen in the Fig. 2.1 (a). The Fig. 2.1 (b), (c), and (d) show the different orientations of a crystal with hexagonal structure.

The crystal structure measured by using X-ray diffraction showed the hexagonal unit cell. The *c*-axis and *a*-axis lattice parameters are 0.52066 nm and 0.325 nm, respectively [5, 7]. In general, the lattice parameter of a semiconductor can be affected by several factors, i.e., 1) deformation potential of a conduction band minimum that occupied by free electron concentration, 2) the substituted matrix ions that related to the concentration of foreign atoms and defects, and 3) by their difference of ionic radii, external strains, and also temperature [4]. The deviation such

as the increasing of lattice parameter could be influenced by lattice stability, ionicity, point defects (e.g., oxygen vacancies, zinc antisites), and extended defects (e.g., threading dislocations) [4].

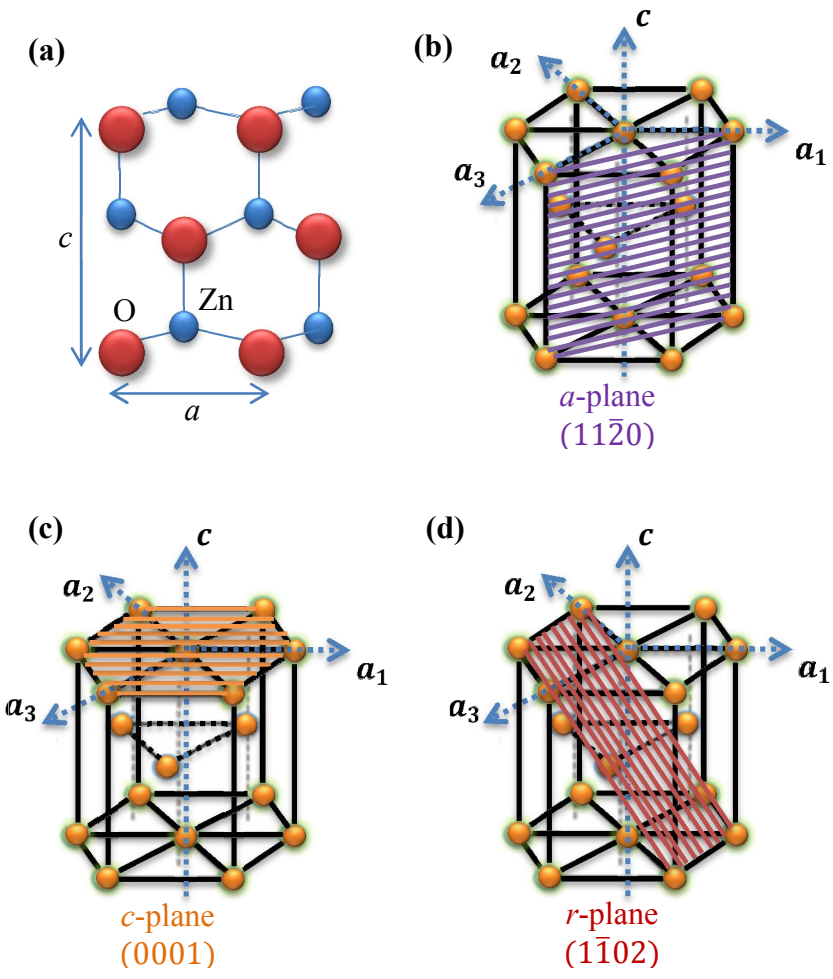

Fig. 2.1 The wurtzite structure with *a* and *c* lattice constants (a) and the schematic drawing of a hexagonal single crystal with different crystallographic planes: *a*-plane (b), *c*-plane (c) and *r*-plane (d), respectively. [Images referred to Ref. 2, 4, 8, 9, with modification].

In the practical studies, the *a* and *c*-axis lattice parameters and volume of unit cell of ZnO can be estimated by XRD measurements. The value of inter-planar spacing (*d*)

that showed perpendicular distance between adjacent planes in the set of *hkl* for the hexagonal structure can be calculated by the following equation [10],

$$\frac{1}{d^2} = \frac{4}{3}\left(\frac{h^2 + hk + k^2}{a^2}\right) + \frac{l^2}{c^2}$$

where *h, k*, and *l* related to the miller indices of the plane. By using the value of *a* and *c* lattice constants, the volume of unit cells (*V*) is given by,

$$V = \left(\sqrt{3}\, a^2 c\right)/2 = 0.866 a^2 c$$

The miller indices using four-digit system, i.e., *hk-il*, where *h+k =-i* are shown in Fig. 2.1. It should be noted that the *hkl* in three-digit system of miller indices is corresponding to *hk-il* in the four-digit system. The *c*-axis direction is referred to as [0001] and the hexagonal (0001) plane means that the lattice plane is perpendicular to the *c*-axis [9].

2.1.2 Polarity of ZnO

Since ZnO materials have conspicuous bond, this material shows polar character in *c*-axis direction that so-called crystal axis polarity [9]. On wurtzite ZnO, the opposite polarity for *c*-cut ZnO crystals, i.e., Zn-terminated (0001) face on one side and the O-terminated $(000\bar{1})$ face on the other side represent a sequence of positively charged Zn^{2+} and negatively charged O^{2-} ions in planes perpendicular to the *c*-axis. The different polarity of Zn-face and O-face causes the differences of etching behavior, doping characteristics, formation of defects and growth properties [4, 9]. The polarity that is caused by spontaneous polarization of ZnO has been expected to be responsible for anisotropic electronic structure, mechanical properties, and chemical properties [4, 11]. Fig. 2.2 shows the ZnO crystallizes into the wurtzite structure along the *c*-axis that consists of alternating planes of Zn and O atoms [12, 13].

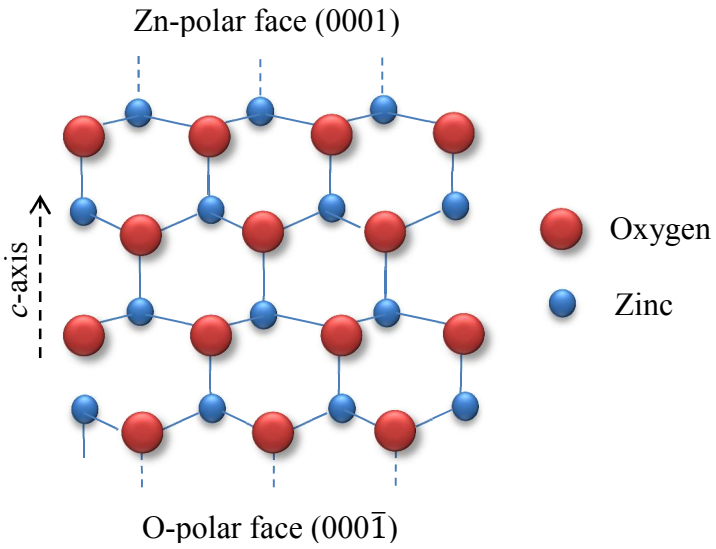

Fig. 2.2 The ZnO crystallizes into the wurtzite structure along the *c*-axis that consists of alternating planes of Zn and O atoms.

2.1.3 Defects in ZnO

While ZnO has many advantages for applications in the optoelectronic and sensor devices, control of doping and defects, which are very important factors for device applications, is still remaining as critical issue. On ZnO, the electrical and optical properties can be controlled by impurities and defects. The impurities can be as donor type impurities such as Ga, Al, In, H and can be as acceptor type impurities such as P, As, and N [14]. The performances and properties of ZnO and doped ZnO are strongly affected by native point defects. The native point defects are also classified into donor type defects such as zinc interstitial (Zn_i) and oxygen vacancies (V_O) and acceptor type defects such as zinc vacancies (V_{Zn}) and oxygen interstitial (O_i).

The Zn_i is stated to be a shallow donor [15], but it is highly mobile [16] and not stable at room temperature [17]. So the Zn_i has been considered to be annealed out at a temperature of 170 K [18]. On the other hand, the V_O is a deep donor that cannot be considered as source of residual carriers in n-type ZnO. The deep donor

characteristics of V_O has been confirmed by first-principles calculations [19]. Even though the V_O act as deep donor, the formation energy of V_O is lower [20] compared to the Zn_i acting as shallow donor in ZnO [21]. For the acceptor type of defects, the V_{Zn} is considered to be the most important deep level acceptors [20] with the lowest formation energy compared to all other point defects in *n*-type ZnO. Whereas, the O_i has higher formation energy in ZnO [16].

In addition to the native point defects like as V_O and Zn_i, impurities also play important role [18]. The diffusion of hydrogen might be occurred on the ZnO crystal instead of point defect and other impurities. The report suggests that H is always a donor in ZnO and it was easily ionized when they have low formation energy [14]. Based on the theoretical work, H has been considered to be a shallow donor in the *n*-type ZnO [22]. Based on the first-principle calculations, an O substitutional site can be occupied by H, and the H act as a shallow donor [23]. Furthermore, native defects interacting with dopants of group III elements and H might affect the electrical properties of ZnO. Look *et al* suggested that native defect complexes with donor elements can appear and contribute to conductance of *n*-type ZnO [24]. It was pointed out that control of native point defects is possible by incorporation of impurities during growth or annealing process [16]. In the practical studies, the native point defects in ZnO may be possibly observed by spectroscopic experimental techniques like as photoluminescence, however, the role of native point defects are still not so clearly understood at the present.

2.2 Charge Carrier Scattering Mechanism

In a semiconductor, the scattering plays an important role to determine carrier transport properties. Accordingly, it is important to understand scattering mechanism governing the carrier mobility. Generally, the charge carrier was considered to be scattered by two aspects: one is stationary defects e.g., impurities and dislocations and another is dynamic defects e.g., electrons, holes and lattice phonons [4].

The electrical resistivity of an *n*-type semiconductor can be calculated in a part of the electrical mobility and carrier concentration as:

$$\rho = \frac{1}{qn\mu}$$

where n is carrier concentration, μ is electron mobility and q is the electron charge. The electron mobility can be expressed in a part of the conductive effective mass m_c* and the relaxation time τ by:

$$\mu_n = \frac{q\langle\tau\rangle}{m_c^*}$$

where $\langle\tau\rangle$ is the average relaxation time [25]. Generally, based on the Matthiesen's rule, the overall of mobility can be expressed as the following formulation:

$$\frac{1}{\mu} = \sum_{i=1}^{n} \frac{1}{\mu_i}$$

where μ_i is the mobility due to the i_{th} scattering mechanism.

When the impurity or dopant content increase, the mobility will be limited by the ionized impurity scattering as the carrier concentration increase. It was reported for polycrystalline ZnO films that the main contribution is grain boundary scattering when the value of carrier concentration $N \leq 10^{19}$ cm^{-3}, while the dominant scattering mechanism is ionized impurity scattering when $N \geq 10^{19}$ cm^{-3} [26]. Furthermore, Look *et al* [27] suggested that scattering at boundaries (surfaces and interfaces) must be considered in thin films, and that phonon scattering should be included especially at high temperatures. Then, the total mobility of thin films, $\mu_{tot,}$ can be expressed using these major scattering mechanisms as:

$$\frac{1}{\mu_{tot}} = \frac{1}{\mu_{ii}} + \frac{1}{\mu_{phonon}} + \frac{1}{\mu_{boundary}}$$

where μ_{ii} is the ionized impurity scattering (scattering by impurities and point defects depending on donor (N_D) and acceptor (N_A) concentrations), μ_{phonon} is the phonon scattering, and $\mu_{coundary}$ is the scattering at boundaries (surface, interface between film and substrate, and also grain boundaries). Each of the major scattering mechanisms that generally governs the electron transport in doped n-type ZnO thin films is explained in the following sections.

2.2.1 Polar optical phonons (POP) scattering

The POP scattering is stirred by the interaction between the charge movements over the lattice with an electric field induced by electric polarization that concomitant with lattice vibration due to the nature of partially ionic bonding in a polar semiconductor [4, 26, 28]. In a polar material, POP scattering plays an important role at temperature near or above room temperature [29]. The effect of this scattering is much robust than other scattering mechanisms. The temperature dependence of mobility is limited by POP scattering. The relationship of them can be expressed as below [30]:

$$\mu_{pop}\left[\frac{cm^2}{V.s}\right] = 0.199x\sqrt{\frac{T}{300}}x\left(\frac{e}{e^*}\right)^2 x\left(\frac{m_0}{m^*}\right)\sqrt{\frac{m_0}{m^*}}x(10^{22}M[g])$$
$$x(10^{23}Va[cm^3])x(10^{-13}\omega[s^{-1}])$$
$$x\left(e^{\frac{h\omega}{kB\,T}}-1\right)x\;G\;\left(\frac{h\omega}{kB\,T}\right)$$

where e^* is the effective charge, M is the reduced mass, V_a is the volume of the unit cell, and m^* is the effective mass of electron and kB is the Boltzmant constant. The POP scattering is very essential since Fermi level situation is more deeply in the conduction band. The details of POP scattering can be found in Ref. 29.

2.2.2 Ionized impurity scattering

The deflection of free carriers by the long-range coulomb potentials of the charge centers that triggered by intentionally doped impurities or unintentionally formed defects lead to crucial contribution of the ionized impurity scattering. This scattering act as a local perturbation of the band edge that can affect the motion of electrons [4]. The ionized impurity scattering is very important in doped materials, particularly for heavily doped semiconductors like as TCOs. The long range electrostatic fields which related to defects and dopants like vacancies and interstitials are indication of this scattering [26]. Look *et al* reported that dominant scattering mechanism at room temperature was not phonons but charge of donors and acceptors which act as scattering centers in the whole temperature range in the case of highly Ga-doped ZnO. Since carrier concentration *n* does not depend on temperature, the ionized impurity scattering can be conveyed from the degenerate form of the Brooks-Herring formula [29, 31]:

$$\mu_{max} = \frac{24\pi^3\varepsilon_0^2h^3}{Z^2e^3m^{*2}} \frac{1}{ln[1+y(n)]-\frac{\dot{y(n)}}{1+y(n)}}$$

where *e* and ε_0 are the elementary charge and dielectric constant, respectively, which correspond to the ionization of Z,

with $y(n) = \frac{3^{1/3}4\pi^{8/3}\varepsilon_0h^2n^{1/3}}{e^2m^*}$ where m^* is an effective mass.

2.2.3 Grain boundary scattering

Generally, in polycrystalline thin films, carriers can be scattered due to the discontinuity at grain boundaries [26]. When the grain size is comparable with mean free path of the charge carriers, the grain boundary scattering intensely affect the mobility of TCOs. The grain boundary scattering can be specified by prevailing defects resulting in chemical bonds at grain boundaries. The equation below

represents the carrier mobility due to the grain boundary scattering in degenerate semiconductors that was established originally by Seto [32], and was also mentioned by Terasako *et al* [33] for heavily Ga-doped ZnO thin films as below:

$$\mu_{gb} = \frac{eL}{\sqrt{2\pi m^* k_B T}} exp\left(\frac{-V_B}{k_B T}\right)$$

where m^* is the effective mass which depends on n, L is the grain size, V_B is the potential barrier height between grain boundaries, and k_B is the Boltzmann constant.

2.3 Magnetron Sputtering

The deposition methods of thin film can be classified to Physical Vapor Deposition (PVD) and Chemical Vapor Deposition (CVD) process. The process of PVD is broadly divided into thermal process and plasma process. The plasma processes including magnetron sputtering, ion plating and plasma CVD are utilizing active ions appearing in the plasma for depositions. On the other hand, the vacuum evaporation and molecular beam epitaxy are operated based on thermal process [34]. The magnetron sputtering that classified into PVD process is one of the most widely used deposition methods to fabricate ZnO thin films. The advantages of magnetron sputtering compared to other methods are its low cost, simplicity of the deposition process, and possibility to deposit film at low substrate temperature with fairly high film quality and uniformity. In the sputtering deposition, particles sputtered out from target materials are condensing onto a substrate in a high vacuum environment [35].

The principle of magnetron sputtering is transfer of thermal energy assisted by a magnetic field. Generally, there are three types of magnetron sputtering, i.e., DC magnetron sputtering, RF magnetron sputtering, and reactive magnetron sputtering. In the sputtering deposition of oxide films, either metallic or ceramic materials can be used as target materials. At the present, the selection of ceramic target showed more benefit due to more simple control of gas atmosphere such as combination between

Ar and oxygen during the sputtering process. When using metallic target, it is necessary to control gases precisely in order to control not only sputtering activity but also metal to oxygen ratio that will be correlated to their stoichiometry and process stability during deposition.

In the magnetron sputtering method, the Ar gas was introduced to create ion plasma that can accelerate the collision ions and atoms from target onto substrate. In order to normalize the sputtering yield rate from the ZnO target, the RF power was adjusted and applied to the plasma [4]. On the experiments, usually the target is pre-sputtered for 5 to 15 minutes prior to the practical deposition in order to remove any contamination on the surface of target, to stabilize the system, and to reach the optimum conditions. A Turbo Molecular Pump (TMP) is used to evacuate the chamber reach to the high vacuum level in the order from 10^{-4} to 10^{-6} Pa that was enough to prevent and to reduce the contaminations. In order to maintain deposition conditions, a load-lock or transfer chamber, which allows us to transfer substrates without opening a main deposition chamber, would be desired connecting to the main chamber in magnetron sputtering systems.

The materials usually used as targets for deposition of oxide films are oxides type. The substrate is usually located on the top (or bottom) of main chamber together with heating system as an anode part, while the oxide target is engaged on the bottom (or top) together with magnet and cooling system that act as a cathode part. The ambient gas, i.e., Ar gas is filled in between these two electrodes in the sputtering chamber during deposition. When the power is applied, this Ar gas will be ionized. The formation of plasma or glow discharge will occur due to the ionization of Ar gas. The magnetic field leads to effective interactions between electrons and Ar ions that responsible to the plasma occurrence. The high energy gas ions will exist due to the effects of coulomb attraction from cathode target initiation. Then, the ejection of atoms from the surface of target will be active due to the bombardment of gas [35].

The process and principle of magnetron sputtering can be illustrated in Fig. 2.3. Generally, when the target material is bombarded by energetic ion (Ar), the target atom will be ejected into the space due to the vigorous collision of the energetic ions. Then, the ejected atoms will be move out in some distance until reach to the substrate and start to condense into a film. When the coalescence of atoms on the substrate continuously active, the atom will start bind to each other at the molecular levels that will form a strongly bound of atomic layer. The layers of atom will depend on the sputtering time or deposition rate that will lead to the precise layer of thin films structures on such thin films deposition [35, 36, 37, 38].

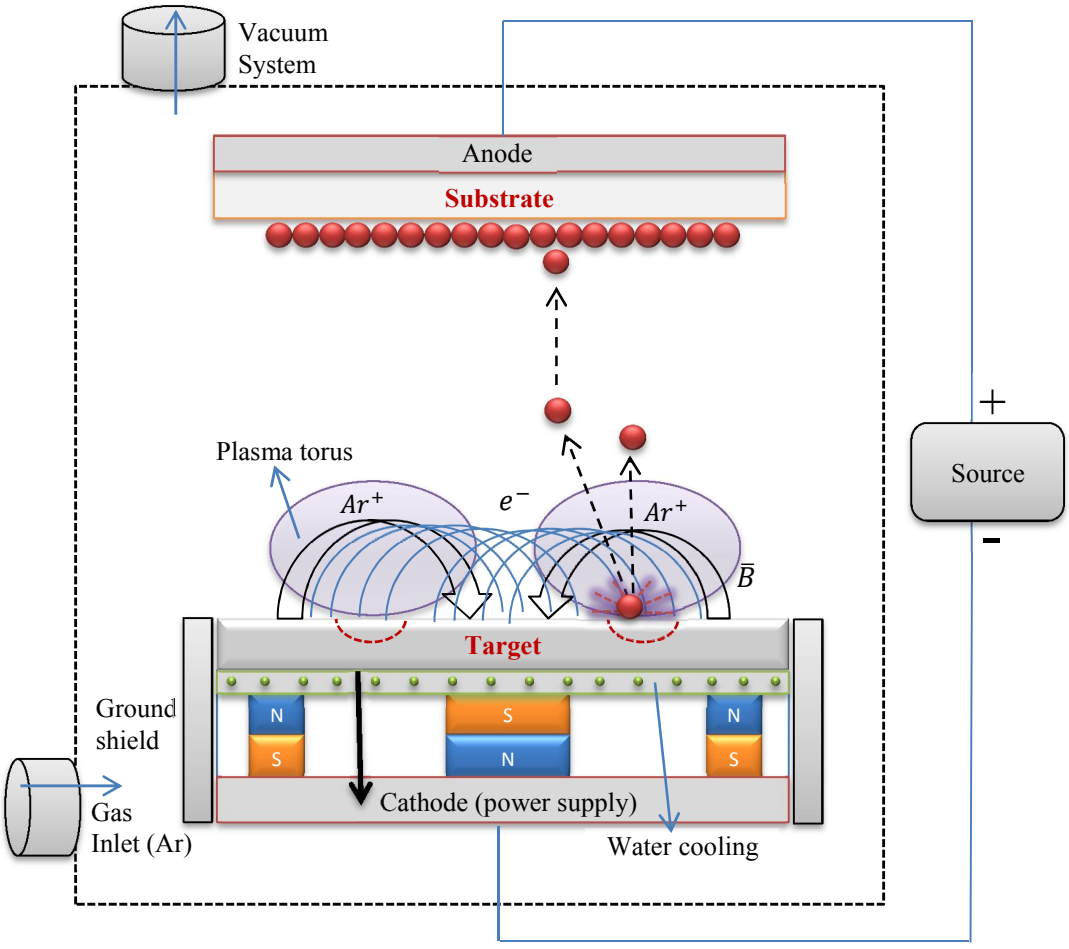

Fig. 2.3 Schematic view of thin films deposition using magnetron sputtering system [35, 36, 37, 38].

2.4 Gas sensors based on metal oxides semiconductor

The surface conductivity or resistance of metal oxides could be intensely influenced by the environment gas atmosphere such as hydrogen and oxygen. The Fermi level can be affected by the adsorption of such gases onto the surface [9]. Based on this indication, the metal oxides are potential candidate as sensing materials for gas sensor application. Lots of studies on the application of metal oxide for gas sensors are reported in Ref. 39-51. Several kinds of metal oxides have been tested for detecting combustible, reducing or oxidizing gases, e.g., In_2O_3, TiO_2, WO_3, Ga_2O_3, SnO_2, MgO, Al_2O_3 and ZnO [39, 52]. A sensor element normally provides part of sensitive layer over the substrate with electrodes and heater. The electrodes are used for measurement of the electrical characteristics of the sensitive layer [44]. Commonly, the resistance or current is monitored as a function of target gas concentration or operating temperature.

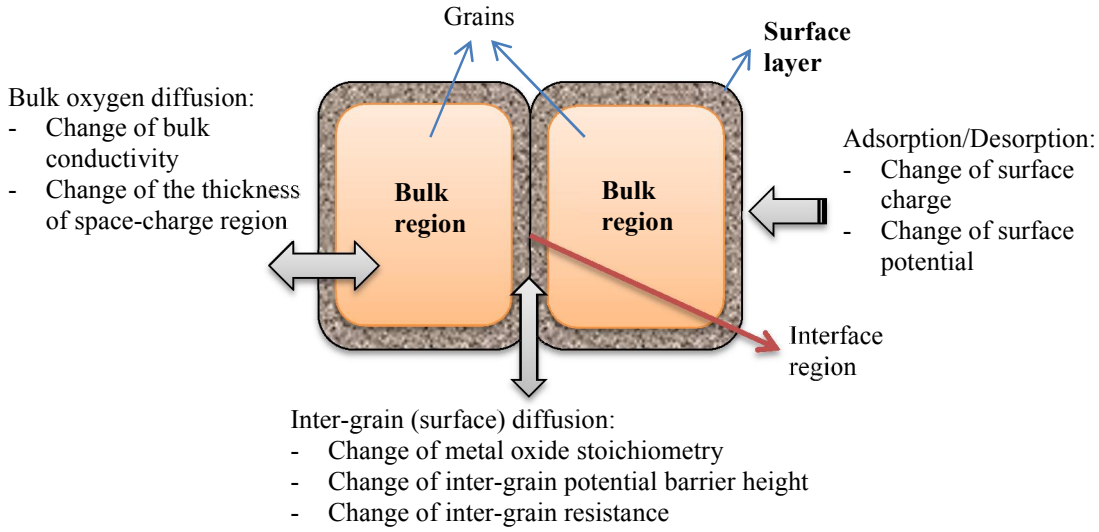

Fig. 2.4 The illustration diagram of process taking during gas detection and their influences especially for polycrystalline metal oxides properties [Adapted from Ref. 40, with modification].

On the metal oxides, the gas response would be affected by surface reactions process, i.e., adsorption-desorption, reduction, re-oxidation, chemical reactions, electron

exchange (between adsorbed species and surface or bulk), and diffusion process, e.g., inter-grain oxygen diffusion, bulk oxygen diffusion, surface diffusion of adsorbed species and gas diffusion within the bulk [39]. The phenomena related to the gas sensing are summarized in Fig. 2.4.

In order to examine the sensor characteristic or properties, usually metal oxide semiconductor materials in form of thin or thick films are exposed to the gas atmosphere. Gas sensor response or sensitivity can be determined by measuring the change of its electrical conductivity or resistance upon exposure to target gases with reference to the baseline in air atmosphere as illustrated in Fig. 2.5.

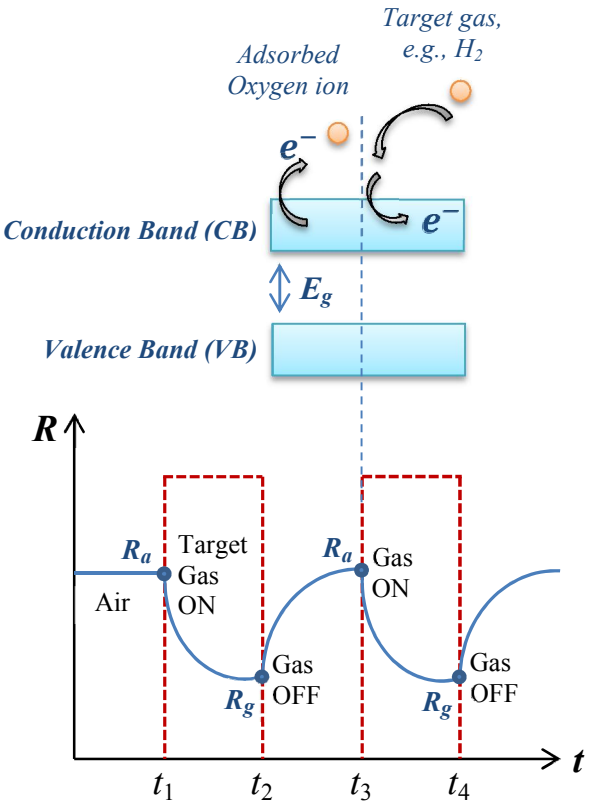

Fig. 2.5 Characteristic of dynamic sensor response as a function of time *t* which determined by the change of electrical resistance when the sensor sample expose to air and target gas.

Basically, the surface reaction phenomena play the most important role in the gas sensing mechanism. Interaction of gases with metal oxides semiconductor surfaces will follow such reaction type, e.g., adsorption-desorption, reduction/oxidation, ion exchange, and surface state [53]. The influence of gas reaction on sheet carrier concentration, N_s, can be explained by the interaction between oxygen and surface of sample at specific operating temperature. For instance, the interaction with atmospheric oxygen at temperature between 100 °C and 500 °C leads to its ionosorption in molecular (O_2^-) and atomic (O^-, O_2^-) [44, 54]. The interaction mechanism is formulated as in Table 2.1 below [44]:

Table 2.1 The interaction of sensor sample and oxygen

The type of reaction	Operating temperature (°C)	Chemical reaction
Physisorption		$O_2(gas) \leftrightarrow O_2(ads)$
Ionosorption	150 °C – 200 °C	$O_2(ads) + e^-(CB) \leftrightarrow O_2^-(ads)$
Ionosorption	Between 200 °C and 400 °C or higher	$O_2^-(ads) + e^-(CB) \leftrightarrow O_2^-(ads) \leftrightarrow 2O^-(ads)$
Ionosorption	Between 200 °C and 400 °C or higher	$O^-(ads) + e^-(CB) \leftrightarrow O^{2-}(ads)$ $O^{2-}(ads) \leftrightarrow O^{2-}(1st\ bulk\ layer)$

The gas detection in metal oxide semiconductor generally starts from reaction in air. At the thin film surface, when the working temperature of sensor between 150 °C and 400 °C or higher are applied, the oxygen molecule could be adsorbed by trapping conduction band electrons from the bulk. As a result, the resistance increases for the the sensor of *n*-type materials (the resistance will decrease for *p*-type materials). When the target gas interacts with the adsorbed oxygens, the electrons will be back to the surface resulted in decreasing of resistance (increasing of resistance for *p*-type materials) [55]. Based on this description, there are two kinds of important aspect in

the sensors. One is the reception function that related to the surface reaction taking place between the material and the gases. Another one is the transduction of receptor function that related to the change of the electrical sensor resistance.

On the semiconductor, the bulk conductance of thin films can be defined as:

$$G = Nq\mu\frac{wd}{L}$$

where N is a bulk carrier concentration, μ is the mobility of electrons, and w, d, L are width, film thickness and length, respectively [53].

The definition of conductance can be emerged into the current as:

$$I = GV = Nq\mu\frac{wd}{L}V$$

One of important parameters on the characteristic of gas sensor is the sensitivity. In general, the sensitivity can be defined as ratio of change of electrical conductance before and after exposed to target gas, ΔG, to conductance before exposed to target gas, G_0 (normally conductance in air). Then the sensitivity of gas sensors based on n-type materials for reducing gas can be defined as follows:

$$S = \frac{\Delta G}{G_o} = \left(\frac{G_g - G_o}{G_o}\right) = \left(\frac{I_g - I_o}{I_o}\right) = \frac{\Delta I}{I_o}$$

where G_0 and I_0 are the conductance and current before exposed to target gas, and G_g and I_g are the conductance and current after exposed to target gas, respectively. When resistance R (=1/G) is used as data in experiments, the sensitivity can be calculated using the relationship among resistance (R), current (I) and voltage (V) from basic ohm's law as below:

$$S = \frac{I_g - I_o}{I_o} = \frac{\frac{V}{R_g} - \frac{V}{R_o}}{\frac{V}{R_o}} = \frac{R_o - R_g}{R_g} = \frac{\Delta R}{R_g}$$

Note that the denominator of fraction is R_g, which is resistance after exposed to target gas. Depending on the data used in the experiments, we can calculate the sensitivity based on the above formulas. The slightly different definition to estimate the sensitivity has been also used in Ref 56, $S = \frac{R_{O_2}}{R_{O_2+CO}}$ that is also equivalent to form of $S = \frac{G_{O_2+CO}}{G_{O_2}}$. This type of definition for current was also used in Ref. 57. The ratio R_0/R_g and G_g/G_0 will be equivalent to $\Delta R/R_g$ and $\Delta G/G_0$ when ΔR and ΔG is large enough compared to R_g and G_0, respectively.

2.5 References

[1] Y. Chen, D. M. bagnall, H-J. Koh, K-T. Park, K. Hiraga, Z. Q. Zhu, and T. Yao, J. Appl. Phys. 84, 3912 (1998).

[2] A. Janotti and C. G. Van de Walle, Rep. Prog. Phys. 72, 126501 (2009).

[3] R. G. W. Wyckoff, Crystal Structures (Interscience, New York, 1963).

[4] H. Morkoc and U. Ozgur, Zinc Oxide: Fundamentals, Materials and Device Technology, Wiley-VCH, 2009.

[5] K. Ellmer, A. Klein, B. Rech, Transparent Conductive Zinc Oxide: Basics and Applications in Thin Film Solar Cells, Springer, 2007.

[6] F. Decremps, J. Zhang, R. C. Liebermann, Europhys. Lett. 51, 268 (2000).

[7] W. L. Bragg, Phil. Mag. 39, 647 (1920).

[8] D. R. Askeland and P. P. Phule, The Science and Engineering of Materials, Toronto: Thomson, Nelson, c2006.

[9] C. F. Klingshirn, B. K. Meyer, A. Waag, A. Hoffmann, J. Geurts, Zinc Oxide: From Fundamental Properties Towards Novel Applications, Springer-Verlag Berlin Heidelberg, 2010.

[10] A. R. West, Basic Solid State Chemistry, John Wiley & Sons Ltd, 1996.

[11] J. R. Williams, I. Pis, M. Kobata, A. Winkelmann, T. Matsushita, Y. Adachi, N. Ohashi, and K. Kobayashi, Journal of Applied Physics 111, 033525 (2012).

[12] M. W. Allen, D. Y. Zemlyanov, G. I. N. Waterhouse, J. B. Metson, T. D. Veal, C. F. McConville, and S. M. Durbin, Applied Physics Letters 98, 101906 (2011).

[13] R. Wahl, J. V. Lauritsen, F. Besenbacher, and G. Kresse, Physical Review B 87, 085313 (2013).

[14] D. C. Look, J. Electron. Mater. 35, 1299 (2006).

[15] D. C. Look, J. W. Hemsky, and J. R. Sizelove, Phys. Rev. Lett. 82, 2552 (1999).

[16] A. Janotti and C. G. Van de Walle, Rep. Prog. Phys. 72, 126501 (2009).

[17] P. Erhart and K. Albe, Appl. Phys. Lett. 88, 201918 (2006).

[18] M. D. McCluskey and S. Jokela, J. Appl. Phys. 106, 071101 (2009).

[19] A. Janotti and C. G. Van de Walle, Appl. Phys. Lett. 87, 122102 (2005).

[20] A. Janotti and C. G. Van de Walle, Phys. Rev. B 75, 165202 (2007).

[21] F. Oba, M. Choi, A. Togo, and I. Tanaka, Sci. Technol. Adv. Mater. 12, 034302 (2011).

[22] C. G. Van de Walle, Phys. Rev. Lett. 85, 1012 (2000).

[23] A. Janotti and C. G. Van de Walle, Nat. Mater. 6, 44 (2007).

[24] D. C. Look, G. C. Farlow, P. Reunchan, S. Limpijumnong, S. B. Zhang, and K. Nordlund, Phys. Rev. Lett. 95, 225502 (2005).

[25] Sheng S. L, Semiconductor Physical Electronics, 2nd edition, Springer (2006).

[26] S. Calnan, A. N. Tiwari, Thin Solid Films 518, 1839-1849 (2010).

[27] D. C. Look, K. D. Leedy, L. Vines, B and G. Svensson, A. Zubiaga and F. Tuomisto, D. R. Doutt and L. J. Brillson, Phys. Rev. B 84, 115202 (2011).

[28] K. Ellmer, A. Klein, B. Rech, Transparent Conductive Zinc Oxide, Basic and Applications in Thin Film Solar Cells, Springer-Verlag Berlin Heidelberg, 2008.

[29] H. Y. Liu, V. Avrutin, N. Izyumskaya, U. Ozgur, A. B. Yankovich, A. V. Kvit, P.M. Voyles, and H. Morkoc, J. Appl. Phys. 111, 103713 (2012).

[30] Y. S. Jung, O. V. Kononenko, and W. K. Choi, Solid State Commun. 137, 474 (2006).

[31] D. C. Look, K. D. Leedy, D. H. Tomich, and B. Bayraktaroglu, Appl. Phys. Lett. 96, 062102 (2010).

[32] J. Y. Seto, J. Appl. Phys. 46, 5247 (1975).

[33] T. Terasako, H.Song, H. Makino, S. Shirakata, T. Yamamoto, Thin Solid Films 528, 19-25 (2013).

[34] K. Wasa and S. Hayakawa, Handbook of Sputter Deposition Technology: Principle, Technology and Applications, Noyes publication, (1992).

[35] Magnetron Sputtering Technology, Micro Magneti, Inc, www.micromagnetics.com

[36] K. Ellmer and T. Welzel, J. Mater. Res. 27, 5 (2012).

[37] A. Bikowski and K. Ellmer, J. Appl. Phys. 114, 063709 (2013).

[38] Donald L. Smith, Thin Film Deposition: Principle and Practice, McGraw-Hill, 1995.

[39] G. Korotcenkov, S. H. Han, and B. K. Cho, J. Sens. Sci. Technol. 22, No 1, pp. 1-17 (2013).

[40] G. Korotcenkov, Mater. Sci. Eng. B 139, 1-23 (2007).

[41] S. Kishimoto, S. Akamatsu, H. Song, J. Nomoto, H. Makino, and T. Yamamoto, J. Sens. Sens. Syst., 3, 331-334 (2014).

[42] N. Al-Hardan, M. J. Abdullah, A. A. Aziz, and H. Ahmad, Appl. Surf. Sci. 256, 3468-3471 (2010).

[43] T. Tesfamichael, C. Cetin. C. Piloto. M. Arita, and J. Bell, Appl. Surf. Sci. 357, 728-734 (2015).

[44] N. Barsan and U. Weimar, J. Electroceram. 7, 143-167 (2001).

[45] N. Barsan, D. Koziej, and U. Weimar, Sens. Actuators B 121, 18-35 (2007).

[46] G. Korotcenkov, Sens. Actuators B 107, 209-232 (2005).

[47] H. Meixner, J. Gerblinger, U. Lampe, and M. Fleischer, Sens. Actuators B 23, 119-125 (1995).

[48] G. Korotcenkov and B. K. Cho, Sens. Actuators B 156, 527-538 (2011).

[49] K. Wetchakun, T. Samerjai, N. Tamaekong, C. Liewhiran, C. Siriwong, V. Kruefu, A. Wisitsoraat, A. Tuantranont, S. Phanichphant, Sens. Actuators B 160, 580-591 (2011).

[50] M. Fleischer and H. Meixner, J. Vac. Sci. Technol. A 17, 4 (1999).

[51] B. Yuliarto, L. Nulhakim, M.F. Ramadhani, M. Iqbal, Nugraha, Suyatman, and A. Nuruddin, IEEE Sensors Journal 15, 7 (2015).

[52] C. Wang, L. Yin, L. Zhang, D. Xiang and R. Gao, Sensors 10, 2088-2106, (2010).

[53] S. R. Morisson, Sens. Actuators 2, 329-341 (1982).

[54] S. Lenaerts, J. Roggen, and G. Maes, Spectrochimia Acta Part A-Molecular Spectroscopy, 51, 883 (1995).

[55] G. K. Mani, J. B. B. Rayappan, Mater. Sci. Eng. B 191, 41–50 (2015).

[56] X. Du and S. M. George, Sens. Actuators B 135, 152-160 (2008).

[57] A. Forleo, L. Francioso, S. Capone, P. Siciliano, P. Lommens, Z. Hens, Sens. Actuators B 146, 111-115 (2010).

3. Research Methodology

3.1 Thin Films Deposition

3.1.1 Substrate Cleaning

In this study, the GZO films were deposited on alkali-free glass substrates (Corning, Eagle XG) with diameters of 50 mm. Before use for sputtering deposition, the glass substrate was cleaned in an ultrasonic bath using two steps. Firstly, the glass substrate was degreased by 2-propanol around 10 minutes, then rinsed by deionized water around 10 minutes in order to ensure that no organic material remaining on the glass surface. After that the substrate was dried by nitrogen blow using nitrogen gun. Then the substrate was introduced to a load-lock chamber for depositions.

3.1.2 Films Growth

The GZO films were prepared by RF magnetron sputtering using an excitation frequency of 13.56 MHz. The GZO films were deposited on glass substrates using a ZnO ceramic target containing 5.7 wt % Ga_2O_3 (AGC Ceramics, GZO). The target dimension was 76.2 mm in diameter and 6 mm in thickness. The distance between the substrate and target was 100 mm. The base pressure of the deposition chamber was kept below $5x10^{-5}$ Pa, and ultra-high purity Argon gas (99.9999 %) was introduced during the sputtering deposition at a flow rate of 450 sccm and a RF power supply was about 100 W. The film thickness was confirmed by a surface profiler (KLA Tencor, Alpha-Step IQ). The substrates temperature (*Ts*) was varied from RT (Room Temperature) to 200 °C depending on purpose. Our sputtering system consists of two vacuum chambers, one is a load-lock chamber that used to introduce substrates without opening a main sputtering chamber, and another is the main sputtering chamber that used for deposition. The load-lock chamber and main chamber were evacuated by individual turbomolecular pumps in order to keep on required pressure during running on system. The pressure inside main chamber was controlled by Ar gas flow rates during depositions.

3.2 Electrical Measurements: Hall-Effect Measurements

The electrical properties have been characterized using HL5500PC Hall Effect Measurement System with HL5580 Buffer Amplifier. The partly content on this part was summarized from the user manual article of HL5500PC Hall Effect Measurement System with HL5580 Buffer Amplifier, User Manual Issue 4.0, Accent Optical Technologies. The complete user manual can be found in Ref 1.

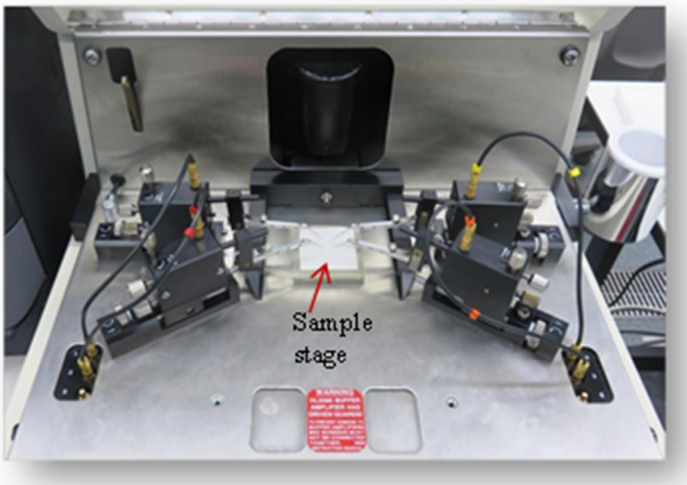

Fig. 3.1 Hall Effect Measurement System (Accent, HL5500PC)

Firstly, the sample was prepared in well-defined squared geometries and good ohmic contacts in order to obtain the accurate results. We putted small indium droplets at corners for some samples in order to obtain the ohmic contacts. Next, we performed resistivity measurements using geometry of van der Pauw as shown in Fig. 3.2 [1, 2].

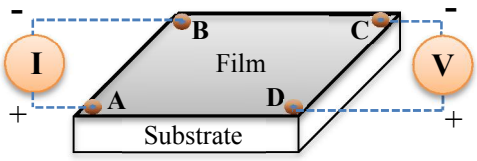

Fig. 3.2 Resistivity measurement on the van der Pauw method.

On this method, the sufficiently small of contact, the uniformity and homogenous of sample thickness and symmetrically placed or circumference of contact are necessary [1, 3]. On the van der Pauw method for ρ_s (sheet resistance) measurements, when the current and voltage are applied in parallel configuration, a resistance is obtained [2].

$$R_{AB,CD} = \frac{V_{DC}}{I_{AB}}$$

When the thickness of films t is known, a sheet resistance can be defined using bulk resistivity ρ as below:

$$\rho_s = \frac{\rho}{t} \rightarrow (\Omega/Sq)$$

Using this van der Pauw method as shown in Fig. 3.2, we can measure the Hall mobility and carrier concentration separately. In order to obtain the Hall mobility, the perpendicular configuration of current and voltage is applied from the same contact as shown in Fig. 3.3:

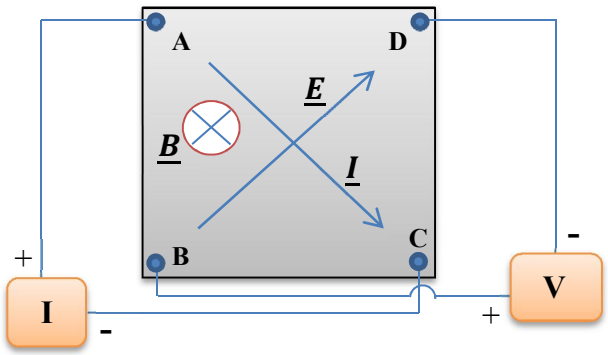

Fig. 3.3 Hall effects arrangement using van der Pauw measurements.

When magnetic field B is applied perpendicular to the film, the current I_{AC} will occur due to the charge carrier. The relationship between them can be expressed by the Lorentz force as below [1, 2, 4]:

$$F = F_E + F_B = q_e E + q_e v \times B$$
$$q\left(\underline{v \otimes B} \right) = q.E$$

where q is the elementary charge of an electron or hole and the electric field of $\underline{E}$ related to the magnetic field of $\underline{B}$ and the carrier of velocity $\underline{v}$. The F_B is perpendicular to the voltage (V) and magnetic field B.

The Hall voltage can be obtained by $V_h = E.W$. When R_H is defined as the Hall coefficient, then the R_H can be expressed as [1]:

$$R_H = \frac{1}{q.N} = \frac{V_h.t}{I.B}$$

Other formulation on the Hall system measurements can be expressed and summarized in Table 3.1 below [1]:

Table 3.1 Summarize of items formulation on Hall system measurements

Items	Equation	Units
Sheet Hall coefficient (when the thickness of active layer is known)	$R_{Hs} = \frac{R_H}{t} = \frac{V_h}{I.B}$	(m^2/C)
Carrier density N_s	$N_s = \frac{1}{q.R_{Hs}}$	(cm^{-2})
Bulk carrier density of N (with input the thickness t)	$N = \frac{1}{q.t.R_{Hs}}$	(cm^{-3})
Hall mobility (not depends on film thickness)	$\mu H = \frac{R_{Hs}}{\rho_s}$	(cm^2/V.s)

On the practical characterization, the samples were cut on dimension of 1x1 cm for each sample. The Hall effect measurements were performed at room temperature in this study.

3.3 Optical Measurements

Spectrophotometer consists of light sources, spectroscopes, a sample cell, and detectors. Generally, there are two types of light source, tungsten halogen lamps with wavelength range of 340-1100 nm and deuterium lamps with wavelength on the range 185-360 nm. The function of spectroscope is to selecting a monochromatic light from a light source (white light). The spectroscope consists of filters, prisms and diffraction gratings. The light that has transmitted from a film sample are detected and changed into an electric signal by a detector. A semiconductor photodiode and or a photomultiplier can be used as detectors.

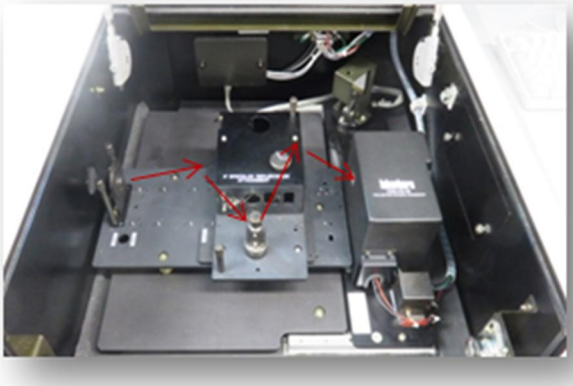

Fig. 3.4 The U-4100, Hitachi spectrophotometer system with 5° specular reflectance.

In this thesis, the optical properties of samples were characterized by a spectrophotometer Hitachi, U-4100 in the wavelength range from 200 nm to 2500 nm. The transmittance (T) and reflectance (R) measurements were performed with an angle of incidence for light at 5º. The reflectance of films properties does not appreciably change in an incident angle range of 0° to 5°. Thus, absolute reflectance at an incident angle of 5° were measured using a 5° specular reflectance unit [5]. The

incident angle of the system measurements is 5±1°. The detector is photomultiplier (UV-Vis)/cooled type PbS (NIR) integrated sphere whose inside wall is coated with $BaSO_4$ and the light source is a deuterium lamp for ultraviolet region and a 50W halogen lamp for visible-near infrared region. The set-ups of sample measurements are displayed as follows:

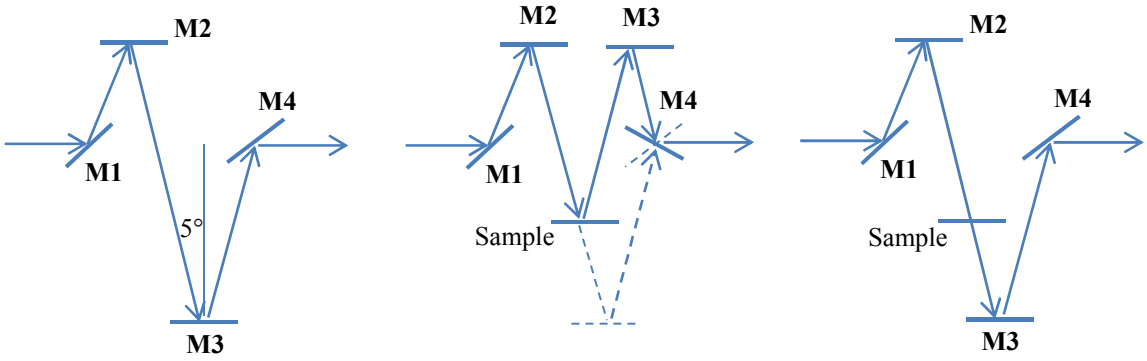

a) Reference b) Reflectance (*R*) c) Transmittance (*T*)

Fig. 3.5 The illustration of (b) Reflectance (*R*) and (c) Transmittance (*T*) measurement using incident angle of 5° specular reflectance. (Fig. 8 (a) is the geometry of reference position) [5].

Firstly, it is necessary to measure baseline as reference before practical sample measurements. The configuration set-up is illustrated as shown in Fig. 3.5 (a), i.e., without sample. Then for reflectance measurement the configuration is shown in Fig. 3.5 (b) while for transmittance is shown in Fig. 3.5 (c). Generally, the total intensity of light in the optical measurements can be written as:

$$I_0 = T + R + A$$

where A is the absorbance and I_0 is the total of incoming light intensity.

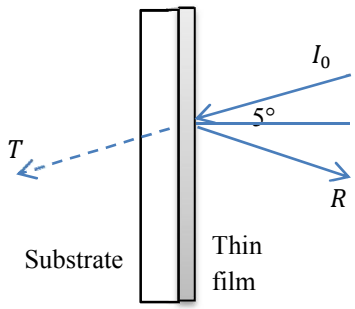

Fig. 3.6 The total of incoming light intensity in the optical measurements is equal to the total of Transmittance, Reflectance and Absorbance.

The relationship between incoming intensity I_0, the transmitted intensity I_t, the reflected intensity I_r, and the absorbed intensity I_a with the transmittance T, reflectance R and absorbance A can be calculated as below:

$$T = \frac{I_t}{I_0}$$

$$R = \frac{I_r}{I_0}$$

$$A = \frac{I_a}{I_0}$$

The total of T, R and A will be equal to 1 that can be written as:

$$1 = T + R + A$$

When the light transmitted through a film with thickness of d, having absorption coefficient α, the transmittance T can be approximated as follows [6]:

$$T = (1 - R)exp(-\alpha d)$$

Using this relationship, we can obtain α from measured T, R and d like as:

$$\alpha = \frac{1}{d} ln\left(\frac{1-R}{T}\right)$$

From the optical characterization, we can evaluate the optical band gap from the absorption coefficient, the optical mobility and the optical carrier concentration by simulation described in the following section.

3.4 Calculation of optical mobility

The optical mobility μ_{opt} can be deduced from an analysis of the reflection and transmission spectra or spectroscopic ellipsometry. On the doped ZnO based TCO, the dielectric function of bulk layer was modeled by combining the Drude model for response of free carriers and the Tauc-Lorentz (TL) model for optical bandgap. The TL model can be applied for dielectric function modeling of amorphous materials and TCOs materials [7]. The excellent fitting from various experimental data of TCO's, e.g., ZnO [8] and SnO_2 [9] has been confirmed by TL model. The dielectric function of TCO can be modeled as the following [7, 10]:

$$\varepsilon(E) = \varepsilon_1(E) - i\varepsilon_2(E)$$
$$\varepsilon(E) = \varepsilon_{TL}(E) + \varepsilon_D(E)$$

where $\varepsilon_{TL}(E)$ indicates the part of the Tauc-Lorentz model representing the optical band gap transition, and $\varepsilon_D(E)$ indicates the part of the Drude model representing the contribution of free carriers. The expression of the Drude model is given by [7]:

$$\varepsilon_D(E) = -\frac{A_D}{E^2 - i\Gamma_D E} = \left(-\frac{A_D}{E^2+\Gamma_D^2}\right) - i\left(\frac{A_D\Gamma_D}{E^2+\Gamma_D^2 E}\right)$$

Here, the amplitude A_D and the broadening parameter, Γ_D, are given by [7, 11]:

$$A_D = \frac{\hbar^2 e^2 N_{opt}}{m^* \varepsilon_0} \quad \text{and} \quad \Gamma_D = \frac{\hbar e}{m^* \mu_{opt}}$$

where $\hbar$, e, and m^* are the reduced plank constant, elementary charge, and effective mass, respectively. The value of Γ_D can be obtained by fitting the calculated transmittance (T) and reflectance (R) spectra to the experimental result. The μ_{opt} can be deduced from the expression of this formula, $\Gamma_D = \frac{\hbar e}{m^* \mu_{opt}}$. The empirical formula of m^* for ZnO, i.e., $m^*(\text{ZnO}) = (0.280 + 0.010 \times 10^{-20} N_{\text{Hall}})\, m_0$, referred to Ref. 7 (Fujiwara *et al*).

The typical fitting result for experimentally obtained transmittance and reflectance is shown in Fig. 3.7. The GZO film with thickness approximately 200 nm deposited at *Ts* of 200 °C was selected as example. The fitting shows well reproduced of *T* and *R* spectra especially in IR wavelength region governed by free carriers.

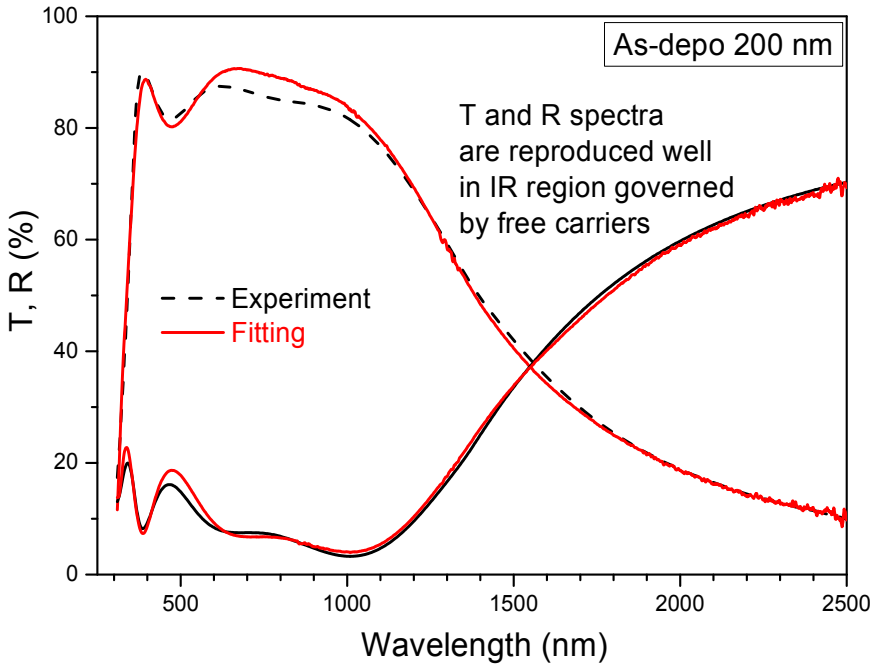

Fig. 3.7 The typical fitting based on the simulation of 200 nm thick GZO films that shows T and R spectra are reproduced well in IR region governed by free carriers.

3.5 Evaluation of In-grain and grain boundary scattering

Generally, the Hall mobility is limited by the contributions of several scattering mechanisms based on Matthiessen's rule [7, 12]. The in-grain mobility in heavily doped semiconductors is limited by ionized impurity scattering, optical phonon scattering, and scattering by defects [7]. In the case of polycrystalline films, the Hall mobility can be also affected by grain boundary scattering even in the very high doping regime [13]. To evaluate the contribution of grain boundary scattering, we employed optical mobility obtained from optical measurements as already mention in part of 2.4. The optical mobility exhibits a close relationship with the in-grain mobility [7, 11, 14, 15], even though there is still a debate and discussion on the origin of the difference between the Hall mobility and the optical mobility. The difference between the μ_{opt} and μ_{Hall} has been reported in several studies [12, 14, 16, 17]. However, the cause of the difference is not so clear at the present. One explanation is the contribution of grain boundary scattering to the Hall mobility [12, 17]. Here, we tentatively attribute the difference to the grain boundary scattering. The μ_{opt} will not be affected by the grain boundary scattering [17]. Considering that the optical mobility corresponds to the in-grain mobility, the Hall mobility can be expressed as follows [12, 14]:

$$\frac{1}{\mu_{hall}} = \frac{1}{\mu_{opt}} + \frac{1}{\mu_{gb}}$$

Based on the equation above, we can say that the μ_{Hall} is equal to or near to be similar with the μ_{opt}, when $\frac{1}{\mu_{gb}}$ value near to zero. This means that the contribution of grain boundary scattering to the Hall mobility is less or nearly negligible. Schematics of mobility determined by the in-grain scattering (μ_{ig}) and the grain boundary scattering (μ_{gb}) on doped ZnO are illustrated in Fig. 3.8, as below:

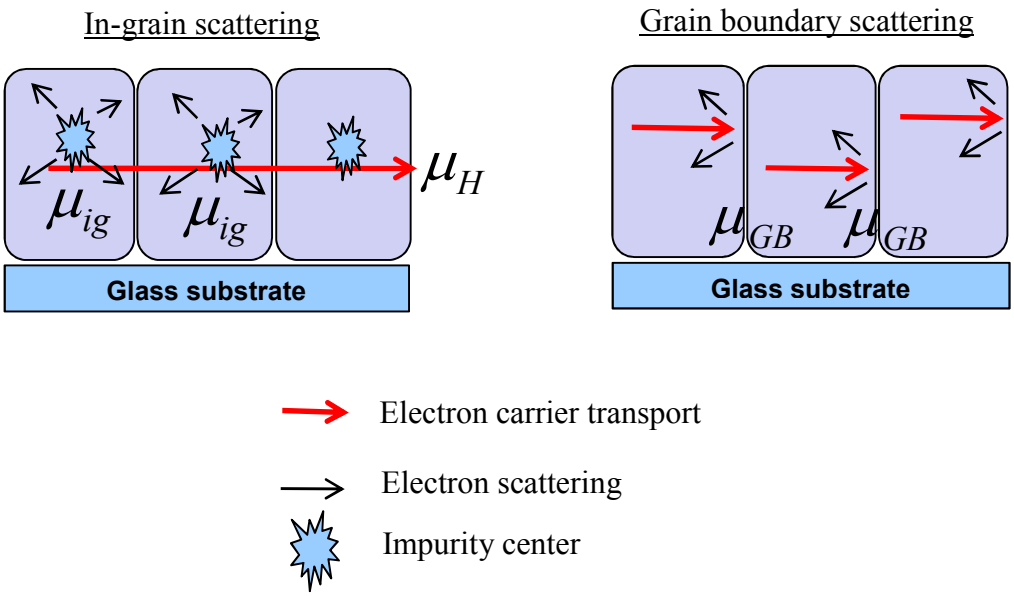

Fig. 3.8 The illustration of μ_{ig} and μ_{gb} on the transport properties of doped ZnO based TCO. The red arrow is electron carrier transport path and the black arrow is electron scattering path.

3.6 Structural Measurements: X-Ray Diffraction

A powerful tool to determine the structural properties of materials is X-ray diffraction (XRD) method. The out-of-plane method with scan axis $2\theta/\omega$ and in-plane measurement with scan axis $2\theta\chi/\varphi$ are two general methods in characterization of thin films. As a part of out-of-plane measurement, the degree of *c*-axis orientation can be characterized using the ω rocking curve technique.

As shown in Fig. 3.9, the instrument of XRD for thin films basically consists of X-ray source, incident optical system, goniometer, receiving optical system, and detection system. In general, the diffractometer is composed by four axes, i.e., the sample rotation axis ω as also called the θ axis in conventional XRD measurement for powder, the tilting axis χ, the in-plane rotation axis φ, and the 2θ axis for scanning

the detector. The sample rotation of ω axis is commonly controlled independent of the 2θ axis in XRD thin film measurements [18].

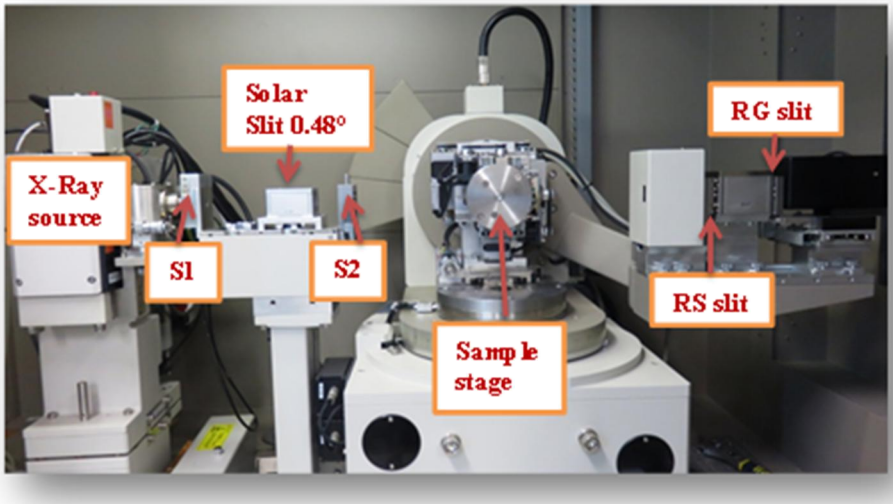

Fig. 3.9 X-ray diffraction (XRD), Rigaku ATX-G system with Cu Kα X-ray source (wavelength of 0.15418 nm).

The out-of-plane diffraction measurement is the most generally used method for characterization of thin films. In this measurement, measurable planes are parallel to the surface of films. In the case of *c*-axis oriented ZnO thin films, *c*-plane can be measured using this method. The geometries of the out-of-plane measurement are shown in Fig. 3.10 [19]:

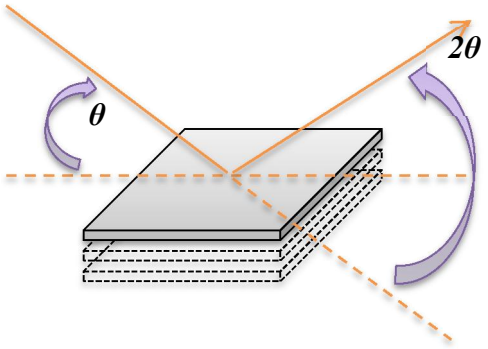

Fig. 3.10 The geometry of out-of-plane XRD measurements.

On the polycrystalline films, the degree of orientation is one kind of important structural parameters, which determines properties of the films. In order to characterize the degree of preferred orientation, a ω rocking curve measurement gives useful information regarding tinting of crystal axis as shown in Fig. 3.11.

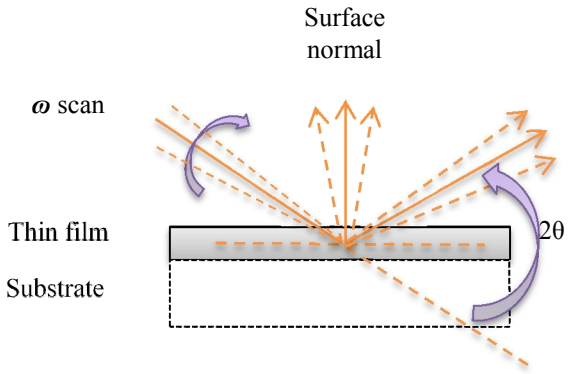

Fig. 3.11 The geometry of XRD rocking curve measurement. (Figure adapted from Ref. 19, with modification).

On the rocking curve measurement, the detector is kept on fixed angle of 2θ in order to estimate the intensity of diffraction for preferentially-oriented lattice planes, and the incident angle ω is scanned. The value of a FWHM (full width at half maximum) estimated from the rocking curve profile gives how largely tilting the oriented planes each other [19].

The in-plane measurement is usually used for measuring diffraction from lattice planes perpendicular to the surface of films. Another characteristic of this measurement that the diffraction of an extremely thin film can be obtained [20]. The geometry of in-plane measurement is shown in Fig. 3.12.

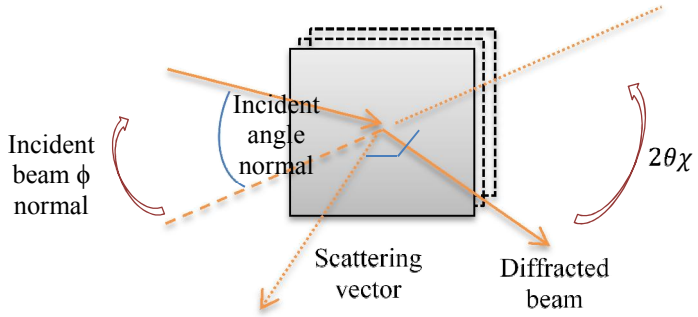

Fig. 3.12 The geometry of in-plane XRD measurement. (Figure referred to Ref. 19, with modification).

On the practical measurement in this thesis, the measurement of out-of-plane has been done in the range of 2θ from 20° to 80° using a Ni filter to cut Kβ radiation, with sampling step of 0.02° and scan speed of 2°/min, whereas for in-plane measurement, the measurement was on the range from 20° to 120°. The scan speed was adjusted depending on measured samples in order to obtain enough signal to noise ratio of each peaks. All of the sample measurement has been done using Cu Kα radiation X-ray source with wavelength of 0.15418 nm. The measurement was controlled by ATX-G operation software.

The out-of-plane and in-plane measurements were also used for calculation of *c*-axis lattice constant from 0002 peak, *a*-axis lattice constant from $10\bar{1}0$ peak, and volume of unit cells from hexagonal wurtzite type using equation of $V = 0.866a^2c$. On the other hand, the grain size was evaluated using Williamson-Hall plot analysis [21]. The five main peaks in in-plane measurement, i.e., $10\bar{1}0$, $11\bar{2}0$, $20\bar{2}0$, $21\bar{3}0$, and $30\bar{3}0$ peaks were used for the estimation of grain size.

3.7 Valence Band Measurements: X-Ray Photoemission Spectroscopy

One of the most powerful techniques for analysis of electronic structure of materials is X-ray photoelectron spectroscopy (XPS). The principle of XPS is based on the effect of photoelectric. The kinetic energy of photoelectrons can be analyzed by the XPS system. The kinetic energy *KE* of emitted electrons can be expressed as below in relationship with their initial state of electrons and photon energy of X-ray used for excitation [22]:

$$KE = hv - BE - \phi_s$$

where photon energy of X-ray was represented by hv, binding energy by BE and work function of spectrometer indicated by ϕ_s.

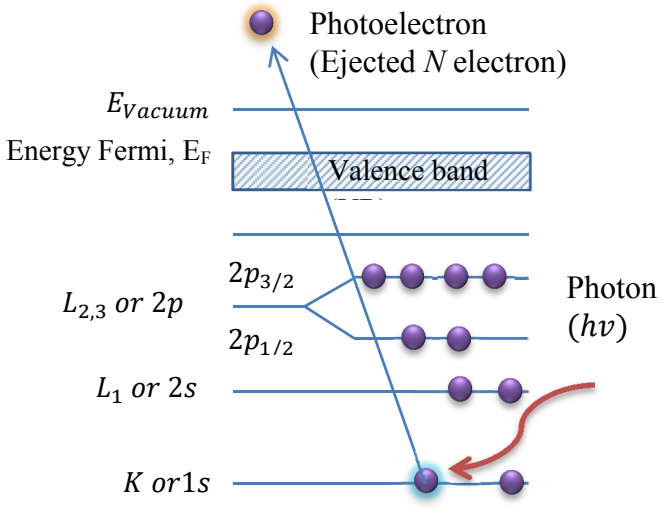

Fig. 3.13 The photoemission on the XPS system process.

Binding energy of ejected photoelectron can be indicated by the final state configuration after photoemission. Fig. 3.13 shows the XPS emission process for a

model atom. The ejected *N* electron was caused by an incoming of incident X-ray (Photon). The kinetic energy of ejected electrons will be analyzed by electron spectrometer. On the practical XPS measurements, graph of count versus binding energy of electrons are usually used for analysis.

An electron spectroscopy on the XPS system usually consists of a source of the primary beam, either of X-rays or electron, an energy analyzer and the detection system. All of these modules enclosed within a vacuum chamber. In order to comply with the issue of surface sensitivity of the measurement techniques, the vacuum systems are intended to operate in the ultra-high vacuum (UHV) in the order of 10^{-8} Pa. In order to overcome the binding energies of electron core level, the X-ray source on the XPS system must produce enough energetic beams. The most commonly used X-ray source in XPS systems are Mg Kα (1253.6 eV with linewidth 0.7 eV), Al Kα (1486.6 eV with linewidth 0.85 eV) or monochromatic Al Kα (1486.7 eV). Penetrating power as effect of this photon energy is limited on the order of 1-10 micrometers [22]. In the case of High Energy XPS (HE-XPS) or hard X-ray XPS (HAX-PES), the Cr Kα line with photon energy of about 5414.87 eV can be used for bulk sensitive analysis reach to 20 nm without any surface treatment.

A custom-made HE-XPS system equipped with Al Kαand Cr Kα X-ray sources provides surface sensitive and bulk sensitive measurements, respectively, in one equipment. The system is illustrated in Fig. 3.14 [23]. In this thesis, valence band spectra were measured by the custom-made HE-XPS system using a wide acceptance angle electron analyzer (VG Scienta EW4000) and a Cr Kα X-ray source with the photon energy of 5414.87 eV (ULVAC-PHI).

The sample measurement was performed under UHV condition. The base pressure inside the chamber reached to as high as 7 x 10^{-8} Pa. The chamber was utilized by two turbo molecular pumps in order to evacuate the system reach to the ultra-high

vacuum level. In this system, the XPS chamber is connected to the load lock chamber of sputtering system for in-situ measurements after deposition of films.

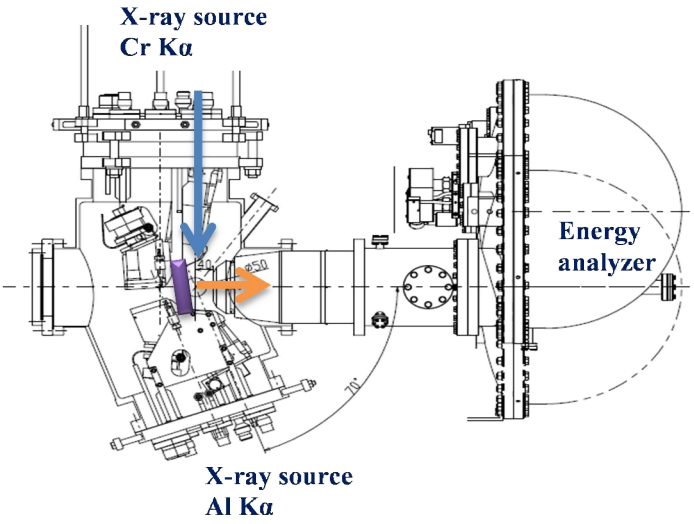

Fig. 3.14 HE-XPS system with a wide acceptance angle electron analyzer (VG Scienta EW4000) and X-ray sources of Cr Kα and Al Kα (ULVAC-PHI).

3.8 Hydrogen gas sensor measurements

The evaluation of gas sensor response was performed by a custom-made set-up for gas sensing measurements. The layout of system can be seen in Fig. 3.15. The GZO film was prepared on the dimension of 5 mm to 5 mm with two area of Au electrode (distance between electrode was about 1 mm for each other). The sample was placed on the compact cylindrical chamber with volume of approximately 200 cm^3 for the sensor test measurement. Change of resistance and sensitivity of sensors was extracted from the current data of films that evaluated using a system source meter (2602A, Keithley), with an applied voltage of 3V under operating temperature of 330 °C. A ceramic heater settled under the sample was used to control the operating temperature. Pure N_2 gas was continuously flowed into the sample chamber at a flow rate of 300 sccm, and then 1% H_2 and N_2 gas mixture was introduced at a flow rate of 100 sccm as target gas in the sensing measurements. The flowing time of the target gas was 10 s for each sample measurements. The evacuation and releasing gas was

done in the atmospheric pressure through gas inlet and outlet in the system test chamber [24].

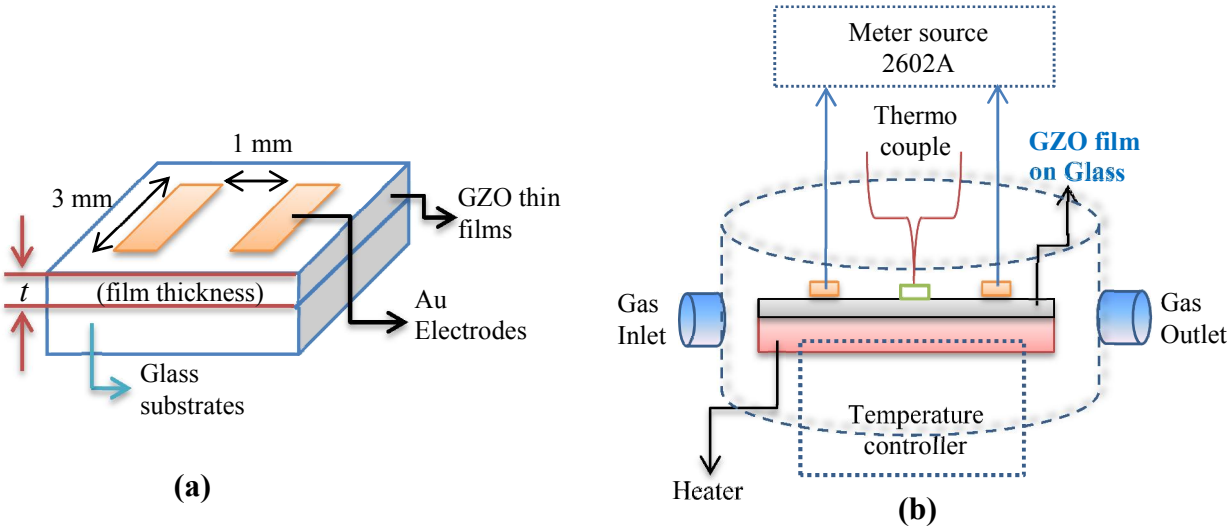

Fig. 3.15 Schematics of gas sensing measurements, (a) geometry of thin film sample for measurements and (b) set-up of sensing test measurements (The figure referred to Ref. 24, with modification).

3.9 References

[1] HL5500PC Hall Effect Measurement System with HL5580 Buffer Amplifier, User Manual Issue 4.0, Accent Optical Technologies, England, 2001.

[2] Donald. L. Smith, Thin Film Deposition: Principle and Practice, McGraw-Hill, Inc. 1995.

[3] L. Van Der Pauw, Philips Research Reports 13, 1-9 (1958).

[4] C. Kittel, Introduction to Solid State Physics, John wiley & Sons, Inc. 2005.

[5] Instruction manual, U-4000/U-4100 spectrophotometer system with 5° specular reflectance, Hitachi, 1994.

[6] H. Makino, T. Yamada, N. Yamamoto, and T. Yamamoto, Thin Solid Films 519, 1521-1524 (2010).

[7] H. Fujiwara and M. Kondo, Phys. Rev. B 71, 075109 (2005).

[8] H. Fujiwara, M. Kondo, and A. Matsuda, J. Appl. Phys. 93, 2400 (2003).

[9] P. I. Rovira and R. W. Collins, J. Appl. Phys. 85, 2015 (1999).

[10] G. E. Jellison, Jr. and F. A. Modine, Appl. Phys. Lett. 69, 371 (1996).

[11] H. Makino, N. Yamamoto, A. Miyake, T. Yamada, Y. Hirashima, H. Iwaoka, T. Itoh, H. Hokari, H. Aoki, T. Yamamoto, Thin Solid Films 518, 1386-1389 (2009).

[12] T. Yamada, H. Makino, N. Yamamoto, T. Yamamoto, J. Appl. Phys. 107, 123534 (2010).

[13] A. Bikowski and K. Ellmer, J. Appl. Phys. 116, 143704 (2014).

[14] J. Nomoto, H. Makino, T. Yamamoto, J. Appl. Phys. 117, 045304 (2015).

[15] T. Yamamoto, H. Song, and H. Makino, Phys. Status Solidi C 10, 603-606 (2013).

[16] H. Makino, N. Yamamoto, A. Miyake, T. Yamada, Y. Hirashima, H. Iwaoka, T. Itoh, H. Hokari, H. Aoki, T. Yamamoto, Thin Solid Films 518, 1386-1389 (2009).

[17] J. Steinhauser, S. Fay, N. Oliveira, E. Vallat-Sauvain, C. Ballif, Appl. Phys. Lett. 90, 142107 (2007).

[18] K. Inaba, The Rigaku Journal 24, 1 (2008).

[19] T. Mitsunaga, The Rigaku Journal 25, 1 (2009).

[20] S. Kobayashi, The Rigaku Journal 26, 1 (2010).

[21] G. K. Williamson and W. H. Hall, Acta Metall. 1, 23-31 (1953).

[22] J. F. Moulder, W. F. Stickle, P. E. Sobol, K. D. Bomben, Handbook of X-ray Photoelectron Spectroscopy, ULVAC-PHI, Inc Japan and Physical Electronics USA, 1995.

[23] H. Makino, H. Song, T. Yamamoto, M. Kobata, and K. Kobayashi, E-MRS meeting, poster presentation, France, 2014.

[24] S. Kishimoto, S. Akamatsu, H. Song, J. Nomoto, H. Makino, and T. Yamamoto, J. Sens. Sens. Syst. 3, 331 (2014).

4. Controlling of microstructure and annealing out of defects: their effects on properties

4.1 Introduction

In the last decade, there has been a growing interest on using transparent conducting oxides (TCOs) as materials for transparent electrodes [1]. Heavily doped ZnO, such as Ga-doped ZnO (GZO) and Al-doped ZnO (AZO), are promising candidates as alternatives to indium tin oxide (ITO) which is the most commonly used TCO in displays, due to low resistivity, high transparency, low cost, and non-toxicity of ZnO [2, 3]. ZnO-based TCOs have been developed for transparent electrodes in optoelectronic applications, such as thin film photovoltaics [4], flat panel displays [5], and light emitting diodes [6]. Currently, most of the research on ZnO-based TCOs has focused on transport properties, e.g., influences of intrinsic defects on transport [7, 8], scattering mechanisms limiting the carrier mobility [9, 10], and relationship between micro structural properties and transport [11-13]. The effect of crystallographic microstructural properties, similar to grain boundaries, on carrier transport in heavily doped ZnO has been extensively discussed, especially in polycrystalline films [11-16]. However, this is not clearly understood. Therefore, there are still some interesting and relevant problems to be addressed.

Doped ZnO films can be prepared by several deposition methods, such as magnetron sputtering, pulsed laser deposition (PLD), evaporation, metal organic chemical vapor deposition (MOCVD), spray pyrolysis, and electrochemical deposition [17]. Radio frequency (RF) magnetron sputtering is one of deposition methods that is currently used to produce dense and high quality films even at low temperatures below 200 °C. Doped ZnO films deposited by magnetron sputtering on heated substrates at approximately 250 °C have shown better electrical and optical properties than those deposited at room temperature (RT) without heating the substrates. It is well known that polycrystalline ZnO films deposited on heated glass substrates shows high orientation in the *c*-axis normal to the substrate surface, while ZnO films deposited at

RT show rather poor crystallinity. On the other hand, it has been noted that some point defects caused by ion bombardment could be annealed out during the deposition of AZO films on heated substrates [18]. Both the point defects and microstructural properties can affect the transport properties of doped ZnO films. Thus, in order to improve the RT deposition, it is necessary to understand the effects of heated substrates on the growth of polycrystalline GZO films in more detail.

In this chapter, we study the effects of heated substrates on the properties of GZO films deposited by RF magnetron sputtering, in terms of the microstructural properties and annealing out the point defects separately, by combining microstructural control and post deposition annealing. The microstructure is controlled by a buffer layer, and a post deposition annealing was employed in order to anneal out the defects.

The main part of this chapter has been published in Thin Solid Films as listed in page of Publications. (*L. Nulhakim and H. Makino, Thin Solid Films 615, 158-164 (2016)*)

4.2 Experimental details

GZO films were prepared by RF magnetron sputtering using an excitation frequency of 13.56 MHz. The GZO films were deposited on alkali-free glass substrates (Corning, Eagle XG) with diameters of 50 mm using a ZnO ceramic target containing 5.7 wt % Ga_2O_3 (AGC Ceramics, GZO). The target dimension was 76.2 mm in diameter and 6 mm in thickness. The distance between the substrate and target was 100 mm. The base pressure of the deposition chamber was kept below $5x10^{-5}$ Pa, and ultra-high purity Argon gas (99.9999 %) was introduced during the sputtering deposition at a flow rate of 450 sccm. The pressure in the chamber during the deposition was ~ 0.3 Pa, and the supplied RF power was 100 W.

Three types of GZO films were prepared in this study. A GZO film with a thickness of approximately 200 nm was deposited at RT on an unintentionally heated glass

substrate (named RT). In order to control the microstructure of the GZO film, we employed a 40 nm thick GZO film deposited at 200 °C as a self-buffer layer or a seed layer. The 40 nm thick GZO film was first deposited at 200 °C, followed by a deposition of a 160 nm thick GZO film at RT after sufficiently cooling down the substrate temperature (named RT/Buffer). The total film thickness was approximately 200 nm. A200 nm thick GZO film was also deposited at a substrate temperature of 200 ºC as a reference (named HT). In order to explore the influence of thermal annealing on the films, the GZO films were annealed at 200 °C in the deposition chamber after the deposition under a flowing Ar gas at 450 sccm, which was in a comparable environment as that during the deposition. Then, the properties of the films before and after the post deposition annealing were compared.

The crystal structural properties of the GZO films were characterized by X-ray diffraction (XRD) using Cu Kα radiation (wavelength of 0.15418 nm) (Rigaku, ATX-G system) with out-of-plane and in-plane measurements. Transmittance (T) and reflectance (R) measurements were performed with an angle of incidence for light at 5º by a spectrophotometer (Hitachi, U-4100). The electrical properties of the GZO films were investigated by a Hall Effect measurement system (Nanometrics, HL5500PC) at room temperature using the van der Pauw method to obtain the resistivity, the carrier concentration, and the Hall mobility.

4.3 Experimental results and discussion

4.3.1 Structural properties

Fig. 4.1 shows the out-of-plane (2θ - ω) XRD patterns of the GZO films, i.e., RT (a), RT/Buffer (b), and HT (c).The out of plane XRD pattern for the film with the self-buffer layer (RT/Buffer) showed a strong *c*-axis orientation, as indicated by intense 002 and 004 diffraction peaks at approximately 34.4° and 72.6°, respectively. It can be observed that the intensity of each diffraction peak was comparable with those of the GZO film deposited at 200 °C (HT). On the other hand, for the GZO film without the self-buffer layer (RT), the XRD pattern also showed a preferred orientation in the

c-axis; however, it showed a poor crystallinity and poor *c*-axis orientation, i.e., the intensity of the 002 peak of the RT film was one order of magnitude lower than that of the RT/Buffer film. In addition to the 0002 and 0004 diffraction peaks, very weak peaks were also observed, corresponding to the $10\bar{1}1$, $10\bar{1}2$, and $10\bar{1}3$ diffractions. This observation indicated that the *c*-axis orientation was not fully realized in the low temperature deposition on the unintentionally heated substrate at room temperature.

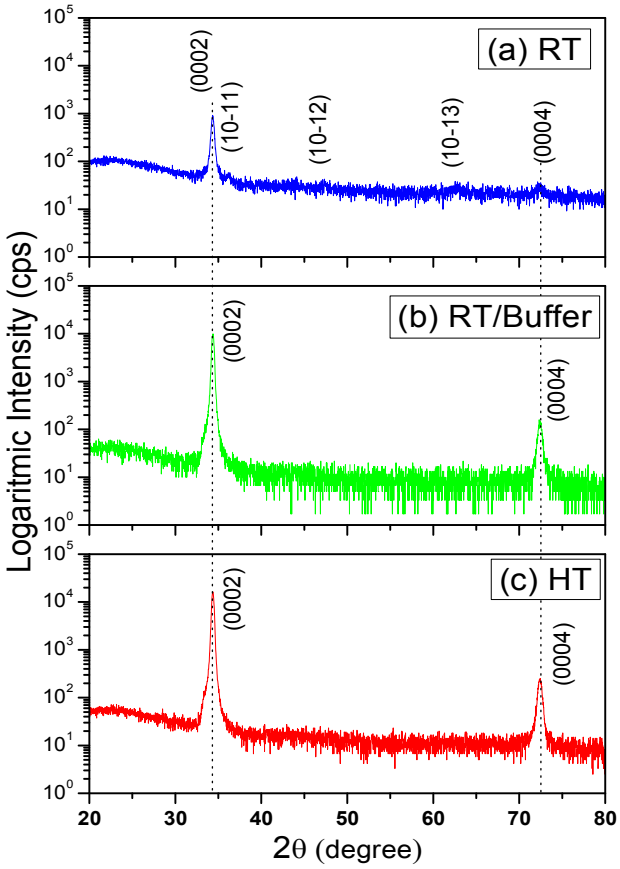

Fig. 4.1 Out-of-plane 2θ-ω scan for GZO films deposited on glass substrates at (a) RT, (b) RT/Buffer, and (c) HT.

In order to evaluate the degree of *c*-axis orientation, we compared 0002 ω-rocking curves. The full-width half-maximum (FWHM) of the ω-rocking curve of the RT film was approximately 12 degrees. In contrast, the FWHM of the ω-rocking curve of the

RT/Buffer film was approximately 4 degrees. This value was comparable with that of the HT film, which showed a FWHM of approximately 3.7 degrees.

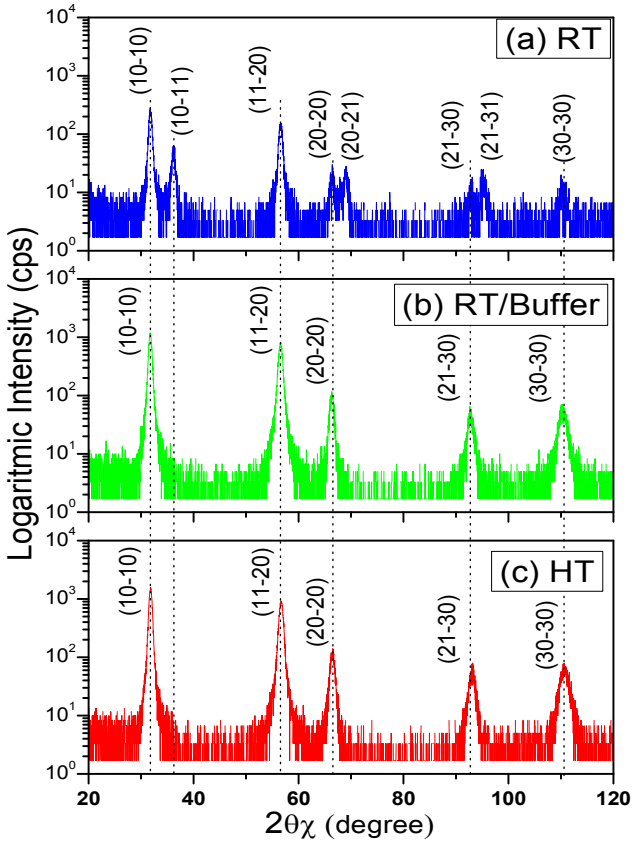

Fig. 4.2 In-plane 2θχ-φ scan for GZO films deposited on glass substrates at (a) RT, (b) RT/Buffer, and (c) 200 ºC.

Fig. 4.2 shows the in-plane XRD patterns of the GZO films, i.e., RT (a), RT/Buffer (b), and HT(c). The in-plane XRD patterns of RT/Buffer (b) showed five diffraction peaks: $10\bar{1}0$, $11\bar{2}0$, $20\bar{2}0$, $21\bar{3}0$, and $30\bar{3}0$, which corresponded to the crystal lattice planes perpendicular to the *c*-plane of wurtzite ZnO. This observation also indicated highly oriented GZO film by inserting the self-buffer layer. On the other hand, we observed the diffraction peaks of $10\bar{1}1$, $20\bar{2}1$, and $21\bar{3}1$, in addition to the five diffraction peaks, in the case of the RT film (a). This characteristic also suggested

that the GZO film deposited at the low temperature was not yet well oriented in the *c*-axis perpendicular to the substrate surface.

These observations in the out-of-plane and in-plane XRD measurements confirmed that the insertion of the self-buffer layer resulted in a highly *c*-axis orientation, which was comparable with the higher temperature deposition at 200 °C.

It is well known that post deposition annealing can lead to changes of microstructural properties resulting in the improvement of electrical properties [18]. We also performed out of plane and in-plane XRD measurements on the GZO films after post deposition annealing. However, there were no significant changes of structural properties after post deposition annealing regarding the *c*-axis orientation or the grain size. This was because of the rather low annealing temperature of 200 °C.

The lattice constants and unit cell volumes of the GZO films are summarized in Table 4.1. The change in the lattice constants showed different characteristics between the low temperature deposition at RT and the higher temperature deposition at 200 °C. For the as-deposited GZO films, the *a*-axis lattice constants of the films deposited at RT, i.e., the RT and RT/Buffer films, were a little larger compared to that of the HT film. The *a*-axis decreased after annealing, and the values became nearly identical with each other. On the other hand, the *c*-axis lattice constants of the as-deposited films were nearly identical with each other; however, the values were enlarged after annealing for the RT and RT/Buffer films. The unit cell volumes of the RT and RT/Buffer films were a little larger than that of the HT film. It should be noted that the change was not dependent on the degree of *c*-axis orientation but was dependent on the deposition temperature. The different behavior of the lattice constants depending on the deposition temperature might be due to defects in the films deposited at RT, which will be discussed later.

Table 4.1 The *a*-axis lattice constant (a), *c*-axis lattice constant (c) and volume of unit cells (V) of GZO films deposited at RT, RT/Buffer and HT.

GZO films	As-deposited			Annealed		
	a (Å)	c (Å)	V (Å)	a (Å)	c (Å)	V (Å)
RT	3.254	5.222	47.78	3.249	5.227	47.77
RT/Buffer	3.250	5.218	47.85	3.250	5.221	47.75
HT	3.248	5.219	47.69	3.248	5.217	47.66

We also evaluated grain size from the in-plane XRD. The grain size of as-deposited films increased after inserting the buffer layer. The grain size was ~ 21 nm for the RT film, while the grain size increased to ~ 28 nm for the RT/Buffer film. The grain size of the HT film deposited at 200 °C was ~ 38 nm, which is larger than the others. However, the grain size showed nearly no change after post deposition annealing.

From the results of structural properties, the *c*-axis orientation of GZO films deposited at RT was improved by inserting a self-buffer layer, while no contribution of post deposition annealing to the improvement of structural properties was observed.

4.3.2 Electrical properties

Fig. 4.3 shows the variations of the resistivity, ρ (a), the carrier concentration, *N* (b), and the Hall mobility, μ_{Hall} (c), of the GZO films. First, the as-deposited GZO films will be discussed. The RT film showed the highest resistivity. The resistivity of the RT/Buffer film was lower than that of the RT film, but was still higher than that of the HT film. It can be observed that the carrier concentration only depended on the deposition temperature regardless of the control of microstructure. The carrier concentration was nearly identical for the RT and RT/Buffer films, which was lower than the HT film. The Hall mobility was also dominated by the deposition temperature, although it was slightly improved by the control of microstructure. The Hall mobility of the RT/buffer film was slightly higher than the RT film; however, even the Hall mobility of the RT/buffer film was very low compared to the HT film.

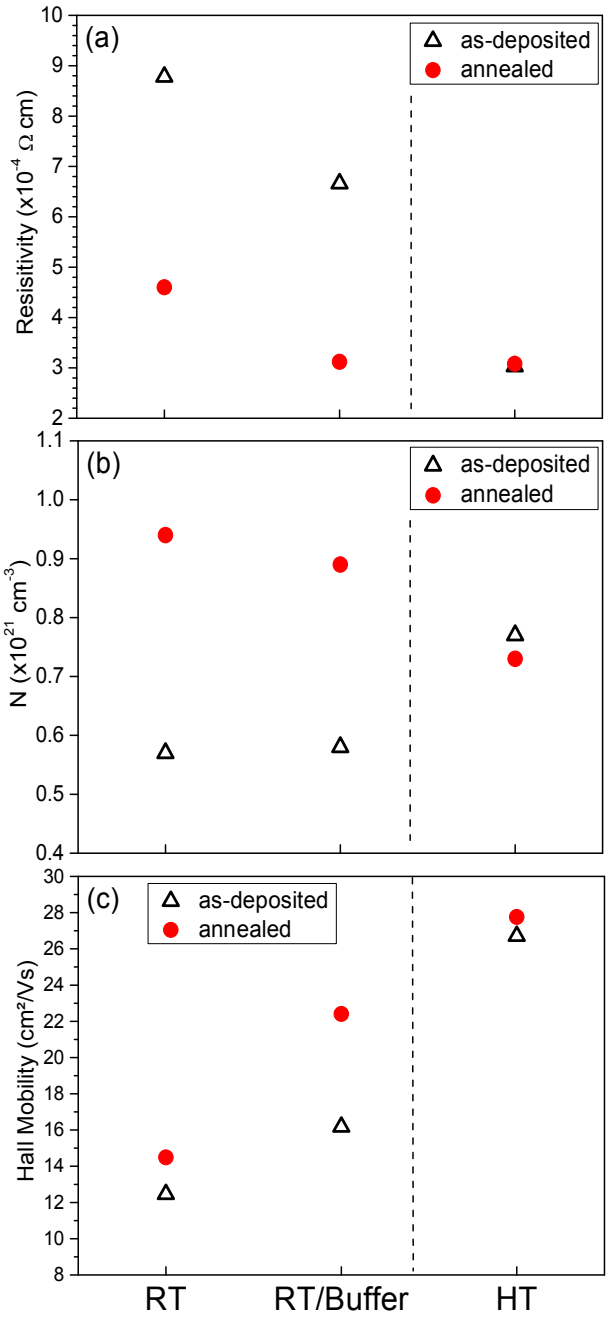

Fig. 4.3 Resistivity ρ (a), carrier concentration *N* (b), and Hall mobility μ_{Hall} (c) of the GZO films, i.e., the RT, RT/Buffer, and HT films, obtained by Hall effect measurement at room temperature.

Next, the effect of the post deposition annealing will be discussed. Nearly no changes in the electrical properties were observed in the HT film (200 °C) before and after annealing. This was reasonable because post deposition annealing was conducted under nearly the same condition as the deposition of the HT film. In the case of the films deposited at room temperature (the RT, and the RT/Buffer), the resistivity drastically decreased after annealing. The resistivity of the RT/Buffer film after annealing was eventually comparable with that of the HT film. However, the resistivity of the RT film was still higher than that of the others even after annealing. It can be observed that the decrease of the resistivity by annealing was due to the increase of carrier concentration, and the characteristics were nearly the same between the RT and RT/Buffer films.

Although the change of carrier concentration by post deposition annealing was nearly the same for the RT and RT/Buffer films, the change of the Hall mobility showed clear differences between the RT and RT/Buffer films. The Hall mobility of the RT/Buffer increased from 16 cm^2/Vs to 22 cm^2/Vs after annealing; however, the Hall mobility of the RT film did not change significantly, i.e., from 12 cm^2/Vs to 14 cm^2/Vs after annealing. It should be noted that the limited change in the Hall mobility resulted in a higher resistivity of the RT film even after annealing.

Because the change of electrical properties by annealing has often been considered as events limited at the surface region, we also confirmed the change of the carrier concentration through another route, i.e., using optical absorption spectra. It is known via the Burstein-Moss effect that the fundamental optical band gap, E_g, is widened linearly with $N^{2/3}$ [20, 21] because of the change of population in the conduction band and is narrowed with increasing carrier concentration because of band gap renormalization [20]. The absorption coefficient, α, can be obtained using the following formula:

$$\alpha = \frac{1}{d} ln\left(\frac{100-R}{T}\right) \quad (1)$$

where d is the film thickness, and R and T are the % of reflectance and % of transmittance, respectively. In this study, E_g was estimated from the maximum of $\frac{d\alpha}{dE}$ according to the literature [20, 21]. α and E are the absorption coefficient and photon energy, respectively. The estimated E_g values are plotted in Fig. 4.4. It was revealed that the change of E_g was consistent with the change of the carrier concentration evaluated by the Hall effect measurement. Although a quantitative discussion in the dependence of the E_g on the carrier concentration is beyond the scope of the present study, the results here showed the increase of carrier concentration after post deposition annealing regardless of the existence of a self-buffer layer.

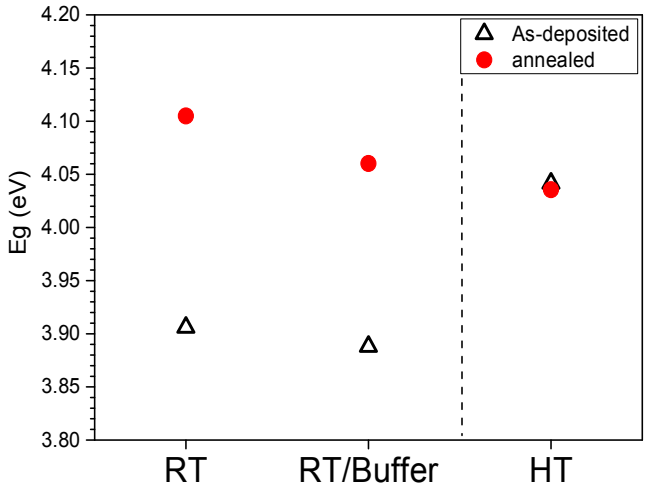

Fig. 4.4 Variations in the optical band gap E_g of the GZO films, i.e., the RT, RT/Buffer, and HT films.

The enhancement of carrier concentration after post deposition annealing in the sample deposited at RT (Fig. 4.3 (b)) can be related to the annealing out of acceptor type defects, such as zinc vacancy, V_{Zn} [8, 22], and/or oxygen interstitial O_i [18]. Such defects were already annealed out during the deposition of the GZO film at 200 ºC, which resulted in the higher carrier concentration of the HT sample.

4.3.3 Optical properties

We studied optical absorption possibly related to defects in the GZO films. Fig. 4.5 (a) and (b) show the absorption spectra of GZO films before and after annealing for the RT (a) and RT/Buffer (b) films, respectively. The absorption spectra of the HT film were also plotted as a reference. We observed rather strong optical absorption in the visible region in the as-deposited GZO films. It can be observed that the absorption band clearly decreased after the post-deposition annealing.

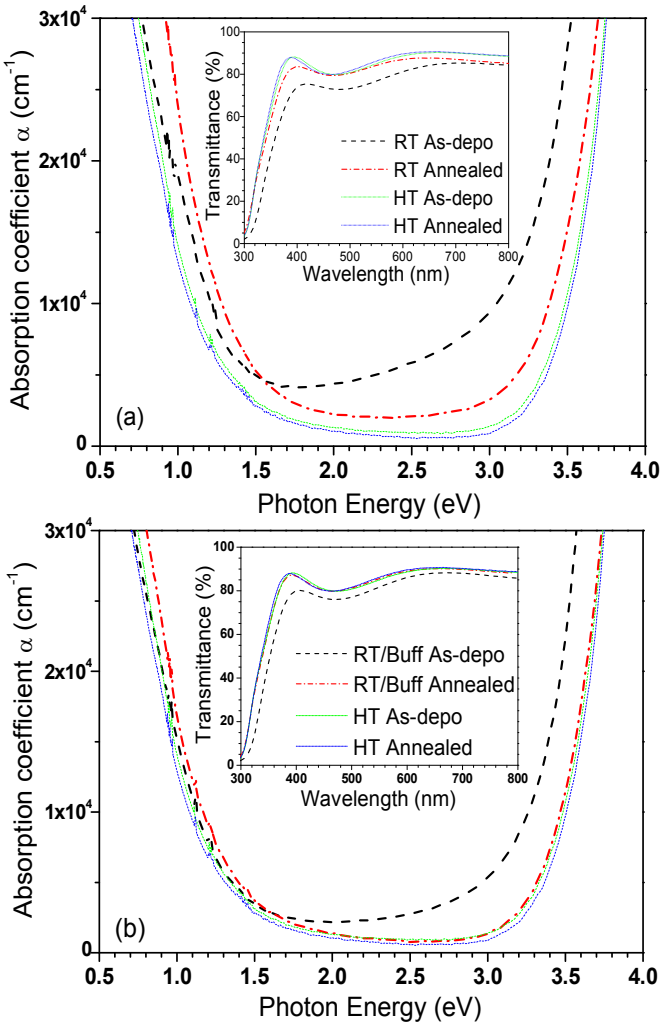

Fig. 4.5 Variations in the optical absorption spectra α of the GZO films, i.e., the RT film (a), and RT/Buffer film (b). Inset of figures shows the transmittance spectra. Those of HT film are also plotted as reference.

The inset of Fig. 4.5 shows the transmission spectra in the visible wavelength range. The transmittance of the as-deposited GZO films deposited at room temperature was lower compared to that of the HT. The average transmittances in the visible wavelength range from 380 nm to 750 nm were78.8 % and 82.8% for the RT and the RT/Buffer films, respectively, while that of the HT was 86.3%. The lower transmittance was due to absorption in the visible range. After the post-deposition annealing, the transmittance increased because of the decrease of the absorption band. The average transmittances after annealing were 84.3% and 86.2 % for the RT and RT/Buffer films, respectively.

Next, we address the effects of the buffer layer on the optical properties. The absorption of the RT/buffer film shown in Fig. 4.5 (b) appeared a little weaker compared to that of the RT film shown in Fig. 4.5 (a). The thickness of the RT film was approximately 200 nm, while the RT/Buffer film consisted of a160 nm thick top layer and a 40 nm thick buffer layer, with a total thickness of 200 nm. The lower absorption in the RT/Buffer film may be caused by the contribution of the buffer layer deposited at 200 °C. Thus, we considered that the lower transmittance and the higher absorption in the visible wavelength region for the as-deposited GZO films were independent of the self-buffer layer. At least, the control of microstructure had a minor effect on the optical absorption in the GZO films.

Such absorption in the visible wavelength region has been observed in GZO films [23] and has been considered as a contribution of the oxygen vacancy, V_O [23]. It was also predicted theoretically that the formation of V_O in GZO resulted in optical absorption in the visible wavelength region [24]. The absorption band also vanished by post deposition annealing [23]. V_O has been considered as native donors and a source of residual carriers for a long time. If that is the case, the carrier concentration will decrease after annealing. In the present study, the absorption band was significantly decreased by the post-deposition annealing, while the carrier concentration increased. Because V_O can form deep donor states according to first-

principle electronic structure calculations [25], it cannot be considered as a source of carriers itself. On the other hand, the increase of carrier concentration after annealing was likely due to the annealing out of acceptor type defects, such as V_{Zn} and/or O_i as discussed above. However, such defects cannot cause absorption in the visible wavelength region [24]. We can conclude that not only acceptor-type intrinsic defects, i.e., V_{Zn} and O_i, but also donor-type intrinsic defects, i.e., V_O, existed in the GZO films deposited at RT by RF magnetron sputtering. Such point defects can be annealed out during the deposition on heated substrates or by post-deposition annealing.

However, the situation of defects could be different between the films deposited on the heated substrate and films annealed after low temperature deposition. This was reflected in the higher carrier concentration and lower Hall mobility in the RT/buffer film even after annealing when compared to the HT film. The difference in the defects between high and low temperature depositions was also reflected in the different behavior observed in the lattice parameters.

4.3.4 Comparison between optical mobility and Hall mobility on the GZO films

An important measure for investigating the transport properties of TCO is the optical mobility, μ_{opt}, which can be deduced from an analysis of the reflection and transmission spectra or spectroscopic ellipsometry. The dielectric function modeling of the TCO including GZO, i.e.,$\varepsilon(E) = \varepsilon_1(E) - i\varepsilon_2(E)$, can be expressed as follows [26]:

$$\varepsilon(E) = \varepsilon_{TL}(E) + \varepsilon_D(E) \quad (2)$$

where $\varepsilon_{TL}(E)$ indicates the Tauc-Lorentz model representing the band gap transition, and $\varepsilon_D(E)$ indicates the Drude model representing the contribution of free carriers. The expression of the Drude model is given by [26]:

$$\varepsilon_D(E) = -\frac{A_D}{E^2 - i\Gamma_D E} = \left(-\frac{A_D}{E^2+\Gamma_D^2}\right) - i\left(\frac{A_D\Gamma_D}{E^2+\Gamma_D^2 E}\right) \quad (3)$$

Here, the amplitude, A_D, and the broadening parameter, Γ_D, are given by [14, 26]:

$$A_D = \frac{\hbar^2 e^2 N_{opt}}{m^* \varepsilon_0} \quad (4)$$

$$\Gamma_D = \frac{\hbar e}{m^* \mu_{opt}} \quad (5)$$

where $\hbar$, e, and m^* are the reduced plank constant, electron charge, broadening parameter, and effective mass, respectively. Using a simple four layer model, the value of Γ_D can be obtained by fitting the transmittance (T) and reflectance (R) spectra to the experimental result. The μ_{opt} can be estimated from the expression below:

$$\mu_{opt} = \frac{\hbar e}{\Gamma_D m^*} \quad (6)$$

Here, we employed the empirical formula of m^* for ZnO, i.e., m^*(ZnO) = (0.280 + 0.010×10^{-20} N_{Hall}) m_0, which was reported by Fujiwara *et al.* [26].

Fig. 4.6 (a) shows the μ_{opt} and μ_{Hall} for all samples studied here. The error bars of the μ_{opt} were estimated by inserting an error of 10 % for the m^*. As shown in Fig. 4.5 (a), the RT sample showed a higher absorption band in the visible wavelength region. We also estimated the μ_{opt} by including an additional Gaussian function, which represented the absorption band. The difference was approximately 0.2 cm^2/Vs, which was smaller than the error bars. The difference between the μ_{opt} and μ_{Hall} was obvious in the RT film regardless of the annealing procedure, while it was less or negligible between the RT/Buffer and HT films.

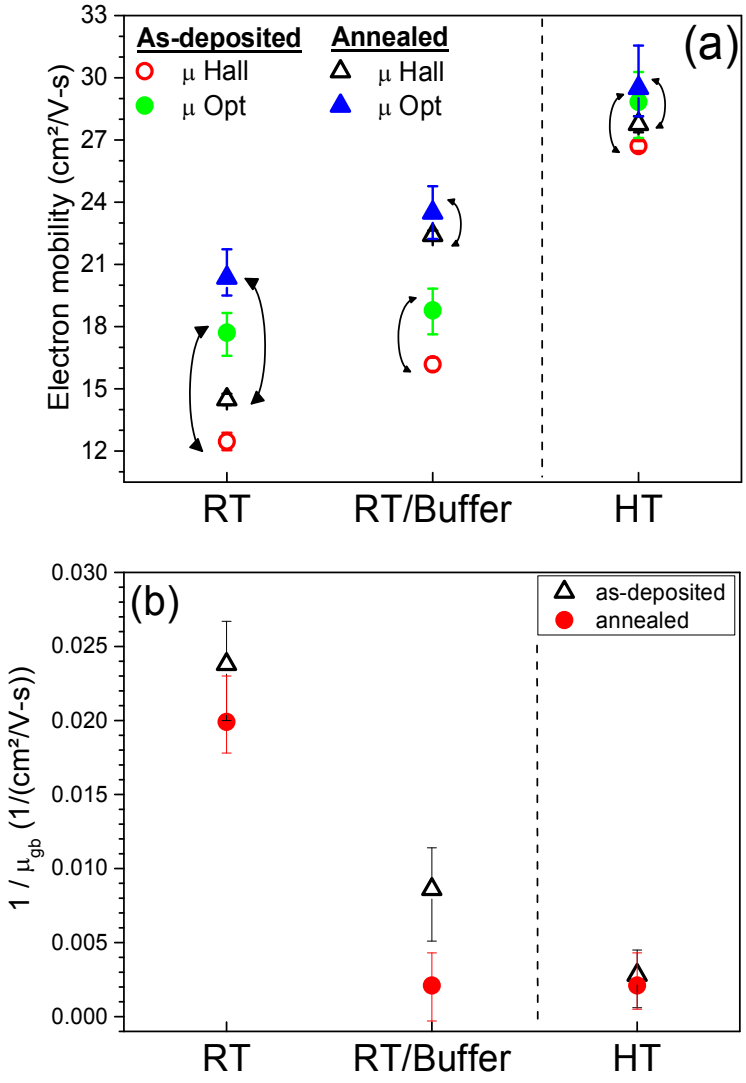

Fig. 4.6 Comparison between Hall and optical mobilities (a), and contributions of grain boundary scattering (b) of the GZO films, i.e., the RT, RT/Buffer, and HT films.

The difference between the μ_{opt} and μ_{Hall} has been reported in several studies [11, 14, 27, 28]. However, the cause of the difference is not so clear at the present. One explanation is the contribution of grain boundary scattering to the Hall mobility [11, 27]. Here, we tentatively attribute the difference to the grain boundary scattering. The μ_{opt} will not be affected by the grain boundary scattering [27]. Considering that the

optical mobility corresponds to the in-grain mobility, the Hall mobility can be expressed as follows [11, 28]:

$$\frac{1}{\mu_{hall}} = \frac{1}{\mu_{opt}} + \frac{1}{\mu_{gb}} \quad (2)$$

The contribution of grain boundary scattering, $\frac{1}{\mu_{gb}}$, is plotted in Fig. 4.6 (b). When $\frac{1}{\mu_{gb}} = 0$, the μ_{Hall} is equal to the μ_{opt}. This means that the contribution of grain boundary scattering to the Hall mobility is negligible. It can be clearly observed that $\frac{1}{\mu_{gb}}$strongly depended on the microstructural properties. The value of $\frac{1}{\mu_{gb}}$was higher in the GZO films deposited at RT without the buffer layer, and it was comparable before and after annealing. On the other hand, the value of $\frac{1}{\mu_{gb}}$ was nearly negligible in the RT/Buffer and HT films. This result suggested that the contribution of grain boundary scattering could be reduced by controlling the microstructure of the GZO films by using a self-buffer layer.

The relationship between the carrier concentration and the contribution of grain boundary scattering was reported by K. Ellmer *et al.* [9]. They reported that the Hall mobility was limited by grain barrier scattering for carrier concentrations of $n < \sim 5\text{x}10^{20}$ cm^{-3}, while the Hall mobility was limited by ionized impurity scattering for $n > \sim 5\text{x}10^{20}$ cm^{-3}. In this study, the carrier concentration of the RT film after annealing was 9 x10^{20} cm^{-3}, which was much higher than the boundary, but it still showed a clear difference between the μ_{opt} and μ_{Hall}. The contribution of the grain boundary scattering in polycrystalline GZO films has been theoretically studied by Yamamoto *et al*. [29] based on the classical grain size effect on the resistivity of thin films proposed by Mayadas and Shatzkes [30]. The contribution of grain boundary scattering has also been analyzed using the extended Seto model in AZO films, and it was suggested that the grain boundary scattering partially contributed to the Hall mobility even for high carrier concentrations of more than 10^{21} cm^{-3} [31].

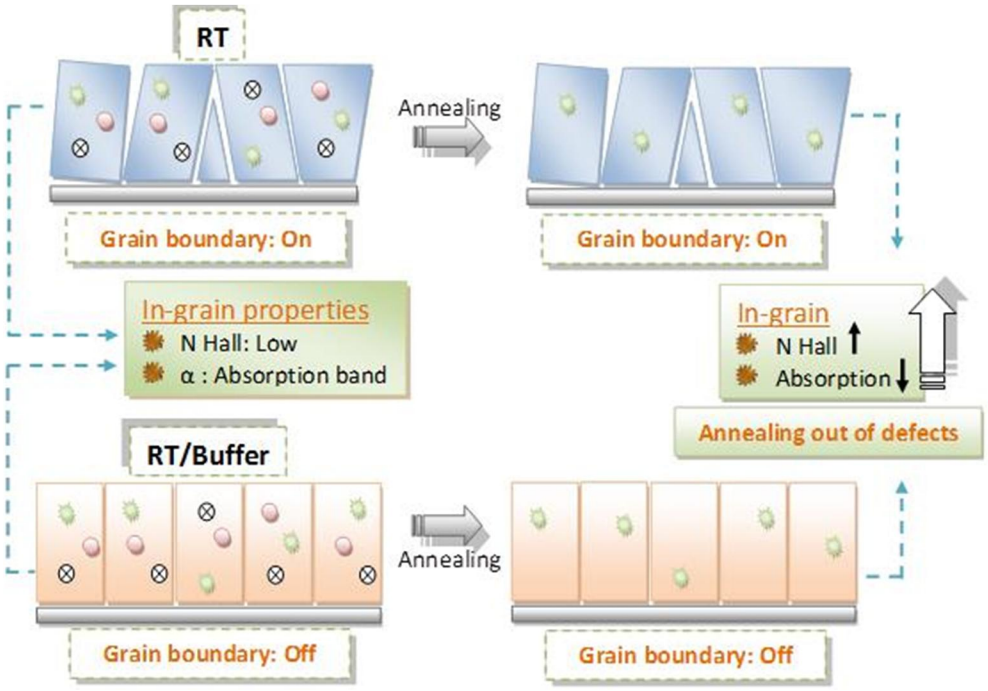

Fig. 4.7 Scheme of GZO film improvement by microstructural control and post deposition annealing.

Fig. 4.7 shows the schematic illustration related to the improvement of the GZO film properties deposited on the glass substrate at RT with and without the self-buffer layer. First, the GZO film deposited at RT without the self-buffer layer revealed that the contribution of grain boundary on the Hall mobility existed for both the as-deposited and annealed films. On the other hand, the GZO film with the self-buffer layer revealed that the grain boundary contribution was nearly negligible owing to the improvement of the *c*-axis orientation. Thus, the main effect of the improvement of the microstructure was reducing the contribution of the grain boundary on the Hall mobility. Second, the in-grain properties were strongly dependent on the deposition temperature. The reduced carrier concentration and the absorption band caused by defects in the films were clearly observed in the GZO films deposited at RT regardless of the microstructure. Such defects decreased after the post deposition annealing, resulting in the enhancement of carrier concentration, the increase of in-

grain mobility reflected in the μ_{opt}, and the reduction of the absorption band. Although the in-grain properties were improved by annealing, the Hall mobility was still limited at low values in the GZO film without the self-buffer layer because of poor *c*-axis orientation.

The results of this study suggest two aspects that should be considered in order to improve the properties of GZO films deposited at RT. One aspect to consider is the microstructure of the films, such as the *c*-axis orientation, in order to reduce the contribution of grain boundary. Another is the elimination of defects, which were commonly annealed out in the case of high temperature deposition. Such defects cannot be reduced only by controlling the microstructure.

4.4 Chapter Conclusions

We studied separately the influences of microstructure and defects on the properties of polycrystalline GZO films deposited at RT on glass substrates by RF magnetron sputtering by combining microstructural control and post deposition annealing. The *c*-axis orientation of GZO films was significantly improved by inserting a self-buffer layer deposited at a high temperature. The higher degree of *c*-axis orientation led to a reduction of the grain boundary contribution to Hall mobility. On the other hand, the in-grain properties were mainly improved by the post deposition annealing. The carrier concentration, in-grain carrier mobility, and transparency in the visible wavelength were improved owing to the elimination of defects in the GZO films. Although the in-grain properties were improved by annealing, the Hall mobility of films deposited on glass without the self-buffer layer was still limited by the contribution of grain boundary because of the poor *c*-axis orientation.

4.5 References

[1] T. Minami, Semicond. Sci. Technol. 20, S35 (2005).

[2] T. Minami, Thin Solid Films 516, 1314 (2008).

[3] T. Yamamoto, T. Yamada, A. Miyake, H. Makino, N. Yamamoto, J. Soc. Inf. Display 16, 713 (2008).

[4] T. Minami, T. Miyata, and J. Nomoto, IOP Conf. Ser.: Mater. Sci. and Eng. 34, 012001 (2012).

[5] N. Yamamoto, H. Makino, S. Osone, A. Ujihara, T. Ito, H. Hokari, T. Maruyama, T. Yamamoto, Thin Solid Films 520, 4131 (2012).

[6] J-K Sheu and Y.S. Lu, M-L. Lee, W.C. Lai, C.H. Kuo, C-J.Tun, Appl. Phys. Lett. 90, 263511 (2007).

[7] D. O. Demchenko, B. Earles, H. Y. Liu, V. Avrutin, N. Izyumskaya, U. Ozgur, and H. Morkoc, Phys. Rev. B 84, 075201 (2011).

[8] D. C. Look, K.D. Leedy, L. Vines and B,G. svensson, A. Zubiaga and F. Tuomisto, D.R. Doutt and L.J. Brillson, Phys. Rev. B 84, 115202 (2011).

[9] K. Ellmer and R. Mientus, Thin Solid Films 516, 4620 (2008).

[10] T. Terasako, H. Song, H. Makino, S. Shirakata, T. Yamamoto, Thin Solid Films 528, 19 (2013).

[11] T. Yamada, H. Makino, N. Yamamoto, and T. Yamamoto, J.Appl. Phys. 107, 123534 (2010).

[12] H. Y. Liu, V. Avrutin, N. Izyumskaya, U. Ozgur, A. B. Yankovich, A. V. Kvit, P.M. Voyles, and H. Morkoc, J. Appl. Phys. 111, 103713 (2012).

[13] S. Y. Lee, W. Lee, C. Nahm, J. Kim, S. Byun, T. Hwang, B. K. Lee, Y. I. Jang, S. Lee, H. M. Lee, and B. Park, Curr. Appl. Phys. 13, 775 (2013).

[14] H. Makino, N. Yamamoto, A. Miyake, T. Yamada, Y. Hirashima, H. Iwaoka, T. Itoh, H. Hokari, H. Aoki, T. Yamamoto, Thin Solid Films 518, 1386 (2009).

[15] H. Makino, H. Song, T. Yamamoto, Thin Solid Films 559, 78-82 (2014).

[16] D. C. Look, K. D. Leedy, D. B. Thomson, and B. Wang, J. Appl. Phys. 115, 012002 (2014).

[17] K. Elmer, A. Klein, B. Rech, Transparent Conductive Zinc Oxide, Basics and Applications in Thin Film Solar Cells, Springer, (2008).

[18] A. Bikowski, T. Welzel, K.Ellmer, Appl. Phys. Lett.102, 242106 (2013).

[19] D. L. Zhu, Q. Wang, S. Han, P.J. Cao, W.J. Liu, F. Jia, Y.X. Zeng, X.C. Ma, Y.M. Lu, Appl. Surf.Sci. 298, 208 (2014).

[20] I. Hamberg and C.G. Granqvist, K.F Berggren, B.E. Sernellius, and L. Engstrom, Phys. Rev. B 30, 3240 (1984).

[21] B. E. Sernelius, K. F. Berggren, Z. C. Jin, I. Hamberg and C. G. Granqvist, Phys. Rev. B 37, 10244 (1988).

[22] D. C. Look, T.C. Droubay, and S. A. Chambers, Appl. Phys. Lett. 101, 102101 (2012).

[23] H. Makino, T. Yamada, N. Yamamoto, T. Yamamoto, Thin Solid Films 519, 1521 (2010).

[24] M. H. Lee, Y. C. Peng, H. C. Wu, J. Alloys Compd. 616, 122 (2014).

[25] A. Janotti and C. G. Van de Walle, Appl. Phys. Lett. 87, 122102 (2005).

[26] H. Fujiwara and M. Kondo, Phys. Rev. B71, 075109 (2005).

[27] J. Steinhauser, S. Fay, N. Oliveira, E. Vallat-Sauvain, and C. Ballif, Appl. Phys. Lett.90, 142107 (2007).

[28] J. Nomoto, H. Makino, and T. Yamamoto, J. Appl. Phys. 117, 045304 (2015).

[29] T. Yamamoto, H. P. Song, H. Makino, Phys. Status Solidi C 10, 603 (2013).

[30] A. F. Mayadas and M. Shatzkes, Phys. Rev. B 13, 82 (1970).

[31] A. Bikowski and K.Ellmer, J. Appl. Phys.116, 143704 (2014).

5. Change of scattering mechanism and annealing out of defects with increasing substrate temperature

5.1 Introduction

Quite recently, considerable attention has been paid to the transparent conductive oxide (TCOs) as transparent electrode in optoelectronic devices. The most important TCOs for electrode applications are Sn-doped In_2O_3 (ITO), Al-doped ZnO (AZO) and Ga-doped ZnO (GZO). In the last few years, GZO is widely proposed as alternatives to ITO due to the similarity of practical low resistivity (~ 1-3 x 10^{-4} Ω.cm), the comparability of optical band gap (higher than 3.4 eV for GZO and ~ 3.7 eV for ITO), and the advantages of higher transmittance of GZO in the visible wavelength range compared to ITO [1-3]. In addition, from the view point of cost and availability, ITO is expensive compared to GZO due to scarcity of In and also toxic issue in the processing of materials.

Several deposition methods have been used to prepare ZnO based TCOs films such as vacuum arc plasma evaporation (VAPE), chemical vapor deposition (CVD), pulsed laser deposition (PLD) and magnetron sputtering (MSP) [4]. MSP system is one of the effective methods for film deposition due to the flexibility to fabricate on low temperature deposition, easily scalable to large deposition area and the fairly high quality films with good homogeneity. Currently, research on highly doped ZnO thin films are focused on transport properties to clarify scattering mechanism. Several publications have appeared in recent years focusing on the transport properties of highly doped ZnO [5-10].

The substrate temperature, *Ts,* is one of the most important parameters on thin films depositions. Commonly, films deposited at low *Ts* showed poor structural properties and low electrical properties indicated by high resistivity, low mobility, and low carrier concentration. The electrical properties of GZO films can be improved by increasing the *Ts* and the decreasing of resistivity was due to the increase both in Hall

mobility and carrier concentration [11, 12]. S.M. Park et al suggested that the improvement of carrier concentration presumably related to the increasing of Ga diffusion from grain boundaries and interstitial locations into the Zn cation sites [11]. A. Bikowski *et al* [13] demonstrated that the electrical properties strongly affected by the effect of ion bombardment during deposition. It has been known that on the sputtering deposition system, the electrical properties of AZO films decreased due to the effect of damage that was affected by negative oxygen ion bombardment during deposition by direct current (DC) and radio frequency (RF) MSP. The electrical resistivity of AZO films was improved by increasing *Ts*. This improvement has been explained on the fact that the defect which caused by ion bombardment could be annealed out by increasing *Ts* [13].

The relationship between structural properties and electrical properties has been reported on thickness dependence of GZO films from view point of grain boundary scattering [2]. It was also found that crystallite size and micro strain of AZO films increased as increasing *Ts* on the range from 30 °C to 400 °C deposited by RF-MSP on glass [14]. They suggested that surface diffusion of adsorbed species of sputtering was higher at higher *Ts* which lead to faster coalescence [14]. Recently, we examined the effects of structural properties on electrical and optical properties of GZO films deposited by RF-MSP at room temperature [15]. Highly oriented GZO films were realized by inserting a thin GZO self-buffer layer deposited at the higher *Ts*. It was found that the low carrier concentration and the optical absorption in visible wavelength region, which reduce transparency of the films, were appeared regardless of the structural properties, however, contribution of the grain boundary scattering was strongly depending on the structural properties [15].

Although the *Ts* has been commonly recognized as one of important parameters in deposition of ZnO based TCO films, the influences of defects and structural properties governed by the *Ts* on their electrical and optical properties has been not yet clearly understood. The discussion on this article will be focus on the change of

scattering mechanism controlled by the micro structural properties of films and annealing out of defects on GZO films deposited by RF-MSP changing the *Ts*.

The main part of this chapter has already been published in Journal of Applied Physics as listed in page of Publications. (*L. Nulhakim and H. Makino, Journal of Applied Physics 119, 235302 (2016)*)

5.2 Experimental

GZO transparent conducting films were prepared by RF-MSP using excitation frequencies of 13.56 MHz. The GZO films with thickness of approximately 200 nm was deposited on alkali-free glass substrate (Corning Eagle XG) with diameter of ~ 50 mm at substrate temperature of room temperature (RT), 100 °C, 125 °C, 150 °C, 175 °C, and 200 °C, respectively, using a ceramic target $ZnO:Ga_2O_3$ 5.7 wt %. The RF power was 100 W. The base pressure of the deposition chamber was kept below 5 x 10^{-5} Pa. The ultra high pure Argon gas (99.9999 %) with flow rate of 450 sccm was introduced during sputtering deposition. The pressure during deposition was ~ 0.3 Pa. The distance of substrate-target was fixed at 100 mm with target dimension of 76.2 mm in diameter and 6 mm in thickness.

We characterized the crystal structure by x-ray diffraction (XRD) using Cu $K\alpha$ radiation (Rigaku, ATX-G system). Transmittance (T) and reflectance (R) measurements have been performed with an angle of incidence for light at 5º by a spectrophotometer (Hitachi, U-4100) to determine the optical properties. The electrical properties of GZO films were characterized by Hall measurement system (Accent, HL5500PC) at room temperature using van der Pauw method to obtain resistivity, carrier concentration and Hall mobility.

5.3 Results and discussion

5.3.1 Structural properties

Firstly, we studied the structural properties of the GZO films by the XRD measurement. Fig. 5.1 (a) and (b) presents out of plane 2θ - ω scan profile of the GZO films. The Fig. 5.1 (b) shows the detail slow scan focus on 2θ on the range of 32 to 38 degree. Note that the diffraction intensity on the y-axis is represented in a logarithmic scale in order to see even week intensity peak. The XRD spectra depicts the films is polycrystalline with a wurtzite-type hexagonal structure without the existence of Ga oxide or Zn metal peaks. The films deposited at from RT to 150 ºC revealed poor *c*-axis orientation which indicated by weak peak intensity of 0002 and 0004 diffraction peaks and also the appearance of 10-11 peak. On the other hand, the GZO films show completely well aligned of *c*-axis orientation for the *Ts* higher than 175 ºC. The films with the *Ts* of 175 ºC and 200 ºC showed only two diffraction peaks of 0002 and 0004 without any additional peaks.

In order to characterize the degree of *c*-axis orientation, we evaluated the full width at half maximum (FWHM) of 0002 ω-rocking curve as a function of *Ts*. As shown in Fig. 5.2, the FWHM of 0002 ω-rocking curve steeply decreased with increasing the *Ts* up to 125 ºC, and then gradually decreased with increasing the *Ts*. This represents that the fluctuation of *c*-axis orientation between grains decreased with increasing the *Ts*.

Fig. 5.1 (c) showed the in-plane 2θχ-φ scan of 200 nm thick GZO films depending on the *Ts*. The patterns of GZO films deposited at *Ts* of 175 °C and 200 °C showed complete preferred *c*-axis orientation normal to glass substrates that indicated by no other peak instead of five main peaks, i.e., of $10\bar{1}0$, $11\bar{2}0$, $20\bar{2}0$, $21\bar{3}0$, and $30\bar{3}0$ which corresponding to lattice planes perpendicular to *c*-plane of wurtzite ZnO. Several peaks were observed for GZO films below the *Ts* of 150 °C. This observation was consistent with the results of out-of-plane measurements.

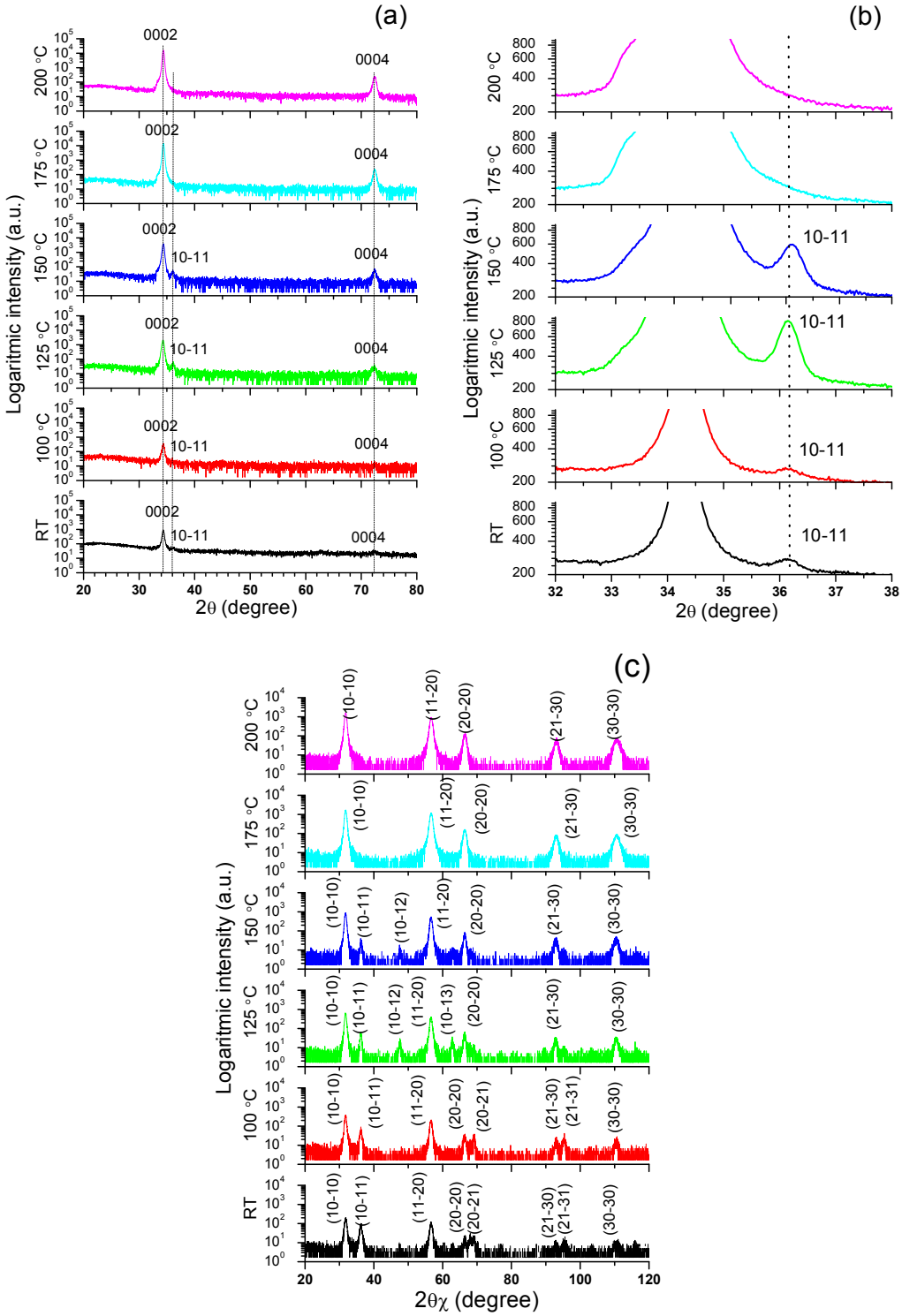

Fig. 5.1 Out of plane 2θ-ω scan in wide range (a), in narrow range (b) and in-plane 2θχ-φ scan (c) for GZO films deposited at varying *Ts* from RT to 200 °C.

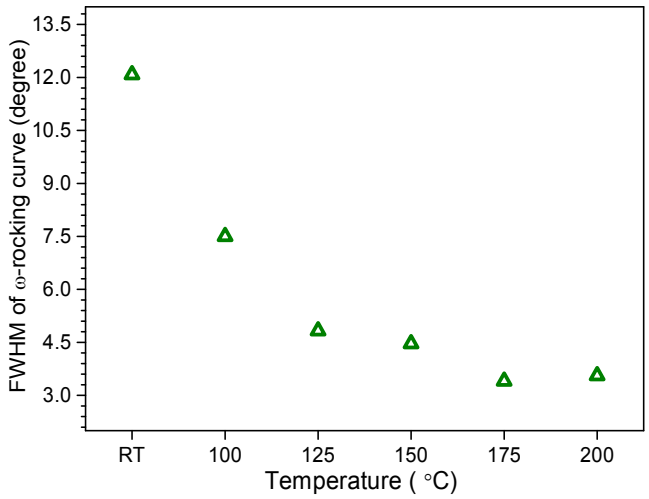

Fig. 5.2 FWHM of the 0002 peak ω-rocking curve in GZO films as a function of *Ts*.

It would be worth mentioning here that the appearance of 10-11 peak in the out-of-plane XRD profile cannot be explained by tilting of the *c*-axis in the *c*-axis orientation. The angle between (10-11) plane and *c*-plane is around 62 degrees. However, the value of FWHM of 0002 ω-rocking was about 4.5 degree at the *Ts* of 125 ºC. It was already sharp enough and not so largely different from that of 200 ºC with 3.5 degree. So the appearance of the 10-11 peak suggests existence of grains with the (10-11) plane parallel to the glass substrate surface. The existence of such oriented grains has been confirmed by ω-rocking curve measured for the 10-11 peak.

The *a*-axis lattice parameter, *a*, and the *c*-axis lattice parameter, *c*, were evaluated from the peak position of 10-10 diffraction peak measured by in-plane XRD, and that of 0002 peak measured by the out-of-plane XRD, respectively. As shown in Fig. 5.3 (a), the *a* is nearly independent on the Ts, while the *c* changed depending on the *Ts*. The c increases with increasing the *Ts* from RT to 125 ºC. It turns to decrease beyond the 125 ºC. The evolution of the lattice constant cannot be explain by residual strain in the films because the *a* was nearly constant with independent on the *Ts*. The change of the lattice parameter *c* possibly reflects defect states in the GZO films resulted in the change of the unit cell volume as shown in Fig. 5.3 (c).

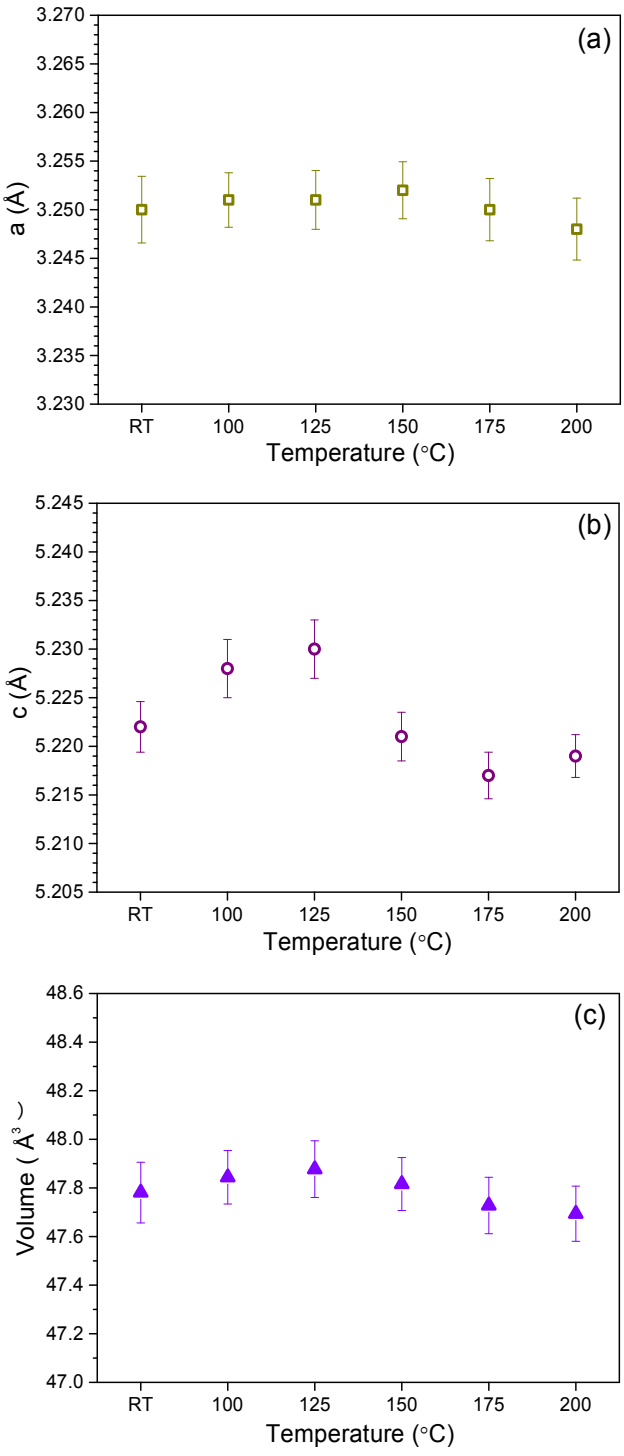

Fig. 5.3 (a) The *a*-axis lattice parameter, *a*, (b) *c*-axis lattice parameter, *c*, and (c) the volume of the unit cell, *V*, of GZO films as a function of *Ts*.

5.3.2 Electrical properties

Fig. 5.4 represents the variation in resistivity (a), carrier concentration (b) and Hall mobility (c) of GZO films as a function of *Ts*. The resistivity of GZO films decreased as increasing *Ts* with the lowest resistivity about 3.0 x 10^{-4} Ω.cm deposited at the *Ts* of 200 ºC, while the GZO film at RT showed the highest resistivity about 8.8 x 10^{-4} Ω.cm. The carrier concentration monotonously increased as increasing the *Ts*. The lowest carrier concentration at the *Ts* of RT was as low as 5.7 x 10^{20} cm^{-3} while the highest carrier concentration at the *Ts* of 200 ºC was as high as 7.7 x 10^{20} cm^{-3}. The increase of carrier concentration as increasing *Ts* can be considered as annealing out of defects during deposition as already pointed out by A. Bikowski *et al* [13]. The increase of carrier concentration could be tentatively attributed to the decrease of acceptor type defects such as interstitial oxygen O_i and/or zinc vacancy V_{Zn} [13, 16-17]. However, we found somewhat different behavior on the *Ts* dependence of the Hall mobility as shown in Fig. 5.4 (c). Although the carrier concentration monotonously increased with increasing the *Ts*, the Hall mobility gradually increased or less changed with increasing the *Ts* from RT to 150 ºC and jumped up beyond the 150 ºC. The Hall mobility rapidly improved from 16.1 cm^2/Vs at 150 ºC to 23.9 cm^2/Vs at 175 ºC. Then, the highest Hall mobility as high as 26.7 cm^2/Vs was achieved at the *Ts* of 200 °C. It should be mentioned that there was something improvements at the *Ts* between 150 ºC and 175 ºC. We will discuss it later in section 5.3.4.

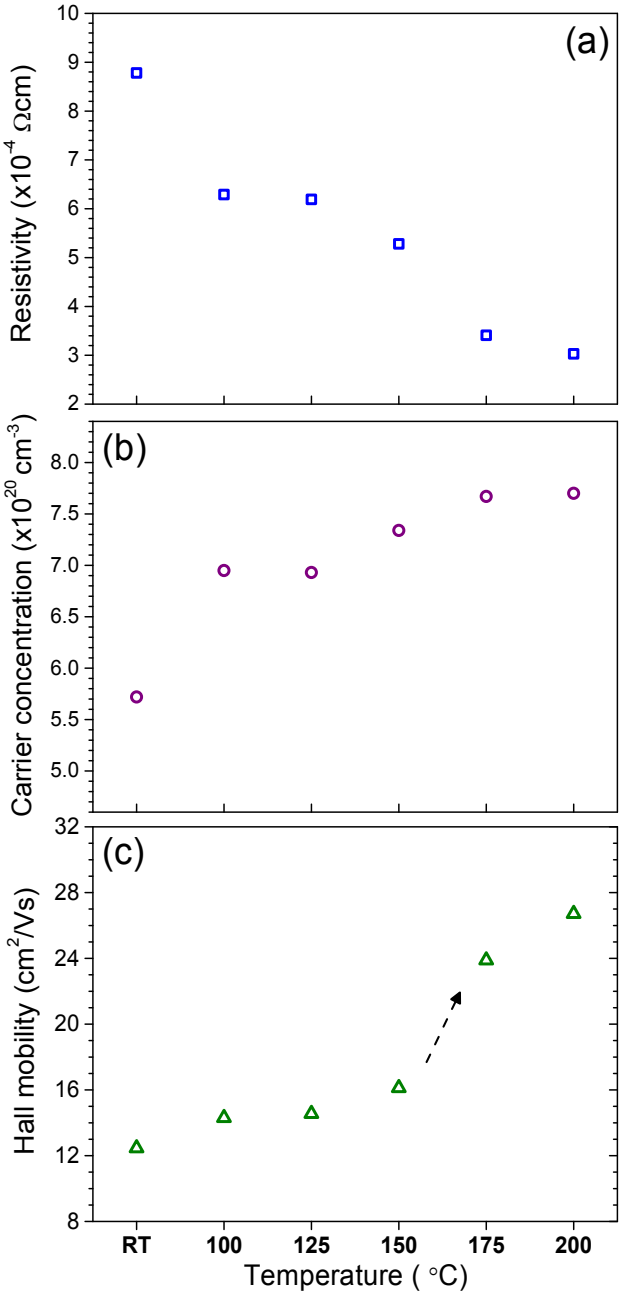

Fig. 5.4 Resistivity (a), carrier concentration (b), and Hall mobility (c) as a function of *Ts* for the GZO films.

5.3.3 Optical properties

We also characterized the optical properties of GZO film. Fig. 5.5 (a) shows the transmittance spectra in the wavelength range from 300 nm to 900 nm. We can see that the transmittance increased as increasing the *Ts*. The average transmittance (between 380 nm and 750 nm) for the *Ts* of 200 °C was about 86.7 %, while that for the *Ts* of RT was about 78.8 %. It was found that the lower transmittance of the low temperature deposition was caused by optical absorption.

Fig. 5.5 (b) shows the absorption spectra plotted as a function of photon energy. The absorption coefficient, α, was obtained by the equation as follow [18],

$$\alpha = \frac{1}{d} ln\left(\frac{100-R}{T}\right)$$

where *R* and *T* are the % of reflectance and % of transmittance, respectively. The *d* is the film thickness. The increase of absorption lower than about 1.5 eV toward low energy is corresponding to the free carrier absorption [19]. On the other hand, the absorption higher than 3 eV toward higher energy is so-called band gap absorption from the valence band to the Fermi level in the conduction band, which is depending on the carrier concentration. Inset of Fig. 5.5 (b) shows the *Ts* dependence of the optical band gap (*Eg*) calculated by the maximum of $\frac{d\alpha}{dE}$, where α and E are absorption coefficient and photon energy, respectively. The method for estimating the *Eg* on highly doped metal oxide followed the reference by I. Hamberg and B. E. Sernellius *et al* [20-22]. As shown in the inset of Fig. 5.5 (b), the *Eg* increased as increasing *Ts*. The tendency of the *Eg* can be understood by the Burstein-Moss (BM) shift. The change of *Eg* is consistent with the change of carrier concentration displayed in Fig. 5.4 (b).

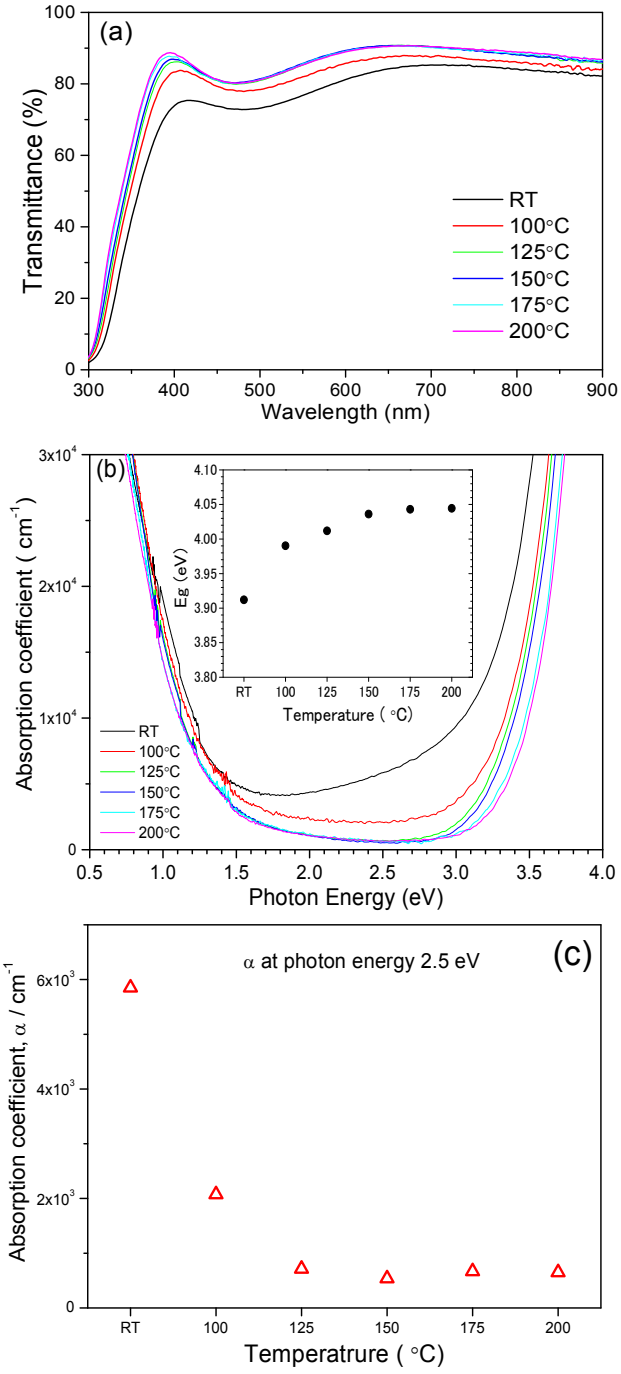

Fig. 5.5 Variation in transmittance T (a), absorption coefficient α (b), and α at photon energy of ~ 2.5 eV as a function of *Ts* (c). Inset of (b) shows optical band gap, E_g, estimated from the absorption spectra.

In addition to the above mentioned two contributions related to the free carriers, it can be also seen that the absorption band observed in the visible region, corresponding photon energy range between 2 eV and 2.8 eV, decreased as increasing the *Ts* as shown in Fig. 5.5 (b). The absorption coefficient at photon energy of about 2.5 eV or at approximately wavelength of 496 nm was plotted as a function of the *Ts* in Fig. 5.5 (c). The absorption band was nearly negligible in the GZO films of the *Ts* higher than 125 ºC. Such the absorption band has been reported in the GZO films deposited by the ion-plating with DC arc discharge [18]. The absorption band diminished with increasing the O_2 gas flow rate during the deposition. It was also decreased by post-deposition annealing [18]. Then the absorption band has been considered to be caused by oxygen vacancy, V_o, in the GZO films [23-26]. If that is the case, the decreasing of absorption in the visible region with increasing *Ts* could be related to the annealing out of defects such as V_o. The V_o has been considered to be a source of residual carriers in the metal oxides. However, the carrier concentration increased with increasing the *Ts*. This is contradicting to the present results. According to the theoretical prediction [27], the energy level of V_o in the band gap will be too deep to activate carriers. Another report on GZO and AZO thin films revealed that the improvement of n-type conductivity and optical transparency was affected by the presence of defect complex V_o - Zn_i [28].

5.3.4 Change of scattering mechanism

Firstly, let us discuss about change of scattering mechanism as increasing the *Ts*. Generally, the Hall mobility is limited by contribution of several scattering mechanisms based on the Matthiessen's rule [2, 29]. The in-grain mobility in heavily doped semiconductors is limited by ionized impurity scattering, optical phonon scattering, scattering by defects [29]. In the case of polycrystalline films, the Hall mobility can be also affected by grain boundary scattering even very high doping regime [30]. In order to evaluate contribution of the grain boundary scattering, we employed optical mobility obtained from optical measurements. Although there is still remaining discussion on the origin of the difference between the optical mobility

and the Hall mobility, the optical mobility shows close relationship with the in-grain mobility [2, 5, 29, 31-32]. The dielectric function of GZO films can be expressed by using the Drude model and the Tauc Lorentz (TL) oscillator model as follow:

$$\varepsilon(E) = \varepsilon_{TL}(E) + \varepsilon_D(E)$$

The TL model was used to describe the spectral data of the *Eg* corresponding to transition from the valence band to the conduction band. For the contribution of free carriers, the Drude model can be expressed as follow:

$$\varepsilon_D(E) = -\frac{A_D}{E^2 - i\Gamma_D E} = \left(-\frac{A_D}{E^2+\Gamma_D^2}\right) - i\left(\frac{A_D\Gamma_D}{E^2+\Gamma_D^2 E}\right)$$

where amplitude, A_D, and broadening parameter, Γ_D, are given by [5, 29]

$$A_D = \frac{\hbar^2 e^2 N_{opt}}{m^* \varepsilon_0}$$

and

$$\Gamma_D = \frac{\hbar e}{m^* \mu_{opt}}$$

Here, $\hbar$, e, and m^* are reduced plank constant, electron charge, and effective mass of carrier, respectively. Based on the above equations, the optical mobility can be estimated from the expression:

$$\mu_{opt} = \frac{\hbar e}{\Gamma_D m^*}$$

In this study, the m^* estimated from the previously reported expression by m^*(ZnO) = (0.280 + 0.010×10^{-20} N_{Hall}) m_0[29] were used. We deduced optical mobility by least square fitting to the transmission and reflection spectra using the A_D and the Γ_D as fitting parameters.

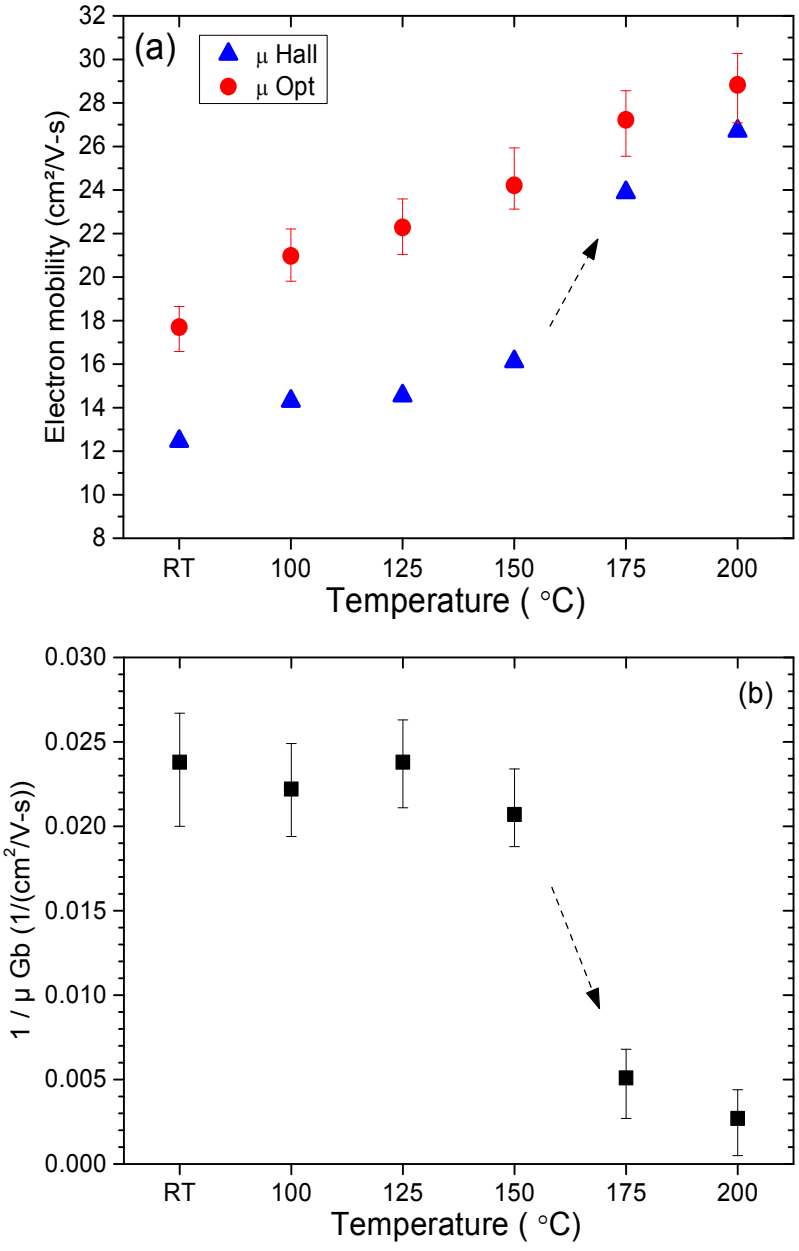

Fig. 5.6 Comparison of the Hall and optical mobility of GZO films (a) and the contribution of grain boundary scattering (b) as a function of *Ts*.

Fig. 5.6 (a) shows comparison between the Hall mobility and the optical mobility as a function of *Ts*. It can be seen that the optical mobility monotonously increased with increasing the *Ts* like as the case of carrier concentration as shown in Fig. 5.4 (b). The tendency is different from the Hall mobility. In the case of polycrystalline films, the Hall mobility, μ_{Hall}, can be expressed as follows including the in-grain mobility, μ_{ig}, and the mobility at grain boundary, μ_{gb}, as the contribution of grain boundary scattering:

$$\frac{1}{\mu_{Hall}} = \frac{1}{\mu_{ig}} + \frac{1}{\mu_{gb}}$$

When the contribution of grain boundary, $1/\mu_{gb}$, is negligible, the μ_{Hall} is identical to the μ_{ig}. Considering that the optical mobility is corresponding to the in-grain mobility, we evaluated the contribution of grain boundary. The contribution of grain boundary, $1/\mu_{gb}$, is plotted as a function of the *Ts* in Fig. 5.6 (b). It was revealed that the grain boundary contribution nearly stable up to 150 °C then drastically decreased from 150 °C to 175 °C. Eventually, the contribution of grain boundary on the Hall mobility nearly neglected at 200 °C.

The evolution of contribution of grain boundary reminds us the characteristics of the structural properties. We observed the 10-11 diffraction peak in the out-of-plane XRD profile up to 150 °C, then the peak disappeared higher than 175 °C. Thus, there is close relationship between the structural properties and the Hall mobility. The Hall mobility was reduced by the contribution of grain boundary, and the contribution of grain boundary was suppressed concomitant with the disappearance of the 10-11 peak. In other word, the existence of 10-11 oriented grains strongly decreases the Hall mobility through grain boundary scattering. The films with *Ts* higher than 175 °C showed perfectly *c*-axis orientation without any other orientation like as (10-11) lattice plane and hence showed nearly no influence of grain boundary contribution.

Details on the mechanisms how the existence of the other oriented grains influence the Hall mobility is not clear at the present.

5.3.5 Annealing out of defects

Next, let us discuss about annealing out of the defects, which were most probably caused by the ion bombardment during the RF-MSP deposition. We observed the optical absorption band in visible wavelength region in the GZO films deposited at the RT. We tentatively attributed the defects to the V_O. The absorption band decreased with increasing the *Ts*, and diminished at the *Ts* of 125 °C. It means that the defects related to the absorption band can be suppressed by a little increase of the *Ts*. In other word, such the defect was not so stable in the GZO films at such the low temperature deposition.

As shown in Fig. 5.4 (b), the carrier concentration gradually increased with increasing the *Ts*. The increase of carrier concentration can be explained by the annealing out of the acceptor type defects, such as O_i and/or V_{Zn}, with increasing the *Ts*. Since the optical mobility reflect scattering of carriers in grain bulk, the change of optical mobility in Fig. 5.6 (a) can be also explained by the annealing out of acceptor type defects such as O_i and/or V_{Zn} created in the grain bulk. Bikowski *et al* reported that O_i is the most probable candidate for the defects in AZO films caused by the ion bombardment during deposition by MSP based on the decrease of the *c*-axis lattice constant [13]. In the present study, the *c* increased with increasing the *Ts* up to 125 °C, then turned to decrease with increasing the *Ts*. This can be explained by contribution of different kinds of defects. From RT to 125 °C, the V_O decreased with increasing the *Ts*. The decrease of V_O contributed to the increase of *c*-axis lattice parameters and the volume of unit cell up to 125 °C. While beyond the 125 °C, the decrease of O_i with increasing the *Ts* started to dominate the change of the lattice parameters, and then resulted in the decrease of the *c* as shown in Fig. 5.3 (b).

The improvement of crystalline quality or the improvement of *c*-axis orientation might be also related to the decreasing of intrinsic defects leading to the increase of carrier concentration and Hall mobility [33]. However, according to our preceding study [15], the control of structural properties itself, that is the improvement of *c*-axis orientation, was not enough to decrease the defects observed in this study. This aspect suggests importance of reducing the formation of such defects caused by the ion bombardment in order to improve electrical and optical properties of ZnO based TCOs deposited at RT. Additionally, it is also important to control structural properties, that is to say, good *c*-axis orientation without other oriented grains like as grains with (10-11) plane parallel to glass surface, in order to obtain higher Hall mobility without contribution of grain boundary scattering that significantly decrease the Hall mobility.

5.4 Chapter Conclusions

In conclusion, to further understanding about the change of scattering mechanism and annealing out of defects on GZO films, we studied the GZO films deposition by RF-MSP method with varying the Ts from RT to 200 °C. We separately discussed that there are two effects of high temperature deposition, the first is annealing out of point defects and the other is improvement of c-axis orientation. The observations showed that the defects caused by ion bombardment during deposition could be eliminated by increasing Ts. The reduction of these defects leads to the improvement of carrier concentration, optical mobility, and transparency. It was also found that the appearance of 10-11 peak was closely related to the contribution of grain boundary scattering which significantly decrease the hall mobility. The grain boundary contribution was nearly neglected at Ts higher than 175 °C, which indicated by completely well aligned c-axis orientation without the appearance of 10-11 peak. Clearly, further research will be required to clarify detailed scattering mechanisms governed by the existences of 10-11 peak observed at rather lower Ts below 150 °C.

5.5 References

[1] T. Minami, Semicond. Sci. Technol. 20, S35 (2005).

[2] T. Yamada, H. Makino, N. Yamamoto, and T. Yamamoto, J. Appl. Phys. 107, 123534 (2010).

[3] T. Yamamoto, T. Yamada, A. Miyake, H. Makino, N. Yamamoto, J. Soc. Inf. Disp. 16, 713 (2008).

[4] K. Elmer, A. Klein, and B. Rech, *Transparent Conductive Zinc Oxide, Basics and Applications in Thin Film Solar Cells* (Springer - Verlag Berlin Heidelberg, 2008) p. 9.

[5] H. Makino, N. Yamamoto, A. Miyake, T. Yamada, Y. Hirashima, H. Iwaoka, T. Itoh, H. Hokari, H. Aoki, and T. Yamamoto, Thin Solid Films 518, 1386 (2009).

[6] H. Makino, H. Song, and T. Yamamoto, Thin Solid Films 559, 78 (2014).

[7] T. Terasako, H. Song, H. Makino, S. Shirakata, and T. Yamamoto, Thin Solid Films 528, 19 (2013).

[8] D. O. Demchenko, B. Earles, H. Y. Liu, V. Avrutin, N. Izyumskaya, U. Ozgur, and H. Morkoc, Phys. Rev. B 84, 075201 (2011).

[9] H. Y. Liu, V. Avrutin, N. Izyumskaya, U. Ozgur, A. B. Yankovich, A. V. Kvit, P.M. Voyles, and H. Morkoc, J. Appl. Phys. 111, 103713 (2012).

[10] D. C. Look, K. D. Leedy, D. B. Thomson, and B. Wang, J. Appl. Phys. 115, 012002 (2014).

[11] S.M. Park, T. Ikegami, and K. Ebihara, Thin Solids Films 513, 90 (2006).

[12] M. Miyazaki, K. Sato, A. Mitsui, and H. Nishimura, J. Non-Cryst. Solids 218, 323-328 (1997).

[13] A. Bikowski, T. Welzel, and K. Ellmer, Appl. Phys. Lett. 102, 242106 (2013).

[14] C. C. Singh, T. A. Patel, and E. Panda, J. Appl. Phys. 117, 245312 (2015).

[15] L. Nulhakim, and H. Makino, Thin Solid Films 615, 158-164 (2016).

[16] D. C. Look, K. D. Leedy, L. Vines, B. G. Svensson, A. Zubiaga, F. Tuomisto, D. R. Doutt, and L.J. Brillson, Phys. Rev. B 84, 115202 (2011).

[17] D. C. Look, T. C. Droubay, and S. A. Chambers, Appl. Phys. Lett. 101, 102101 (2012).

[18] H. Makino, T. Yamada, N. Yamamoto, and T. Yamamoto, Thin Solid Films 519, 1521-1524 (2010).

[19] H. Peelaers, E. Kioupakis, and C. G. Van de Walle, Appl. Phys. Lett. 100, 011914 (2012).

[20] I. Hamberg, C. G. Granqvist, K. F. Berggren, B. E. Sernellius, and L. Engstrom, Phys. Rev. B 30, 3240 (1984).

[21] B. E. Sernelius, K. F. Berggren, Z. C. Jin, I. Hamberg and C. G. Granqvist, Phys. Rev. B 37, 10 244 (1988).

[22] I. Hamberg and C.G. Granqvist, J. Appl. Phys. 60, 11 (1986).

[23] K. Vanheusden, C. H. Seager, W. L. Warren, D. R. Tallant, and J. A. Voigt, Appl. Phys. Lett. 68, 403 (1996).

[24] K. Vanheusden, W. L. Warren, D. H. Seager, D. R. Tallant, J. A. Voigt, and B. E. Gnade, J. Appl. Phys. 79, 7983 (1996).

[25] H. S. Kang, J. S. Kang, J. W. Kim, and S. Y. Lee, J. Appl. Phys. 95, 1246 (2004).

[26] K. Sakai, T. Kakeno and T. Ikari, S. Shirakata, T. Sakemi, K. Awai, and T. Yamamoto, J. Appl. Phys. 99, 043508 (2006).

[27] A. Janotti and C. G. Van de Walle, Appl. Phys. Lett. 87, 122102 (2005).

[28] N. K. Temizer, S. Nori, and J. Narayan, J. Appl. Phys. 115, 023705 (2014).

[29] H. Fujiwara and M. Kondo, Phys. Rev. B 71, 075109 (2005).

[30] A. Bikowski and K. Ellmer, J. Appl. Phys. 116, 143704 (2014).

[31] J. Nomoto, H. Makino, and T. Yamamoto, J. Appl. Phys. 117, 045304 (2015).

[32] T. Yamamoto, H. Song, and H. Makino, Phys. Status Solidi C 10, 603-606 (2013).

[33] T. Yamada, A. Miyake, S. Kishimoto, H. Makino, N. Yamamoto, and T. Yamamoto, Appl. Phys. Lett. 91, 051915 (2007).

6. Effect of polarity inversion on the electrical properties

6.1 Introduction

Zinc oxide based transparent conductive films like as Ga-doped ZnO (GZO) and Al-doped ZnO (AZO) have been gaining importance in recent years as a material class of transparent electrodes for optoelectronic applications, e.g., flat panel displays [1], light emitting diode [2], and thin film photovoltaic [3, 4], etc. Researchers have extensively studied the doped ZnO based on several criteria, i.e., the Zn material is abundance in nature, low cost in processing, and non-toxicity. The RF magnetron sputtering (RF-MSP) is one of the effective methods to prepare high quality ZnO films, e.g., dense film, good homogeneity and uniformity of films and relatively simple to control film thickness [5, 6].

For several years great effort has been devoted to the study of thickness dependence of heavily doped ZnO either thin or thick films on the range from a few nm to higher than 500 nm [7-13]. It has been reported that electrical properties strongly depends on films thickness. Yamada *et al* [7] studied the low resistivity GZO thin films of thickness less than 100 nm by ion plating method and discussed the electrical properties in relation to their structural properties. Itagaki *et al* [14] improved resistivity of 20 nm thick AZO films utilizing a ZnO buffer layer fabricated by solid-phase crystallization, and it was argued that the improvement was owing to the improvement of structural properties [14]. Look *et al* mentioned that the lower mobility of very thin films was caused by the poor interface layer with high density defects formed at interface of lattice mismatched substrates [10-11]. Bikowski *et al* recently reported that the resistivity of AZO films deposited by RF-MSP was strongly influenced by inhomogeneous distribution of Al dopants [13].

In this chapter, we propose influence of crystallographic polarity on electrical properties of GZO films deposited by RF-MSP as one of causes for the strong thickness dependence below 100 nm. We achieved a 30 nm thick GZO thin film with

resistivity of 2.62 × 10^{-4} Ωcm, Hall mobility of 26.9 cm^2/Vs, and carrier concentration of 8.87 × 10^{20} cm^{-3} using Zn-polar ZnO template on glass substrate.

The main part of this chapter has already been published in Physica Status Solidi-Rapid Research Letter as listed in page of Publications. (*L. Nulhakim and H. Makino, Phys. Status Solidi-Rapid Res. Lett. 10, 535–539 (2016)*)

6.2 Experimental

Polycrystalline GZO films were prepared by RF-MSP (frequencies 13.56 MHz) using a ceramic target ZnO:Ga_2O_3 5.7 wt. % (AGC Ceramic) at a substrate temperature of 200 °C. The ultra-high purity Argon gas (99.9999 %) was introduced at a flow rate of 450 sccm. The deposition rate was 10.7 nm/minutes under a RF power of 100 W. GZO films with several thicknesses in the range of 10 nm to 500 nm were deposited on glass substrates (Corning, Eagle XG). The film thickness was controlled by deposition time and confirmed by a surface profiler (KLA Tencor, Alpha-Step IQ). The electrical properties were characterized by room temperature Hall measurement (Accent, HL5500PC) using van der Pauw method. The crystal structure was characterized by x-ray diffraction (XRD) using Cu Kα radiation (Rigaku, ATX-G). The valence band spectra were measured by a custom made laboratory high energy x-ray photoelectron spectroscopy (HE-XPS) system equipped with a Cr Kα x-ray source with photon energy of 5414.87 eV (ULVAC-PHI) and a wide acceptance angle electron analyzer (VG Scienta EW4000).

6.3 Results and discussion

Fig. 6.1 showed the electrical properties of GZO films deposited on glass substrates as a function of films thickness. As shown in Fig. 6.1 (a), resistivity rapidly decreased with increasing the films thickness below 100 nm and then it was nearly stable at higher than 100 nm. The resistivity of 30 nm thick GZO thin films was ~ 1.4 × 10^{-3} Ωcm, while those of thicker than 100 nm were ~ 2.9 × 10^{-4} Ωcm. The carrier

concentration rapidly increased with thickness below 100 nm and then nearly identical up to 500 nm as shown in Fig. 6.1 (b). The Hall mobility also rapidly increased with increasing thickness between 30 nm and 100 nm, and then gradually increased up to 500 nm. These observations were basically similar to previously reported thickness dependence of GZO films deposited by the ion-plating [8, 9].

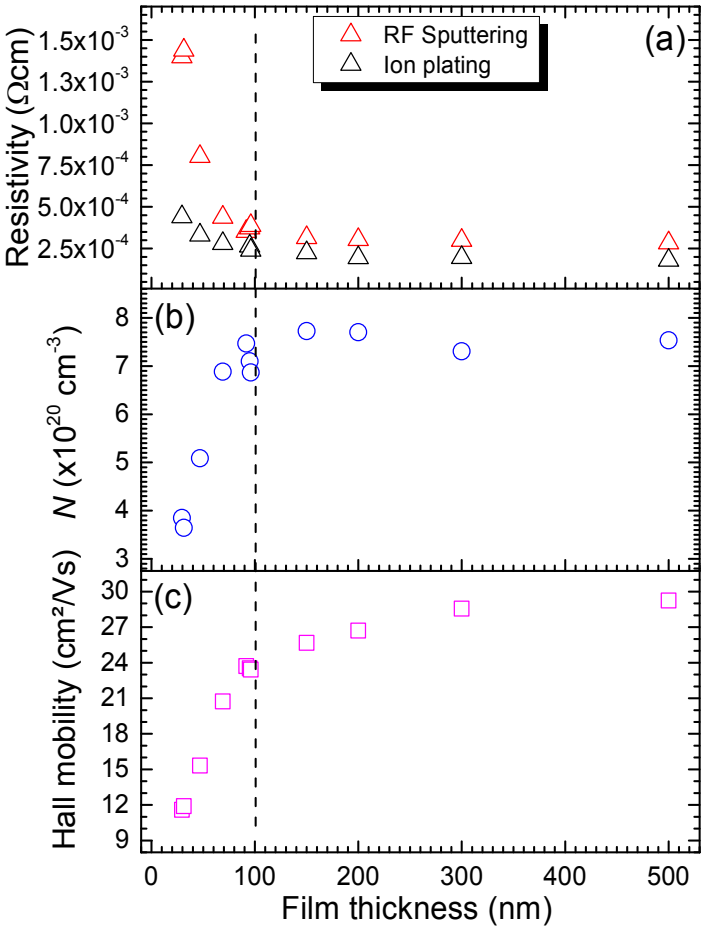

Fig. 6.1 Variation in (a) resistivity ρ, (b) carrier concentration N, and (c) Hall mobility μ of GZO films deposited on glass substrates at 200 °C as a function of film thickness.

Fig 6.2 (a) and (b) show the out-of-plane and in-plane XRD patterns of the GZO films deposited on glass substrates. We observed 0002 and 0004 diffraction peaks for

all the GZO films in the out-of-plane XRD. On the other hand, we observed five diffraction peaks of $10\bar{1}0$, $11\bar{2}0$, $20\bar{2}0$, $21\bar{3}0$, and $30\bar{3}0$ that corresponding to lattice planes perpendicular to *c*-plane of ZnO in the in-plane XRD. These results suggest that the GZO films show strong preferred orientation in *c*-axis normal to glass substrates.

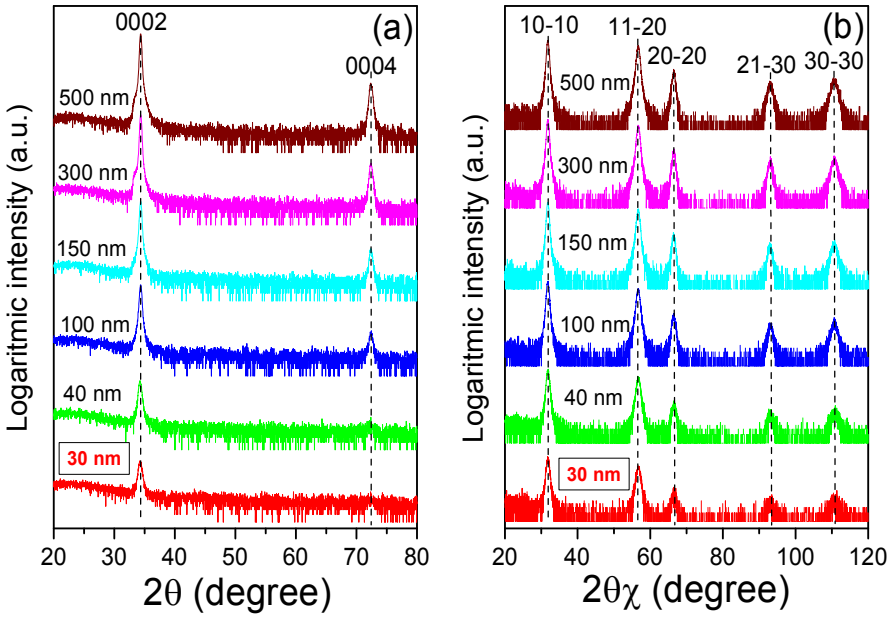

Fig. 6.2 Out-of-plane 2θ-ω scan (a), grazing incidence in-plane 2θχ-φ scan (b) of GZO films deposited on bare glass substrates as a function of film thickness.

We also found that the structural properties of GZO films like as degree of *c*-axis orientation and grain size were nearly comparable between the RF-MSP (this study) and the ion plating [8, 9]. We measured ω-rocking curve for 0002 diffractions, and characterized the full width at half maximum (FWHM). The grain size of GZO films was evaluated from the in-plane XRD using the Williamson-Hall plot analysis. Fig.6.3 shows the full width at half maximum (FWHM) of 0002 ω rocking curve and grain size of GZO films deposited by RF-MSP as a function of films thickness. The data of GZO films deposited by ion plating from references [8, 9] were also plotted

for comparison. The FWHM of 0002 ω rocking curve and the grain size for GZO film deposited by RF-MSP were practically comparable to those deposited by the ion-plating method [8, 9].

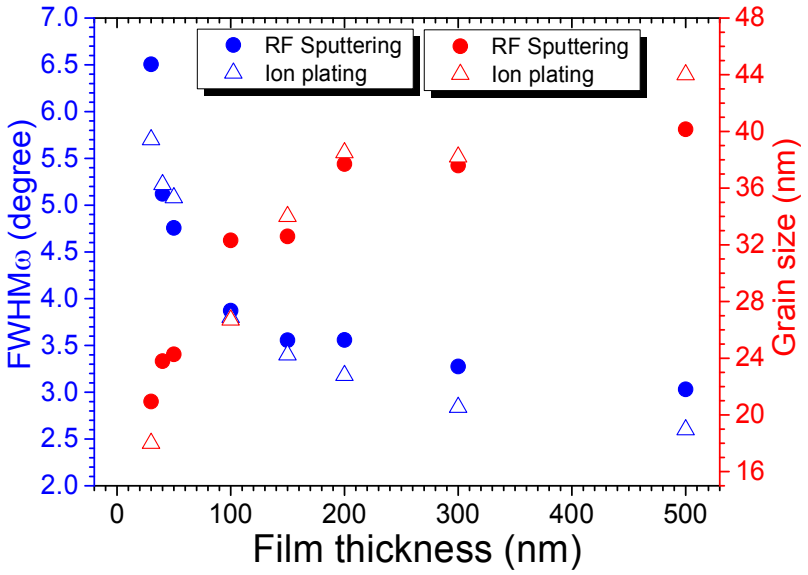

Fig. 6.3 FWHM of 0002 ω-rocking curve and grain size of GZO films deposited on glass substrates at 200 °C as a function of film thickness. The data of ion-plating from references [8, 9].

Fig. 6.4 shows the lattice parameters of GZO films as a function of film thickness. It can be seen that *a*-axis lattice parameter slightly increased up to the thickness of 100 nm then saturated until 500 nm. Whereas, *c*-axis lattice parameter drastically decreased up to thickness of 100 nm then nearly saturated until 500 nm. The volume of unit cell was entirely identical over the range of film thickness. These tendencies can be explained by relaxation of the compressive residual strain with increasing the film thickness up to 100 nm. And such behavior was also observed the thickness dependence of GZO deposited by the ion-plating [8, 9].

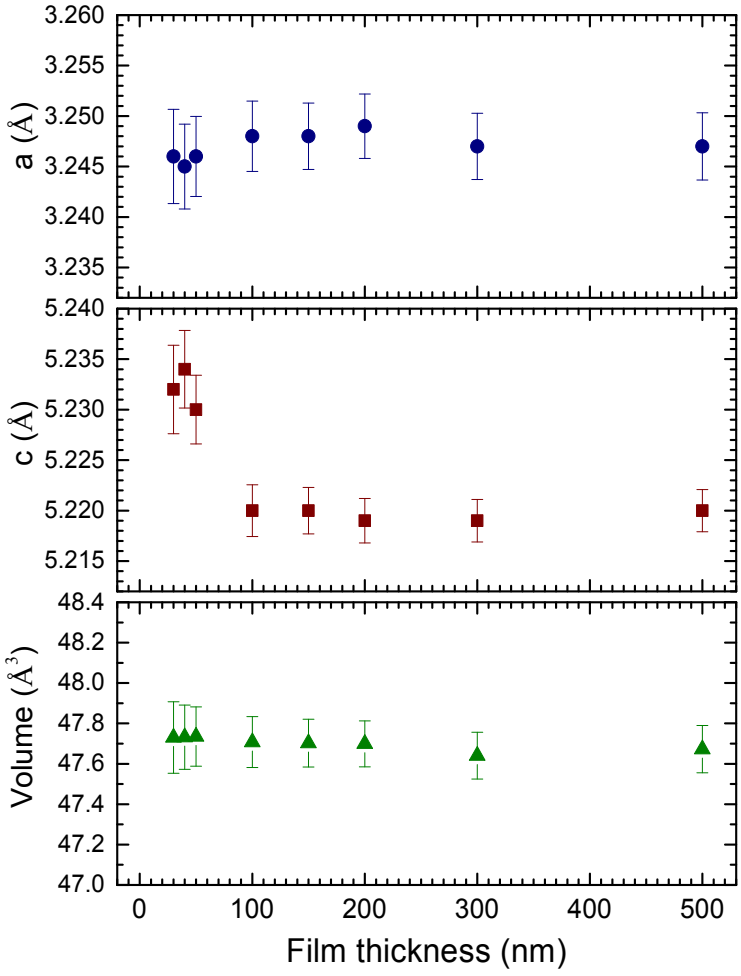

Fig. 6.4 The a-axis and c-axis lattice parameters and volume of unit cell of GZO films deposited on bare glass substrates as a function of film thickness.

Yamada et al. suggested that the change of grain structures depending on the thickness would lead to formation of some defects resulting in the degradation of electrical properties below 100 nm [8]. In the case of RF-MSP, we could not observe any obvious differences in structural properties of GZO films from the ion-plating deposition [8]. However, the change of the electrical properties below 100 nm was more abrupt in the present case resulting in much higher resistivity of the very thin films compared to that deposited by the ion-plating [8]. Accordingly, we needed to

consider additional influences on their electrical properties, and we noticed the influence of polarity.

The spectral shape of the valence band (VB) measured by XPS has been known as one of finger prints of crystallographic polarity in wurtzite type semiconductors [15, 16]. Fig. 6.5 shows the VB spectra of Zn-polar (0001) face and O-polar $(000\bar{1})$ face of a single crystalline ZnO measured by HE-XPS as reference. The Zn-polar face can be indicated by the appearance of sub peak at binding energy of ~ 5 eV.

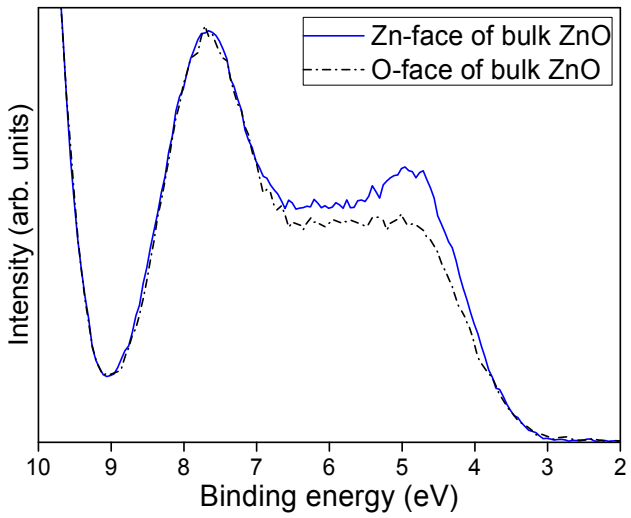

Fig. 6.5 Valence band spectra for Zn-polar and O-polar faces of single crystalline ZnO.

Fig. 6.6 shows the VB spectra for the GZO films with various thicknesses of 10, 30, 40, 100, 150, 300, and 500 nm, respectively. As shown in Fig. 6.6, the spectra of the thinner films (10 and 30 nm) showed more likely to O-polar face, and then a sub peak at ~ 5 eV appeared and increased with increasing thickness from 30 to 100 nm. The films higher than 100 nm showed the Zn-polar face because the sub peak at ~ 5 eV was more obvious. This observation suggests polarity inversion from O-polar to Zn-polar with increasing film thickness.

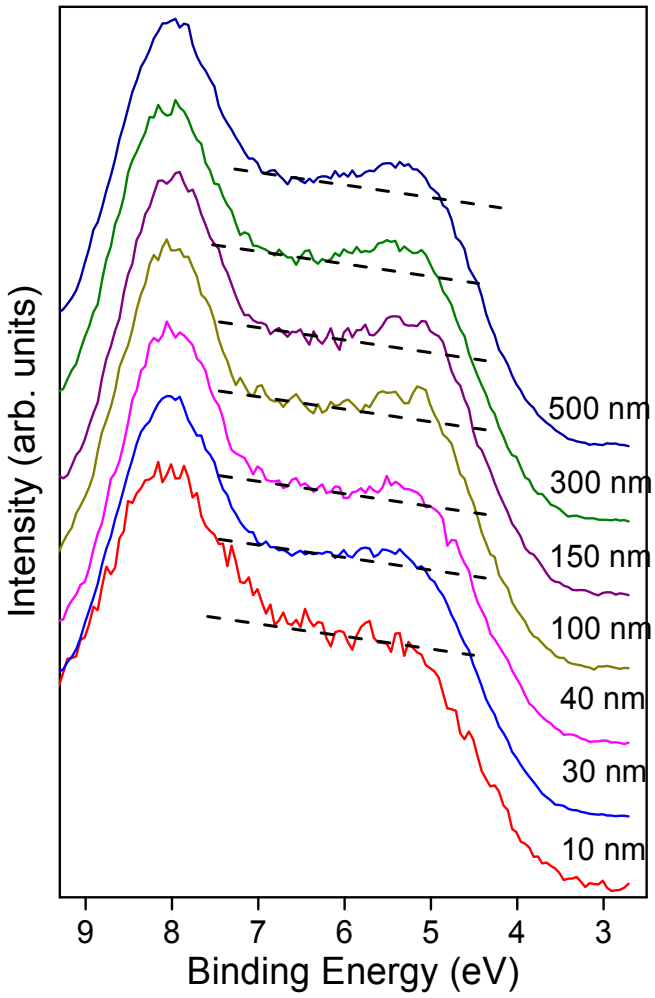

Fig. 6.6 Valence band spectra for GZO films of different thicknesses deposited on bare glass substrates.

Such the flipping of polarity during growth of doped ZnO films have been reported and discussed based on film growth mechanism [17-19]. Ogino *et al* reported that the GZO tend to be nucleation of grains with Zn-polar, and resulted in the growth of Zn-polar films in heavily doped GZO while flipped to O-polar films in lightly doped GZO by abnormal grain growth [18]. Abduev *et al* proposed the GZO shows nucleation of grains with both Zn-polar and O-polar grains, and then Zn-polar grains dominate in heavily doped GZO while O-polar grains dominate in lightly doped GZO

after reached to film growth stage [19]. In the present study, we deposited in high doping regime, so it is consistent with the previous reports that we obtained Zn-polarity in the thicker films. Accordingly, it is reasonable to say that the growth of GZO starting with nucleation of possibly both Zn-polar and O-polar grains but O-polar dominant, and then flipping to Zn-polarity with increasing film thickness. Such the polarity inversion occurred at early stage of film growth at very thin films.

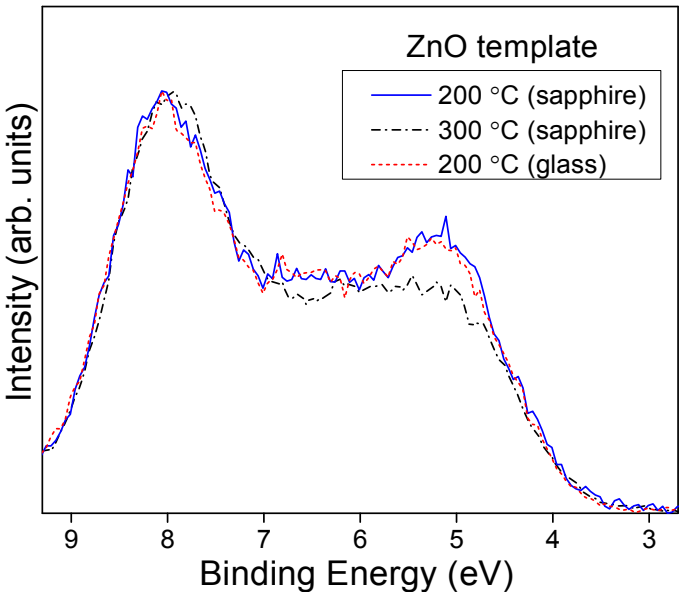

Fig. 6.7 Valence band spectra of ZnO templates deposited on glass and sapphire substrates.

In order to explore the influence of polarity on electrical properties of GZO films more clearly, we examined GZO films deposited on ZnO templates having different polar faces, that is, Zn-polar and O-polar faces. We prepared two kinds of ZnO films using ion plating with direct current arc discharge. Fig. 6.7 showed the VB of XPS spectra of un-doped ZnO films with film thickness of 200 nm deposited on *c*-plane sapphire substrates at the substrate temperature of 200 °C and 300 °C. It can be seen that the ZnO film deposited at 200 °C shows typical feature of Zn-polar face, while that deposited at 300 °C shows characteristics of O-polar face. On these ZnO films,

the 30 nm thick GZO film was deposited using the RF-MSP at the same deposition conditions mentioned above. The electrical properties of these GZO films are summarized in Table 6.1. We can recognize that the carrier concentration and the Hall mobility of the GZO film on O-polar ZnO were much smaller than those on Zn-polar ZnO. This result suggests that the electrical properties of GZO films are seriously influenced depending on the polarity.

Table 6.1 Electrical properties of 30 nm-thick GZO films deposited on Zn-polar faces and O-polar faces. A 30 nm GZO film deposited on glass without a ZnO template is also listed for comparison.

30 nm GZO films on:	ρ (Ωcm)	μ (cm^2/Vs)	N (cm^{-3})
Zn-polar ZnO (sapphire)	2.09×10^{-4}	32.7	9.11×10^{20}
O-polar ZnO (sapphire)	6.50×10^{-4}	19.9	4.83×10^{20}

30 nm GZO films on:	ρ (Ωcm)	μ (cm^2/Vs)	N (cm^{-3})
Zn-polar ZnO (glass)	**2.62×10^{-4}**	**26.9**	**8.87×10^{20}**
Glass w/o template	1.44×10^{-3}	11.9	3.64×10^{20}

Based on the result, we also prepared a Zn-polar ZnO film on glass substrate using the ion-plating at the substrate temperature of 200 °C. The VB spectra of the ZnO film was also plot in Fig. 6.7. The result supports the Zn-polar face of ZnO layer even on the glass substrate. Then 30 nm thick GZO film was deposited on the ZnO template on glass, and its electrical properties are also listed in Table 6.1 together with that of bare glass substrate without the ZnO template. Indeed, we observed significant improvement of the electrical properties. The resistivity, Hall mobility, and carrier concentration was 2.62×10^{-4} Ωcm, 26.9 cm^2/Vs, and 8.87×10^{20} cm^{-3}, respectively. Surprisingly, these properties were much better than those of the GZO film on O-polar ZnO on sapphire, although it was deposited on glass substrate. It should be mentioned that the significant improvement was not owing to structural properties. It has been known that the *c*-axis orientation is one of the key structural properties which influence to the electrical properties of doped ZnO films [9, 20].

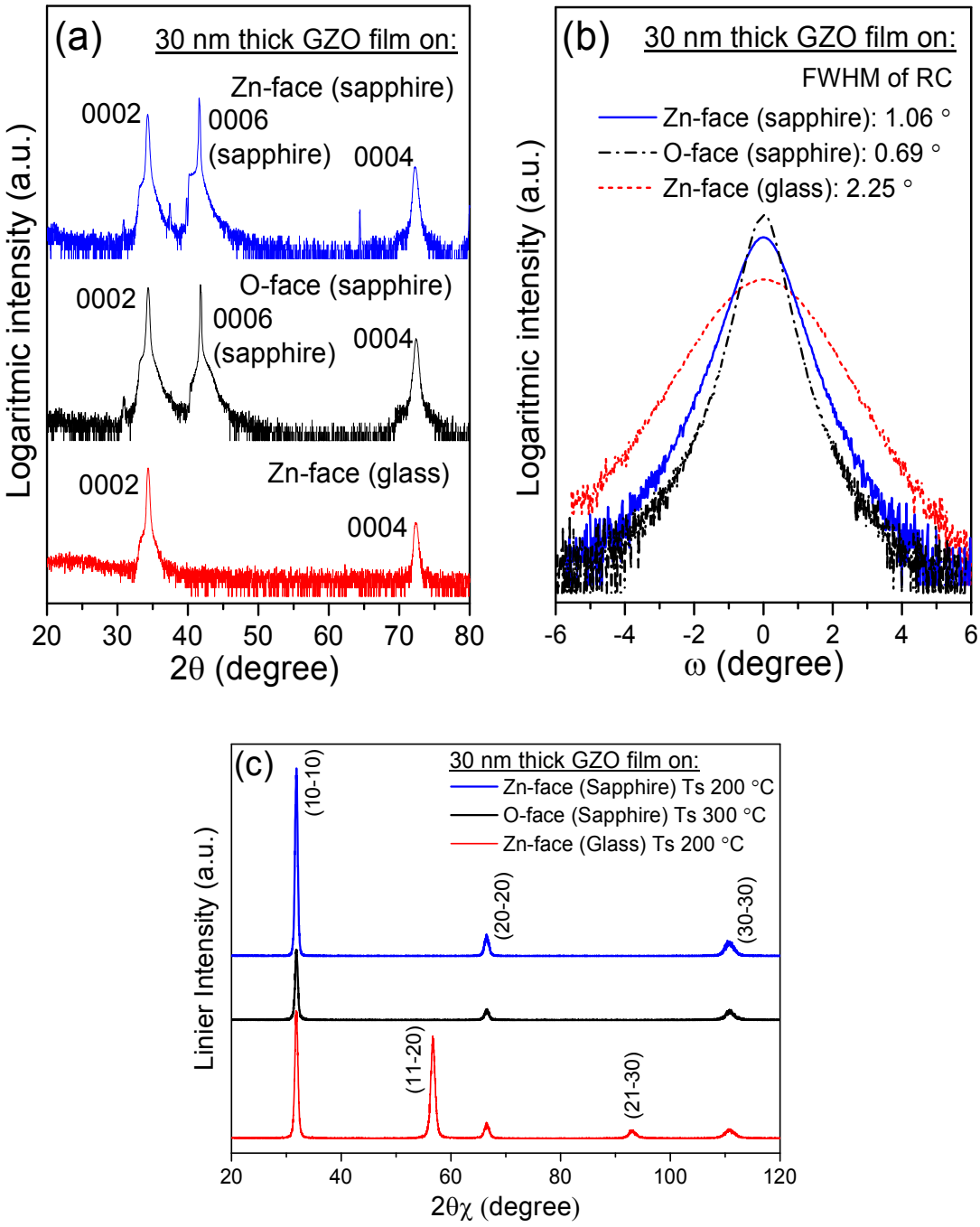

Fig. 6.8 The out-of-plane 2θ-ω scan (a), (0002) ω rocking curve (b) and in-plane 2θχ-φ scan (c) of 30 nm-thick GZO films deposited on Zn-polar and O polar faces.

Fig. 6.8 (a) and (c) shows the out-of-plane and in-plane XRD diffraction patterns of GZO films deposited on the ZnO templates. It was also confirmed that the films showed alignment of *c*-axis normal to the substrates. In addition, we only observed 10-10, 20-20, and 30-30 in the in-plane XRD patterns of the GZO films deposited on sapphire substrates. This means that *a*-axis was also aligned in in-plane direction, and the epitaxial GZO films were successfully grown on the *c*-plane sapphire substrates without rotational domains. Fig. 6.8 (b) shows the FWHM of 0002 ω rocking curve for the 30 nm GZO films deposited on Zn-polar and O-polar face. The FWHM of GZO films on Zn-polar and O-polar ZnO using sapphire substrates were 1.06° and 0.69°, respectively. The FWHM of the GZO film on Zn-polar ZnO using glass substrate was 2.25°, and it was worse among them.

When we compare the results of Zn-polar face between glass and sapphire substrates, the carrier concentration was comparable, while the Hall mobility was a little bit higher on sapphire substrate. The higher Hall mobility on sapphire could be owing to better crystallinity of well aligned epitaxial films [21]. On the other hand, the electrical properties of GZO films on O-polar face showed poor electrical properties compared to those deposited on Zn-polar face even though the tilting of *c*-axis was smaller than the others. This also supports that the poor electrical properties of the GZO film on O-polar face is mainly caused by the polarity.

Such the improvement of electrical properties of highly doped ZnO on un-doped ZnO buffer layer has been reported [10, 14]. Look *et al* argued that the lower mobility of very thin AZO without ZnO buffer layer was due to the interface layer caused by lattice mismatch between substrate and film, which trap electrons and act as scattering centers, and then the influence of the interface layer could be reduced by inserting the ZnO layer or increasing film thickness [10]. However, this is not fully attributed to the present 30 nm thick GZO films. In the case of GZO thin films deposited on Zn-polar ZnO, such the interface layer could be reduced by the inserting the ZnO layer. However, this is not the case in the GZO thin film on O-polar ZnO.

It has been known that effectiveness of incorporation of dopant in ZnO strongly depends on the polarity [22]. We confirmed that the Ga content in the GZO film was relatively higher in the film deposited on O-polar ZnO face than that on Zn-polar face using intensity ratio between Ga 2*p* and Zn 2*p* core spectra measured by HE-XPS. This is also the case of the thickness dependence on glass, that is, relatively higher Ga content in the thinner films when we compared between the 30 nm thick and the 100 nm thick GZO films. In the case of growth on O-polar face, Ga species might be accumulated on the surface during RF-MSP deposition that will lead to the change of surface energy and surface adsorption coefficient for species of O and/or Zn [17]. However, when the film thickness and the surface energy increased during deposition, the nucleation predict to be enhanced. Then, it would be switch the polarity of surface from O-polar to Zn-polar together with increasing film thickness during deposition. Although detailed mechanisms on the low electrical properties of thin GZO films on O-polar face has not yet clear at the present, the polarity inversion strongly affects the electrical properties of GZO films especially very thin thickness below 100 nm.

6.3 Chapter Conclusions

In conclusion, the improvement of electrical properties of 30 nm thick GZO films was achieved by inserting a Zn-polar face of ZnO layer on glass substrate. The evolution of the VB spectra measured by HE-XPS suggests that the very thin GZO film was dominated by O-polarity, and then flipping to Zn-polarity with increasing films thickness. The GZO films deposited on Zn-polar face showed higher carrier concentration and higher mobility compared to the deposition on O-polar face owing to inhibition of polarity inversion. The growth on Zn-polar face leads to the improvement of electrical properties of very thin GZO films. These findings suggest that the polarity inversion plays an important role on the electrical properties of GZO thin films.

6.4 References

[1] N. Yamamoto, H. Makino, S. Osone, A. Ujihara, T. Ito, H. Hokari, T. Maruyama, T. Yamamoto, Thin Solid Films 520, 4131 (2012).

[2] J. K. Sheu and Y. S. Lu, M. L. Lee, W. C. Lai, C. H. Kuo, C. J. Tun, Appl. Phys. Lett. 90, 263511 (2007).

[3] T. Minami, T. Miyata, and J. Nomoto, IOP Conf. Ser.: Mater. Sci. and Eng. 34, 012001 (2012).

[4] M. Berginski, J. Hupkes, M. Schulte, G. Schope, H. Stiebig, and B. Rech, J. Appl. Phys. 101, 0749903 (2007).

[5] T. Minami, H. Sato, H. Nanto, and S. Takata, Jpn. J. Appl. Phys. 24 Part 2, L781 (1985).

[6] C. Agashe, O. Kluth, J. Hüpkes, U. Zastrow, B. Rech, and M. Wuttig, J. Appl. Phys. 95, 1911 (2004).

[7] T. Minami, T. Miyata, Y. Ohtani, and T. Kuboi, Phys. Status Solidi: Rapid Res. Lett. 1, R31 (2007).

[8] T. Yamada, A. Miyake, S. Kishimoto, H. Makino, N. Yamamoto, and T. Yamamoto, Appl. Phys. Lett. 91, 051915 (2007).

[9] T. Yamada, H. Makino, N. Yamamoto, and T. Yamamoto, J. Appl. Phys. 107, 123534 (2010).

[10] D. C. Look, K. D. Leedy, A. Kiefer, B. Claflin, N. Itagaki, K. Matsushima, and I. Surhariadi, Opt. Eng. 52, 033801 (2013).

[11] D. C. Look, B. Claflin, A. Kiefer, and K. D. Leedy, Opt. Eng. 53, 087108 (2014).

[12] A. Bikowski and K. Ellmer, J. Appl. Phys. 116, 143704 (2014).

[13] A. Bikowski, M. Rengachari, M. Nie, N. Wanderka, P. Stender, G. Schmitz, and K. Ellmer, APL Mater. 3, 060701 (2015).

[14] N. Itagaki, K. Kuwahara, K. Nakahara, D. Yamashita, G. Uchida, K. Koga, and M. Shiratani, Appl. Phys. Express 4, 011101 (2011).

[15] Y. Adachi, N. Ohashi, T. Ohgaki, T. Ohnishi, I. Sakaguchi, S. Ueda, H. Yoshikawa, K. Kobayashi, J. R. Williams, T. Ogino, and H. Haneda, Thin Solid Films 519, 5875 (2011).

[16] M. W. Allen, D. Y. Zemlyanov, G. I. N. Waterhouse, J. B. Metson, T. D. Veal, C. F. McConville, and S. M. Durbin, Appl. Phys. Lett. 98, 101906 (2011).

[17] A. V. Kvit, A. B. Yankovich, V. Avrutin, H. Liu, N. Izyumskaya, U. Ozgur, H. Morkoc, and P. M. Voyles, J. Appl. Phys. 112, 123527 (2012).

[18] T. Ogino, J. R. Williams, K. Watanabe, I. Sakaguchi, S. Hishita, H. Haneda, Y. Adachi, T. Ohgaki, N. Ohashi, Thin Solid Films 552, 56 (2014).

[19] A. Abduev, A. Akmedov, A. Asvarov, and A. Chiolerio, Plasma Process. Polym. 12, 725 (2015).

[20] K. Maejima, H. Shibata, H. Tampo, K. Matsubara, and S. Niki, Jpn. J. Appl. Phys. 51, 10NC16 (2012).

[21] H. Makino, H. Song, and T. Yamamoto, Thin Solid Films 559, 78 (2014).

[22] H. Maki, I. Sakaguchi, N. Ohashi, S. Sekiguchi, H. Haneda, J. Tanaka, and N. Ichinose, Jpn. J. Appl. Phys. 42, 75 (2003).

7. Hydrogen gas sensor based on GZO thin films

7.1 Introduction

In the last few years, considerable attention has been paid to hydrogen as a one of promising clean energy resources in the world [1]. There a lot of advantages of hydrogen in wide area, i.e., hydrogen for fuels, automobile, fuel cells, chemical material industry, etc [2, 3]. Based on the reference [3], hydrogen gas was flammable and explosive on the concentration of higher than 4% in air. Since hydrogen gas has specific properties such as tasteless, odorless, colorless, and also un-detectable by human senses, development of highly sensitive and reliable hydrogen gas sensors with fast response and recovery times become very important to detect leakage in the environment.

Metal oxide semiconductors such as ZnO have been considered as one of promising candidates of sensing materials for such gas sensors. Look *et al* [4] stated that the reactive surface of ZnO is strongly suitable for gas sensing materials. The reactive surface leads to the change of electrical properties through charge transfer interactions with reactive gases in environment such as hydrogen, oxygen, carbon monoxide, ethanol, etc [5]. In the last few years, the gas sensors for such specific target gas have been reported using n-type semiconductors, e.g., SnO_2, In_2O_3, and ZnO. Gas sensors based on p-type materials such as CuO have been also reported recently by Lupan *et al* [6]. In the case of gas sensors based on ZnO, Al-hardan *et al* reported that the conductivity was controlled by surface reactions [1]. The mechanism was mainly attributed to the surface charge at grains [1]. Haidry *et al* suggested that the sensitivity of TiO_2 thin films to hydrogen gas was enhanced by increment of surface roughness that offer more adsorption sites [7]. Enachi *et al* discussed the effects of annealing on hydrogen gas sensing properties of TiO_2 based sensing materials [8].

On the other hand, the effects of doping on metal oxide gas sensors have been discussed as well. It was reported that the additive such as gallium and phosphorus would be useful for optimization of gas sensing characteristics in the case of gas sensors based on In_2O_3 [9]. Korotcenkov *et al* also reported a correlation between grain size and influence of air humidity on sensitivity in the gas sensors using highly Ga-doped In_2O_3 [9]. Another study reported that the doping of Cr to ZnO lead to the enhancement of sensitivity at low operating temperature [10]. The improvement was attributed to the higher oxidation state of chromium [10]. Recently, Kishimoto *et al* reported gas sensors based on GZO thin films that showed large change of current under exposure to carbon monoxide [11]. In their study, a correlation between electrical properties of as-deposited GZO films and gas sensing characteristics has been explored, however, it was not clearly observed [11].

The microstructure sensing materials such as grain size have been known as one of main factors to determine sensitivity of gas sensors based on metal oxides. Several studies related to the effects of grain size to the performance of gas sensor have already published [4, 5, 12-13]. The effect of crystallographic planes on sensing properties has been also reported for the gas sensor based on SnO_2 [14, 15].

In the case of ZnO based TCOs, the microstructure of the thin films like as grain size and *c*-axis orientation strongly influence to their transport properties as discussed in the preceding three chapters in this thesis. However, the effects of structural properties on gas sensing are still not yet clarified for ZnO based gas sensors. Based on the brief survey of literatures, the sensing characteristics of hydrogen gas sensors based on highly doped ZnO such as GZO has not yet well understood. In this chapter, influences of grain size and *c*-axis orientation on hydrogen gas sensing properties has been studied for highly Ga-doped ZnO thin films deposited by RF magnetron sputtering.

7.2 Experimental

Highly doped GZO thin films were deposited by radio-frequency (RF) magnetron sputtering method using a ZnO:Ga_2O_3 5.7 wt% target at substrate temperature (*Ts*) of 200 °C with Ar flow rate of 450 sccm and RF power of 100 W. Two series of GZO films have been prepared on glass substrates. One is GZO films directly deposited on bare glass substrates with film thickness about 30 nm, 50 nm and 100 nm (hereafter referred to as "S1, S2, and S3, respectively"). Another one is 30 nm thick-GZO films deposited on undoped ZnO template with film thickness about 30 nm, 80 nm and 200 nm (hereafter referred to as "S4, S5, and S6, respectively"). The ZnO templates were deposited by ion plating method on glass substrates at *Ts* of 200 °C in order to control the microstructure of GZO films. We also prepared 30 nm thick GZO films on ZnO templates deposited on *c*-plane sapphire substrates. The structural properties were characterized by X-ray diffraction measurement.

The evaluation of gas sensor response was performed using a custom-made set-up for gas sensing measurement. The GZO film was cut in a 5 mm square, and two circular Au electrodes in diameter of 1 mm were deposited on the films. The distance between electrode was about 1 mm. The sample was placed on a compact cylindrical chamber with a volume of approximately 200 cm^3, and the sample was heated up to 330 °C. Current was monitored using a system source meter (2602A, Keithley) with an applied voltage of 3 V. Details on the measurement system have been reported elsewhere [11]. Pure N_2 gas was continuously flowed into the test chamber at a flow rate of 300 sccm, and then a mixture gas of N_2 and 1% H_2 gas was additionally introduced at a flow rate of 100 sccm for the sensing measurements. The condition corresponds to introduction of 0.25 % H_2 gas diluted by pure N_2 gas. The flowing time period of H_2 mixture gas was 10 s for each measurement and repeated several times to see stability of the response.

7.3 Experimental results and discussion

7.3.1 Structural properties

Fig. 7.1 show the out-of-plane 2θ-ω scan (a) and the variation of FWHM 0002 ω-rocking curve and grain size (b) for sample S1, S2, S3, S4, S5, and S6. It can be seen that all of sample showed preferred *c*-axis orientation which only showed 0002 and 0004 diffraction peaks without any other peaks. The intensity of 0002 and 0004 peak increased as increasing the film thickness. The increase of diffraction intensity suggests improvement of crystallinity of the films. To evaluate the degree of *c*-axis orientation, the FWHM of 0002 ω-rocking curve were compared in Fig. 7.1 (b). The FWHM decreased as increasing the film thickness. Accordingly, the preferred orientation in *c*-axis improved as the film thickness increases. We also estimated the grain size by Williamson-Hall plot for in-plane XRD measurement and plotted in Fig. 7.1 (b). It can be seen that the grain size increased as increasing film thickness. The details on structural properties of GZO thin films deposited on bare glass substrates can be seen in chapter 6 and in reference [16].

For the GZO films deposited on ZnO templates, the relationship between the FWHM of 0002 ω-rocking curve and the grain size showed a little difference. The grain size seems nearly determined by the total thickness of ZnO and GZO layers. The sample S6 showed the largest grain size, this is due to the total thickness of this sample was about 230 nm. The total thickness of S5 (~110 nm) and S3 (~100 nm) were comparable, resulting in comparable grain size of about 30 nm. The S4 was totally ~ 60 nm that nearly comparable with S2 (~ 50 nm). The grain size of these two samples was ~ 23 nm. The S1 sample showed the smallest grain size of ~ 21 nm compared to those of all other samples.

On the other hand, the FWHM of 0002 ω-rocking curve was entirely narrower than that of the GZO films on bare glass. For instance, the thickness of S4 was nearly comparable with that of the S2, however, the FWHM of 0002 ω-rocking curve for the

S4 was obviously smaller than that of the S2. This is because of higher degree of *c*-axis orientation in the case of undoped ZnO templates deposited by the ion-plating.

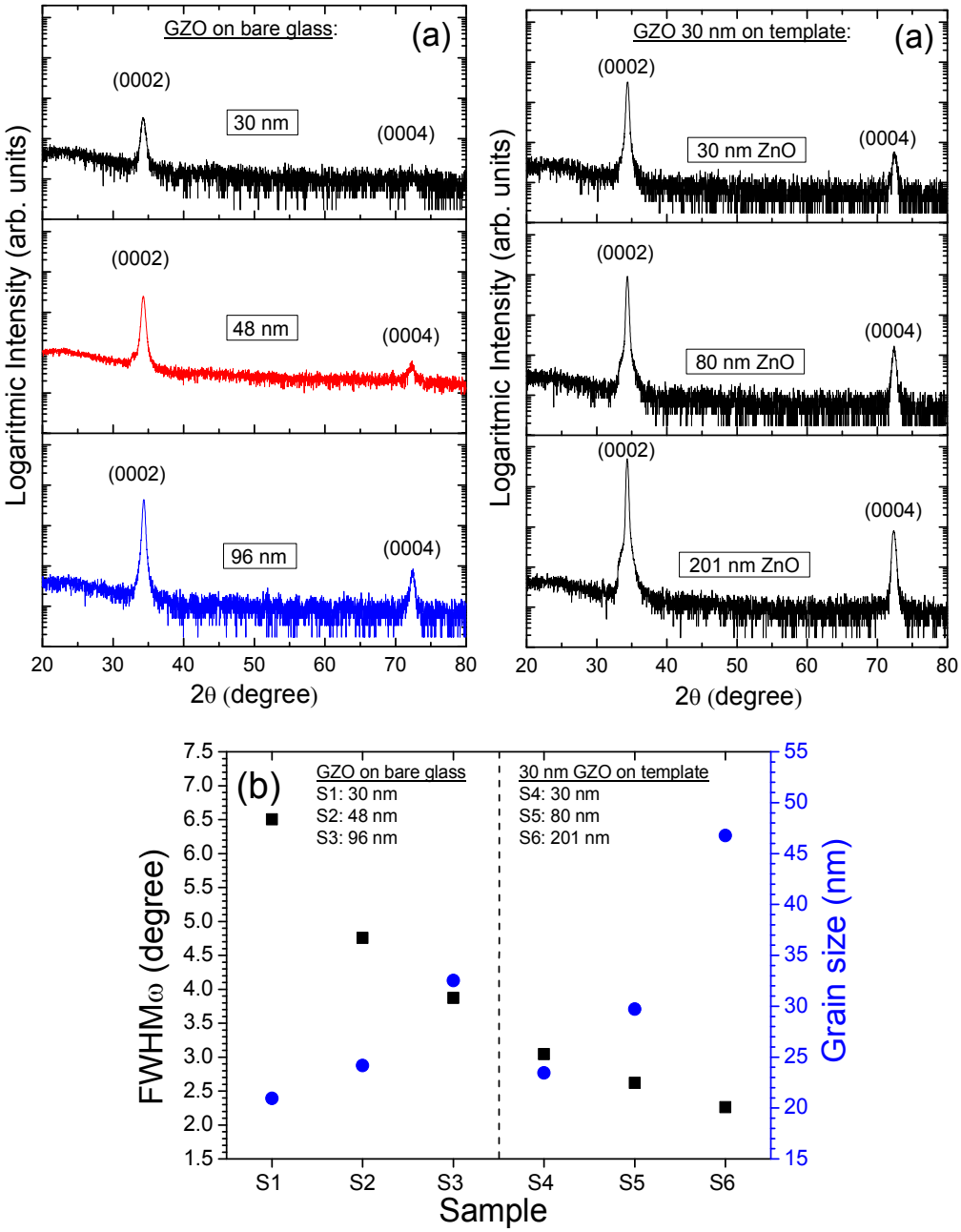

Fig 7.1 Out-of-plane 2θ-ω scan of XRD measurement (a) and variation of FWHM 0002 ω-rocking curve and grain size (b) for GZO films deposited on bare glass and ZnO templates.

7.3.2 Sensing characteristics

For the semiconductors, the bulk conductance of thin films can be defined as [17]:

$$G = Nq\mu\frac{wd}{L}$$

where *N* is a bulk carrier concentration, μ is the mobility of electron, and w, *d, L* are width, film thickness and length, respectively. In the case of gas sensors, the conductance would increase when carrier concentration or hall mobility increases by reactions with hydrogen gas.

The definition of sensitivity can be calculated by [17]:

$$S = \frac{\Delta G}{G_0} = \frac{\Delta R}{R_g} = \left(\frac{R_o - R_g}{R_g}\right)$$

where G_0 and Ro are the conductance and resistance before expose to air and G_g and Rg are the conductance and resistance after the sample expose to hydrogen, respectively. It should be mentioned here that the GZO layer dominantly contribute to the conductivity measurements because of large difference in conductivity between the highly doped GZO layer and the undoped ZnO template. The contribution of ZnO layer on gas sensing measurements would be nearly negligible in this study.

Fig. 7.2 shows the sensing characteristic of hydrogen gas sensor based on GZO films. Here, the time of H_2 gas introduction was settled to zero for each measurement. Fig. 7.2 (a) is the dynamic response for typical S1 sample. The resistance of sample before exposed to hydrogen (R_0) is about 5430 Ω. The resistance decreased after exposed to hydrogen gas (R_g) to about 1038 Ω. Then the change of resistance (R_0-R_g) or ΔR was about 4392 Ω. The sensitivity was calculated by $\frac{\Delta R}{R_g}$, and it was 4.23. The response curves $(R_0 - R)/R_g$ of each samples are plotted in order to compare the tendency of

sensing characteristics in Fig. 7.2 (b). It was found that the sample S1 showed the highest sensitivity. Inset of Fig. 7.2 (a) shows introduction of H_2 gas.

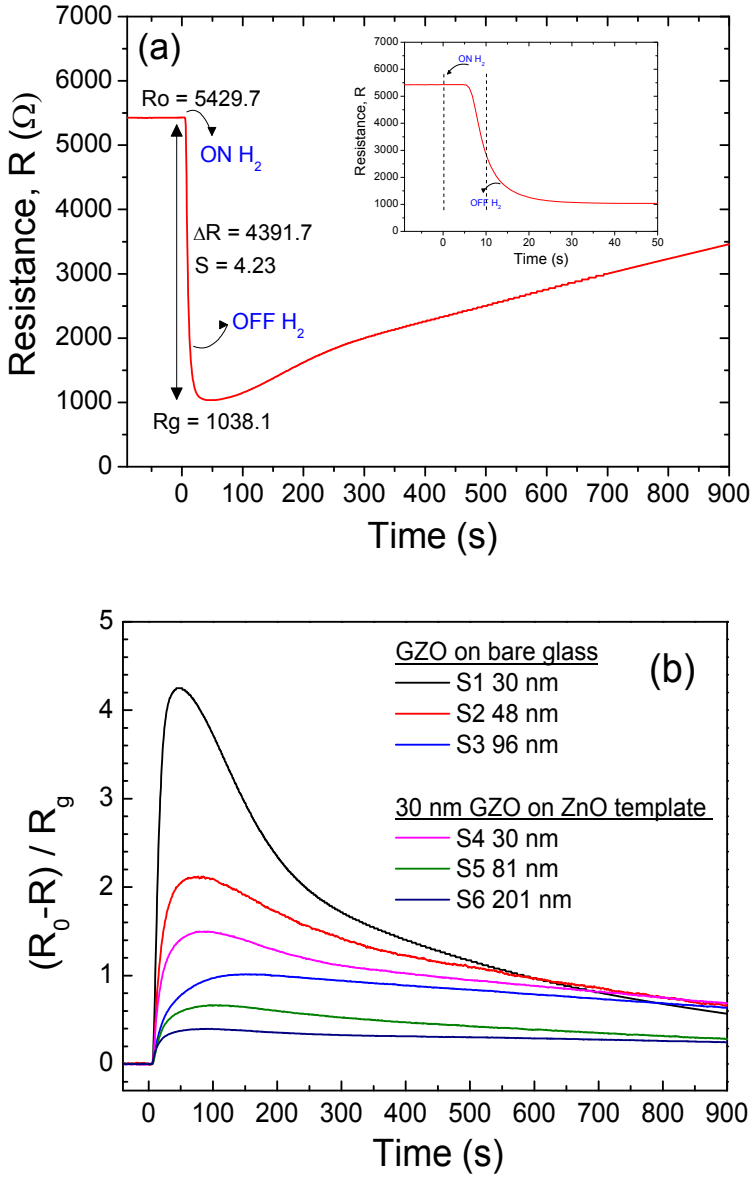

Fig. 7.2 The typical dynamic response base on change of resistance for 30 nm GZO films deposited on a bare glass (a) and variation in sensitivity curve as a function of time (b).

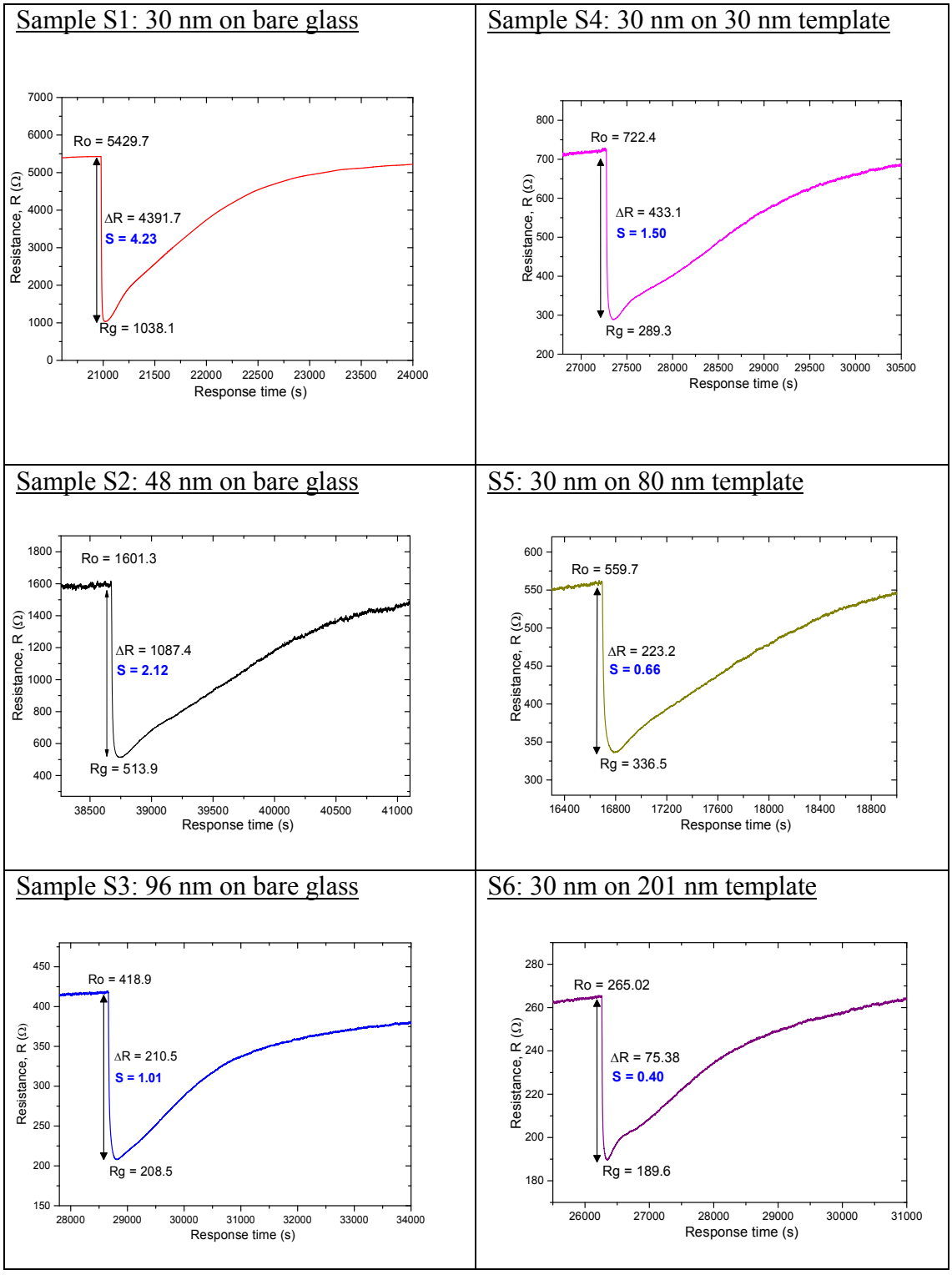

Fig. 7.3 The dynamic response of S1, S2, S3, S4, S5, and S6.

The dynamic response curves of other samples are plotted in Fig. 7.3, in order to show the variation of practical values of R_0, R_g, and ΔR. The value of ΔR represented the change of resistance before and after exposure to hydrogen gas. The sensitivity value seems depends on not only ΔR but also the R_o.

7.3.3 Relationship between grain size and *c*-axis orientation to the sensitivity

Fig. 7.4 (a) shows the relationship between grain size with the gas sensitivity for hydrogen. It can be seen that the highest sensitivity has been achieved on sample S1 which has the smallest grain size of ~21 nm. Interestingly, in the case of S4 sample, even grain size (~23 nm) was smaller than that of S3 sample (~33 nm), but the sensitivity was comparable. The S1 and S4 showed nearly comparable grain size of ~21 nm and ~23 nm, respectively, however, the sensitivity was largely different. Based on this result, it seems that the grain size was not the main factor to determine the sensitivity of GZO thin films. The Fig. 7.4 (b) shows the relationship between the FWHM of ω-rocking curve and the sensitivity. The sample S1 with the widest FWHM value of 6.5-degree showed the highest sensitivity, whereas the narrowest FWHM of S6 showed the lowest sensitivity. The sensitivity obviously increased with increasing the FWHM of ω-rocking curve. A sample S7 was additional sample of 30 nm-thick GZO films deposited on ZnO template using sapphire substrate [16]. This sample showed very well oriented films due to characteristics of single crystalline epitaxial layer. The FWHM for this sample was 1.06, and the grain size was ~ 82 nm. Details on this sample has already shown in chapter 6. Another additional sample was S8, which is 30 nm thick GZO films but using 3 wt% Ga_2O_3 doped ZnO target deposited on 30 nm thick ZnO template on glass substrate. The grain size and FWHM of this sample were ~ 29 nm and 3.21 degree, respectively.

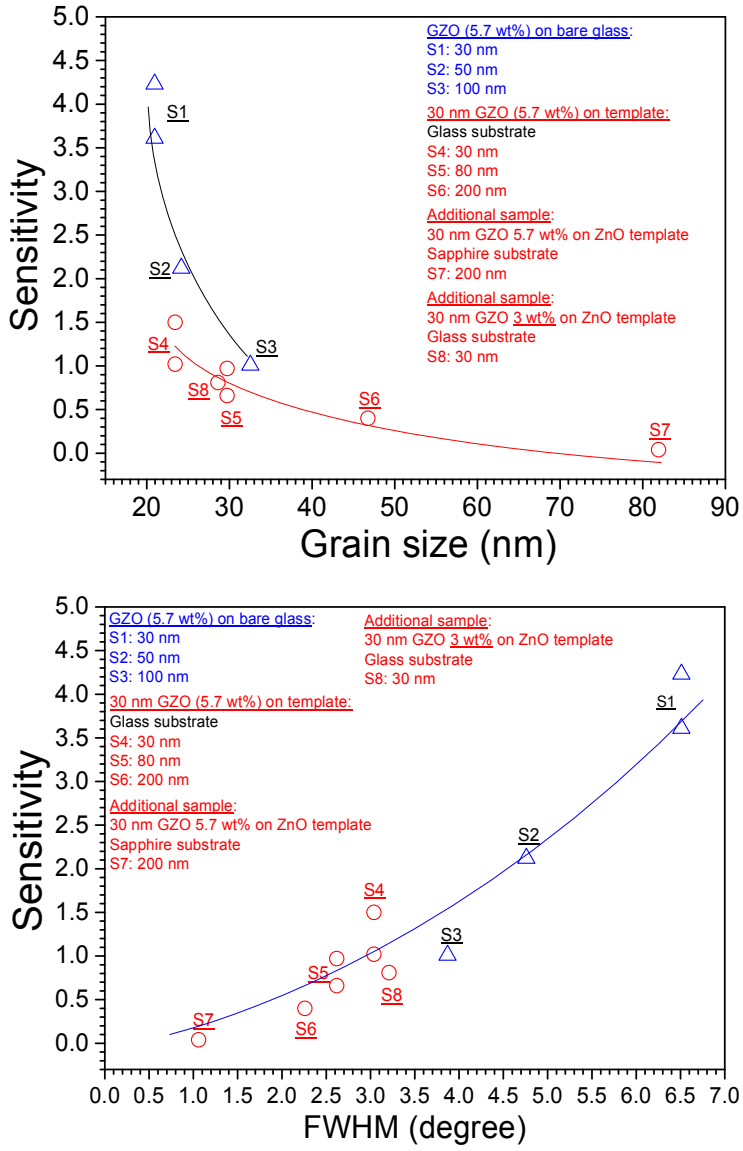

Fig. 7.4 Effects of grain size (a) and the degree of *c*-axis orientation (b) to the sensitivity of GZO films deposited on bare glass and ZnO template.

7.3.4 Sensing mechanism of hydrogen gas sensors

Since a long time ago researcher have discussed about possibility where is gas sensing taking place [5, 18, 19]. In order to obtain knowledge about this issue on the polycrystalline GZO films, we prepared an additional sample of 30 nm-thick GZO

film using an epitaxial ZnO template grown on sapphire substrate (S7 in Fig. 7.4). The film not only showed orientation in c-axis normal to the substrate, but also showed well oriented *a*-axis in in-plane direction without rotational domains due to epitaxial growth on single crystalline substrates. The hydrogen gas sensitivity was 0.04 widely smaller than others. Considering the fact that the sensitivity depending on grain size and *c*-axis orientation, we consider here that the hydrogen gas sensing in the GZO films deposited on glass substrate is taking place not only at surface but also at grain boundaries. In the case of well oriented films like as S7, the reaction takes place most probably only at the surface, while the reaction takes place at surface and sensitive grain boundary in the case of poor *c*-axis orientation or high tilting of *c*-axis.

Surface roughness has been considered to be another factor to determine gas sensitivity [20]. We characterized surface roughness of typical samples by atomic force microscopy. The GZO films deposited on glass substrates showed very flat surface and comparable roughness. The RMS roughness was 0.74 nm for 40 nm thick film and 0.99 nm for 100 nm thick film, respectively. We cannot expect any influence of surface roughness on the sensitivity in the present case.

The change of resistance will be governed by the occurrence of oxygen adsorption-desorption that will lead to the change of gas sensitivity. Before the sample exposes to the hydrogen gas, the sensitive layer will adsorb oxygen molecules in air. Then the electron from conduction band will be captured by this oxygen change to oxygen ions. Subsequently, the number of electrons in thin films will decrease that will lead to the increasing of resistance. In the case of GZO films exposed to the air, the gas reaction at operating temperature of sensing test can be express as follow:

$$O_2(ads) + e^- \rightarrow O_2^-(ads) + e^- \rightarrow 2O^-(ads)$$

When the films expose to hydrogen gas, the molecules of hydrogen will diffuse to the layer of GZO films resulting in the reaction between the molecules and the oxygen

ions on films layer. The hydrogen molecule interacts with the adsorbed oxygens. The results of reaction will release the electrons back to the conduction band resulting in the decreasing of resistance. The reaction when the GZO films expose to the hydrogen gas at operating temperature of 330 °C can be shown as follow:

$$H_2 + O^-(ads) \rightarrow H_2O(des) + e^-$$

Next, let us discuss about the effects of grain size and *c*-axis orientation on the sensitivity. According to the reference, when the grain size decreases, the number of grains and the amount of grain boundaries would be increased [5]. Based on this, the sensing area will increase with decreasing the grain size [5]. Accordingly, the amount of oxygen adsorbates will increase [21]. The increase of sensing area or oxygen adsorbates resulted in the enhancement of H_2 sensitivity [5]. Such the effect of grain size seems observed in gradual increase of sensitivity with decreasing the grain size for GZO films deposited on the ZnO template (S4, S5, and S6).

As shown in Fig. 7.4 (b) of previous section, the sensitivity of GZO films was depending on the *c*-axis orientation. One of possible explanations for the effects of *c*-axis orientation is increase of density of reaction sites with increasing the FWHM of ω rocking curve. When the *c*-axis shows highly tilting, it might lead to increase of adsorption sites for oxygens like as dangling bonds of Zn at grain boundaries. According to the molecular orbital theory, it has been known that ZnO involves the four Zn dangling bonds (sp3 hybrids) and two electrons that will related to the formation of oxygen vacancy (V_O) [22]. The higher density of adsorption sites at grain boundaries similar to the V_O may result in the higher sensitivity. The adsorption of some chemical species may have preference to be occurs on the corner and edge sites or on their plane facet [23]. Such the effect also might be lead to higher sensitivity of highly c-axis tilting GZO thin films.

Another possible explanation is diffusivity of gas through grain boundaries. When the samples have higher tilting of *c*-axis, the grain boundaries will be sparser than the well oriented samples. In this case, the oxygen can diffuse into more deeply inside of the GZO films thorough grain boundaries to form sensitive grain boundaries. When the samples have comparable grain size, the area of grain boundaries is also comparable, however, the density of adsorbed oxygens could be different depending on the situation of *c*-axis orientations because of the higher density of adsorption sites or the higher diffusivity of gas thorough grain boundaries.

Although the sensing mechanism of GZO films is still not yet clear at the present, it seems that the degree of *c*-axis orientation plays an important role on the sensing of hydrogen gas by highly Ga-doped ZnO polycrystalline thin films deposited by RF magnetron sputtering on glass substrates. As shown in Fig. 7.5, in the case of well oriented GZO thin films like as epitaxial layer on sapphire substrates, the sensing is dominated at the surface. In the case of poor oriented GZO thin films, the grain boundary is more sensitive resulting in the higher sensitivity of gas sensors.

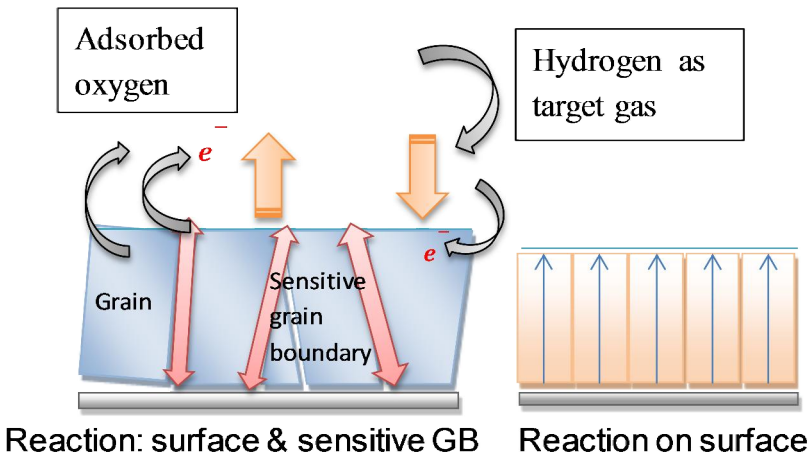

Fig. 7.5 Schematic picture of enhancement of hydrogen gas sensitivity in highly Ga-doped ZnO thin films.

Finally, influence of Ga doping density in GZO films was preliminarily checked in this study. Korotcenkov et al showed that there was influence of doping additive of Ga to In_2O_3 [24]. It was also reported that doped ZnO lead to higher donor content of V_O that can modify surface state resulting the enhancement of gas sensing [25, 26]. We prepared another additional sample (S8) of 30 nm thick-GZO film deposited on ZnO template using 3wt% Ga_2O_3 doped ZnO ceramic target. This sample showed grain size about 29 nm (FWHM of ω rocking curve: 3.2 degree) that was comparable with sample S5 with grain size about 30 nm (FWHM of ω rocking curve: 2.6 degree). These two samples showed really comparable sensitivity of about 0.8. We could not see any dependence on doping density within the doping level studied here.

7.4 Chapter Conclusions

In summary, the sensitivity of highly Ga-doped ZnO thin films was mainly determined by tilting of *c*-axis compared to grain size. The highest sensitivity as high as 4.23 for concentration 0.25 % of H_2 gas at 330 °C was achieved by 30 nm thick-GZO films deposited on bare glass which have the smallest grain size and the highly tilting of *c*-axis. On the other hand, the sensitivity was as low as 1 to 1.5 for samples which showed higher preferred *c*-axis orientation. These findings are important for gas sensing devices base on highly Ga-doped ZnO thin films.

7.5 References

[1] N. H. Al-Hardan, M. J. Abdullah, A. A. Aziz, Int. J. Hydrogen Energy 35, 4428 (2010).

[2] M. Fleischer and H. Meixner, J. Vac. Sci. Technol. A 17, 1866 (1999).

[3] A. Katoch, Z. U. Abideen, H. W. Kim, and S. B. Kim, ACS Appl. Mater. Interfaces 8, 2486 (2016).

[4] D. C. Look, J. Electron. Mater. 35, 1299 (2006).

[5] A. Rothschild and Y. Komem, J. Appl. Phys. 95, 6374 (2004).

[6] O. Lupan, V. Postica, V. Cretu, N. Wolff, V. Duppel, L. Kienle, and R. Adelung, Phys. Status Solidi RRL 10, 260 (2016).

[7] A. A. Haidry, J. Puskelova, T. Plecenik, P. Durina, J. Gregus, M. Truchly, T. Roch, M. Zahoran, M. Vargova, P. Kus, A. Plecenik, and G. Plesch, Appl. Surf. Sci. 259, 270 (2012).

[8] M. Enachi, O. Lupan, T. Braniste, A. Sarua, L. Chow, Y. K. Mishra, D. Gedamu, R. Adelung, and I. Tiginyanu, Phys. Status Solidi RRL 9, 171 (2015).

[9] G. Korotcenkov, I. Boris, V. Brinzari, S. H. Han, B. K. Cho, Y. N. Lychkovsky, Ceram. Int. 41, 7478 (2015).

[10] N. Al-Hardan, M. J. Abdullah, A. A. Aziz, H. Ahmad, Appl. Surf. Sci. 256, 3468 (2010).

[11] S. Kishimoto, S. Akamatsu, H. Song, J. Nomoto, H. Makino, and T. Yamamoto, J. Sens. Sens. Syst. 3, 331 (2014).

[12] G. Korotcenkov and B. K. Cho, Sensors and Actuators B 156, 527-538 (2011).

[13] G. Korotcenkov, S. H. Han, and B. K. Cho, J. Sens. Sci. Technol. 22, No 1, pp. 1-17 (2013).

[14] G. Korotcenkov, Sensors and Actuators B 107, 209 (2005).

[15] V. Brinzari, G. Korotcenkov, and V. Golovanov, Thin Solid Films 391, 167 (2001).

[16] L. Nulhakim and H. Makino, Phys. Status Solidi RRL 10, 535 (2016).

[17] S. R. Morisson, Sens. Actuators 2, 329-341 (1982).

[18] N. Barsan and U. Weimar, J. Electroceram. 7, 143-167 (2001).

[19] G. Korotcenkov, Mater. Sci. Eng. B 139, 1-23 (2007).

[20] T. Tesfamichael, C. Cetin, C. Piloto, M. Arita, and J. Bell, Applied Surface Science 357, 728-734 (2015).

[21] Y. Shimizu, F.C. Lin, Y. Takao, and M. Egashira, J. Am. Ceram. Soc. 81, 1633 (1998).

[22] A. Janotti and C. G. Van de Walle, Rep. Prog. Phys. 72, 126501 (2009).

[23] G. Korotcenkov, Mater. Sci. Eng. R 61, 1-39 (2008).

[24] G. Korotcenkov, Ceramic International 41, 7478 (2015).

[25] S. Bai, T. Guo, Y. Zhao, R. Luo, D. Li, A. Chen, and C. C. Liu, J. Mater. Chem. A 1, 11335 (2013).

[26] N. Illyaskutty, H. Kohler, T. Trautmann, M. Schwotzer, and V. P. M. Pillai, J. Mater. Chem. C 1, 3976 (2013).

8. Concluding Remarks

The studies reported in this thesis have investigated topics related to properties of polycrystalline Ga-doped ZnO thin films as transparent conductive films, and to hydrogen gas sensor using Ga-doped ZnO thin films as sensing materials. The structural, electrical, optical, and transport properties of GZO thin films deposited by RF magnetron sputtering have been investigated. The studies especially focus on the influence of structural properties of polycrystalline GZO thin films like as grain size and *c*-axis preferred orientation. In this thesis, such the structural properties have been artificiality controlled using highly *c*-axis oriented ZnO based thin films called as buffer layer, or seed layer, or template for growth of over layer, in order to discuss the influence of the structural properties more clearly. Concerning the carrier transport properties of polycrystalline GZO films, optical mobility, which is evaluated by optical spectroscopy, has been positively employed as effective measure to discuss charge carrier scattering mechanisms.

As the first topic, influences of microstructural properties and defects caused by ion bombardment during film deposition by RF magnetron sputtering on electrical, optical, and transport properties of polycrystalline GZO films have been separately discussed. To separate the influences, control of microstructure and post-deposition annealing has been employed in sequence. It was clearly observed that the contribution of grain boundary scattering resulting in the lower Hall mobility compared to the optical mobility reflecting in-grain electron mobility was caused by the partially oriented domains like as (10-11) planes different from the main preferred orientation of *c*-plane. It was clarified that the *c*-axis orientation reduces the contribution of grain boundary scattering. The defects formed by ion bombardment can be gradually annealed out with increasing substrate temperature. The reduction of defects was resulting in improvement in-grain mobility and transparency of the films. These findings suggest two important factors to be considered to improve performance of GZO films deposited at RT, one is *c*-axis orientation in order to reduce the grain boundary scattering and another one is elimination of defects caused

by the ion bombardment during the deposition process. It should be emphasize that such defects cannot be simply reduced only by controlling the microstructure.

For the practical application of GZO films as transparent electrodes, extremely thin film with good electrical properties is required sometimes depending on the purpose. The one of critical issue of ZnO based TCO is obvious thickness dependence of electrical resistivity, that is, the resistivity strictly increased with decreasing the film thickness. In order to overcome this issue, influence of crystallographic polarity has been investigated in this thesis. It was found that polarity inversion plays an important role to determine electrical properties of heavily doped GZO thin films especially very thin thickness region. The growth as Zn polarity is quite important for highly doped GZO thin films to realize fairly low resistivity.

As the second topic, the hydrogen gas sensors based on polycrystalline GZO thin films have been investigated in this thesis with focused light on the effects of structural properties on the sensitivity. The effects of c-axis orientation on the sensitivity have been explored for the first time. It was found that not only grain size but also c-axis orientation is important factors to influence the hydrogen gas sensitivity of the heavily doped GZO films.

It is believed that these findings obtained through the studies in this thesis powerfully contribute to develop any kinds of applications based on Ga-doped ZnO thin films.

List of Figures

1. Introduction

No Figure

2. Fundamentals

3. Research Methodology

4. Controlling of microstructure and annealing out of defects: their effects on properties

5. Change of scattering mechanism and annealing out of defects with increasing substrate temperature

6. Effects of polarity inversion on the electrical properties

7. Hydrogen gas sensor based on GZO thin films

List of Tables

Publications

1) **L. Nulhakim** and H. Makino: Control of microstructure by using self-buffer layer and its effects on properties of Ga-doped ZnO thin films deposited by radio frequency magnetron sputtering. ***Thin Solid Films*** 615, 158-164 (2016).

2) **L. Nulhakim** and H. Makino: Change of scattering mechanism and annealing out of defects on Ga-doped ZnO films deposited by radio-frequency magnetron sputtering. ***Journal of Applied Physics*** 119, 235302 (2016).

3) **L. Nulhakim** and H. Makino: Influence of polarity inversion on the electrical properties of Ga-doped ZnO thin films. ***Physica Status Solidi (RRL) - Rapid Research Letters*** 10, 535-539 (2016).

4) **L. Nulhakim**, H. Makino, S. Kishimoto, J. Nomoto, and T. Yamamoto: The sensitivity of hydrogen gas sensor based on highly Ga-doped ZnO thin films influenced by tilting of *c*-axis preferred orientation. (To be submitted, 2016).

Acknowledgement

First of all, I would like to thank my supervisor Prof. Hisao Makino for his guidance and insightful advice for my research work throughout the whole three years. His research route advice was very powerful and it was always gave a significant meaning on my improvement of research results. I would like to thank him for his patience and time to transfer a lot of advance research skills, research knowledge and experiences. He always tried to help me understand in the details of my research, for example, he did not just explain how to operate research equipment system but he always tried to get me to understand the basic principle of the equipment, and to always improve the quality of my analysis and research results.

Thank you for Dr. Junichi Nomoto from Research Institute of KUT, for his fruitful discussions and for creating a pleasant atmosphere during my research experiments and study. Thank you for his help to understand the principle of sputtering deposition and thin films characterization such as Hall, Optical and also XRD system measurements. I also would like to thank Seiichi Kishimoto Sensei from Kochi National College of Technology for his patience and help to characterize samples for Hydrogen gas testing measurements even when he was very busy.

Next, I would like to thank all of committee member and thesis defense examiners at KUT who have improved my research by their questions.

I am very glad a grateful that the KUT SSP Program exists, and I owe a debt of gratitude the wonderful IRD member for their help and academic assistance.

Thanks to all of my SSP friends in KUT and also thanks to all members of Thin Film Engineering Lab (Makino Laboratory).

Moreover, I am greatly indebted and owe many thanks to my parents and family who always support me even when I am exclusively focused on my research work and do not communicate with them regularly.